UNIVERSIDADE FEDERAL DO CEARÁ
CENTRO DE TECNOLOGIA
DEPARTAMENTO DE ENGENHARIA METALÚRGICA E DE MATERIAIS
PROGRAMA DE PÓS-GRADUAÇÃO EM ENGENHARIA E CIÊNCIAS DE MATERIAIS

MAURO ANDRES CERRA FLOREZ

SYNTHESIS AND CHARACTERIZATION OF OXIDES PRODUCED BY HIGH TEMPERATURE CORROSION ON GRADE 300 AND 350 MARAGING STEELS

FORTALEZA
2021

MAURO ANDRES CERRA FLOREZ

SYNTHESIS AND CHARACTERIZATION OF OXIDES PRODUCED BY HIGH TEMPERATURE CORROSION ON GRADE 300 AND 350 MARAGING STEELS

Thesis presented to the doctorate programs in Materials Science and Engineering of the Universidade Federal do Ceará and the Universitat Politècnica de Catalunya, as a requisite to obtain a double Doctor degree in Materials Science and Engineering.

Doctoral Advisors: Dr. Marcelo José Gomes da Silva and Dr. Gemma Fargas Ribas

FORTALEZA

2021

Dados Internacionais de Catalogação na Publicação
Universidade Federal do Ceará
Biblioteca Universitária
Gerada automaticamente pelo módulo Catalog, mediante os dados fornecidos pelo(a) autor(a)

C398s Cerra Florez, Mauro Andres.
SYNTHESIS AND CHARACTERIZATION OF OXIDES PRODUCED BY HIGH TEMPERATURE CORROSION ON GRADE 300 AND 350 MARAGING STEELS / Mauro Andres Cerra Florez. – 2021.
156 f. : il. color.

Tese (doutorado) – Universidade Federal do Ceará, Centro de Tecnologia, Programa de Pós-Graduação em Engenharia e Ciência de Materiais, Fortaleza, 2021.
Orientação: Prof. Dr. Marcelo José Gomes da Silva.
Coorientação: Prof. Dr. Gemma Fargas Ribas.

1. maraging steels. 2. heat treatments. 3. oxidation. 4. oxide film. 5. spinel ferrites. I. Título.
CDD 620.11

MAURO ANDRES CERRA FLOREZ

SYNTHESIS AND CHARACTERIZATION OF OXIDES PRODUCED BY HIGH TEMPERATURE CORROSION ON GRADE 300 AND 350 MARAGING STEELS

Thesis presented to the doctorate programs in Materials Science and Engineering of the Universidade Federal do Ceará and the Universitat Politècnica de Catalunya, as a requisite to obtain a double Doctor degree in Materials Science and Engineering.

Approved on: _____/_____/_____

PANEL MEMBERS

_____

Prof. Dr. Marcelo José Gomes da Silva (Advisor)
Universidade Federal do Ceará – UFC
(Ceará – Brazil)

_____

Prof. Dr. Enrique Rodriguez Castellón
Universidad de Málaga
(Mágala – Espanha)

_____

Prof. Dr. Clascidia Aparecida Furtado
Centro de Desenvolvimento da Tecnologia Nuclear
(Minas Gerais – Brazil)

_____

Prof. Dr. Carlos Augusto Silva de Oliveira
Universidade Federal de Santa Catarina – UFSC
(Santa Catarina – Brazil)

_____

Dr. Andreia de Souza Martins Cardoso
Universidade Federal Fluminense – UFF
(Rio de Janeiro – Brazil)

ACKNOWLEDGEMENT

I want to thank all the people involved during all the stages of preparing this work: my family, friends, the people from the Federal University of Ceará and the Universitat Politècnica de Catalunya who made this project possible.

To the supervising professors Dr. Marcelo José Gomes da Silva, Dr. Hamilton Ferreira Gomes de Abreu, Dr. Antonio Manuel Mateo Garcia and Dr. Gemma Fargas Ribas, for all their support, guidance, dedication, disposition and help in all stages of this investigation.

To professors Dr. Moises Bastos Neto, Dr. Enrique Vilarrasa Garcia, Dr. Joan Josep Roa Rovira, Dr. Enrique Rodriguez Castellon, Dr. Luis Flavio Gaspas Herculano, Dr. Jorge Luis Cardoso, Dr. Walney Silva Araújo and Dr. Emilio de Castro Miguel, for all the support and collaboration in the stages of the project that each one could contribute, without their collaboration it would not have been possible to obtain the results achieved.

To all my study and laboratory colleagues both at the Federal University of Ceará and at the Universitat Politècnica de Catalunya, Msc. Marcos Natan da Silva Lima, Msc. Ursula Cid, Msc. Francisco Oliveira, Dr. Erica Roteiro, Dr. Fernando Garcia Marro, Msc. Mohammad Rezayat and Msc. Daniela Tovar Vargas, for their support, helps in carrying out the experiments, companionship, and technical teaching.

To all the undergraduate students of the Lacam who at some moment supported me in the experimental procedures of this thesis

To all personnel of the laboratories / research groups: Laboratorio de Caraterização de materiais - LACAM, Laboratorio de Pesquisa em Corrosão - LPC, Laboratório de Pesquisa em Adsorção e Captura de CO_2 (LPA), Central Analitica of the UFC, Grupo de Nuevos Materiales Inorganicos of the Universidad de Malaga, the Centro de Integridad Estructural, Fiabilidad y Micromecánica de los Materiales (CIEFMA) of the UPC, and the Barcelona Research Center in Multiscale Science and Engineering of the UPC, in particular to Trifon Todorov Trifonov and Irene Lopez Peña.

To all academic support staff at different levels, both at the Federal University of Ceará and at the Universitat Politècnica de Catalunya, in particular the staff of the proreitoria de pesquisa e posgraduação and relaçoes internacionais of the UFC, and the coordinators of the postgraduate programs in Material Science and Engineering Dr. Cleiton Carvalho Silva from the UFC and Dr. Maria Lluïsa Maspoch Ruldua from the UPC.

To the FUNCAP and CAPES Brazilian agencies for the financial support received during my doctorate studies.

To Felipe, my husband, my mother Miladis and my mother-in-law Maria de Lourdes, for all the understanding, encouragement, support, and their daily contribution to my development as a human being.

ABSTRACT

The aging heat treatments in maraging steels are fundamental to achieving their excellent mechanical properties and, in some applications using oxidation surface treatments lead to induce a superficial layer formed by iron spinel which in some cases it can be protective. In this research, an exhaustive study of the characterization and mechanical properties of the grade 300 and 350 maraging steels was performed. Trying to produce a spinel-like oxide film on these steels during the aging heat treatment at 485 ºC, a novel procedure with particular conditions based in different steps combining time, temperature, atmosphere and leakage were developed. Four applications of the procedure were made using Air, O_2, CO_2 or N_2 in the first steps, and using similar conditions of steam, helium and N_2 atmospheres in the rest of the procedure. Afterwards, the layer produced in all the procedures was microstructural and mechanically characterized by means of advanced characterization techniques at the micro- and submicrometric length scale in order to highlight information related to the generated oxide layers. Differences between the oxides produced in all the conditions were found, such as roughness, thickness, and the quantity of the superficial heterogeneities (ridges, valleys, cracks, porosity and peeling), but the most important results area related to the chemical composition and the adherence of the oxides. The results of the procedure using air and O_2 atmospheres showed (in both steels) a non-homogeneous mix oxide formed by magnetite (Fe_3O_4), nickel ferrite ($NiFe_2O_4$), cobalt ferrite ($CoFe_2O_4$), MoO_3, TiO_2 and a particularly important quantify of hematite (α-Fe_2O_3). The oxide produced using CO_2 atmosphere was formed by TiO_2, MoO_3, hematite and the spinel $CoFe_2O_4$ being the latter one the majority compound. And using the N_2 atmosphere it was found that the oxide thickness (in both steels) was made up of the spinel's Fe_3O_4 and $CoFe_2O_4$ (with amounts was close to ~ 85%), MoO_3, TiO_2 and no Hematite was found.

Keywords: maraging steels; heat treatments; oxidation; oxide film; spinel ferrites; XRD study; Raman study; XPS study; nanoscratch study.

RESUMO

Os tratamentos térmicos de envelhecimento em aços maraging são fundamentais para o alcance de suas excelentes propriedades mecânicas e, em algumas aplicações usando tratamentos superficiais por oxidação, se induz à produção de uma camada superficial formada por espinélio de ferro que em alguns casos pode ser protetora. Nesta pesquisa, foi feito um estudo exaustivo da caracterização e propriedades mecânicas dos aços maraging 300 e 350. Tentando produzir um filme de óxido tipo espinélio sobre esses aços durante o tratamento térmico de envelhecimento a 485 ºC, foi desenvolvido um novo procedimento com condições especificas, baseado em diferentes etapas onde é combinado tempo, temperatura, atmosfera e vazão. Quatro aplicações do procedimento foram feitas usando Ar sintético, O_2, CO_2 ou N_2 nas primeiras etapas, e se utilizaram similares condições com vapor de água, hélio e N_2 no restante do procedimento. Posteriormente, a camada produzida em todos os procedimentos foi caracterizada microestrutural e mecanicamente por meio de técnicas avançadas de caracterização na escala de comprimento micro e sub-micrométrica a fim de destacar informações relacionadas aos óxidos produzidos e resultados notavelmente interessantes foram encontrados. Foram encontradas diferenças entre os óxidos produzidos nas quatro condições, tais como a rugosidade, espessura e quantidade de heterogeneidades superficiais (cristas, vales, fissuras, porosidade e descamação). Porém, os resultados mais importantes estão relacionados à composição química e à aderência dos óxidos. Os resultados do procedimento usando atmosferas de ar sintético e O_2 mostraram (em ambos os aços) uma mistura de óxido não homogênea formada pelos espinelios: magnetita (Fe_3O_4), ferrita de níquel ($NiFe_2O_4$), ferrita de cobalto ($CoFe_2O_4$), mas também por MoO_3, TiO_2 e uma quantidade particularmente importante de hematita (α-Fe_2O_3). O óxido produzido na atmosfera de CO_2 é composto por TiO_2, MoO_3, hematita e o espinélio $CoFe_2O_4$ sendo este o composto majoritário. E usando a atmosfera de N_2, verificou-se que a espessura do óxido (em ambos os aços) foi composta pelos espinelios Fe_3O_4 e $CoFe_2O_4$ (com quantidades próximas a ~ 85%), MoO_3, TiO_2 e nenhuma hematita foi encontrada.

Palavras-chave: aços maraging; tratamentos térmicos; oxidação; filme de óxido; ferritas de espinélio; estudo de DRX; estudo de Raman; estudo de XPS; estudo de nanoscratch.

RESUMEN

Los tratamientos térmicos de envejecimiento en aceros martensíticos son fundamentales para alcanzar sus excelentes propiedades mecánicas y, en algunas aplicaciones mediante tratamientos superficiales por oxidación, se induce la producción de una capa superficial de oxido formada por la espinela de hierro y que en algunos casos puede ser protectora. En esta investigación se realizó un estudio exhaustivo de la caracterización y de las propiedades mecánicas de los aceros maraging 300 y 350. Intentando producir una película de óxido tipo espinela en estos aceros durante el tratamiento térmico de envejecimiento a 485 ºC, se estableció un nuevo procedimiento con condiciones específicas, basado en diferentes etapas donde se combinan tiempo, temperatura, atmósfera y flujo. Se realizaron cuatro aplicaciones del procedimiento utilizando aire sintético, O_2, CO_2 o N_2 en las primeras etapas, y se utilizaron condiciones similares con vapor, helio y N_2 en el resto del procedimiento. Posteriormente, los óxidos producidos fueron caracterizados microestructural y mecánicamente mediante técnicas avanzadas de caracterización en la escala de longitud micro y submicrométrica con el fin de obtener informaciones relacionadas con los óxidos producidos, fueron encontrados resultados de grande interés. Se encontraron diferencias entre los óxidos producidos en las cuatro condiciones, tales como rugosidad, espesor y cantidad de heterogeneidades superficiales (crestas, valles, grietas, porosidad y descamación), sin embargo, los resultados más importantes están relacionados con la composición química y la adherencia de los óxidos. Los resultados de los procedimientos usando las atmosferas con aire sintético y O_2 mostraron (en ambos aceros) una mezcla de óxido no homogéneo formado por los espinelios: magnetita (Fe_3O_4), ferrita de níquel ($NiFe_2O_4$) y la ferrita de cobalto ($CoFe_2O_4$), pero también por MoO_3, TiO_2 y una cantidad particularmente importante de hematita (α-Fe_2O_3). El óxido producido en la atmósfera de CO_2 está compuesto de TiO_2, MoO_3, hematita y en mayor cantidad, la espinela $CoFe_2O_4$. Y utilizando la atmósfera de N_2, se encontró que el espesor del óxido (en ambos aceros) estaba compuesto por las espinelas Fe_3O_4 y $CoFe_2O_4$ (con cantidades cercanas a ~ 85%), MoO_3, TiO_2 y no se encontró hematita.

Palabras Clave: acero maraging; tratamientos térmicos; oxidación; filme de óxido; ferritas de espinela; Estudio de DRX; Estudio Raman; Estudio XPS; estudio de nanoscratch.

LIST OF ILLUSTRATIONS

LIST OF TABLES

LIST OF ABBREVIATIONS

AES	Auger Electron Spectroscopy
AFM	Atomic Force Microscopy
BCC	Body-Centered Cubic
BCT	Body-Centered Tetragonal
CAPES	Coordination of Superior Level Staff Improvement
CIEFMA	Center for Structural Integrity, Reliability and Micromechanics of Materials
EDS	Energy-Dispersive X-ray Spectroscopy
EIS	Electrochemistry Impedance Spectroscopy
ESCA	Electronic Spectroscopy for Chemical Analysis
FCC	Face-Centered Cubic
FE-SEM	Field Emission Scanning Electron Microscopy
FIB	Focused Ion Beam
FT-IR	Fourier Transform Infrared
FUNCAP	Ceará State Foundation to Support Scientific and Technological Development
HF	Fluoride Acid
LACAM	Materials Characterization Laboratory
LPA	CO_2 Adsorption and Capture Research Laboratory
LPC	Corrosion Research Laboratory
LSCM	Laser Scanning Confocal Microscope
OPC	Open Circuit Potential
SEM	Scanning Electron Microscope
TEM	Transmission Electron Microscopy
UFC	Federal University of Ceará
UPC	Universitat Politècnica of Catalunya
XPS	X-Ray Photoelectron Spectroscopy
XRD	X-Ray Diffraction

LIST OF SYMBOLS

300 E480	Samples of grade 300 maraging steel annealed at 840 °C by 1 h, and aged at 480 ºC by 3h
300 E560	Samples of grade 300 maraging steel annealed at 840 °C by 1h, and aged at 560 ºC by 1h
300 SOL	Samples of grade 300 maraging steel annealed at 840 °C by 1h
350 E480	Samples of grade 350 maraging steel annealed at 840 °C by 1 h, and aged at 480 ºC by 3h
350 E560	Samples of grade 350 maraging steel annealed at 840 °C by 1 h, and aged at 560 ºC by 1h
350 SOL	Samples of grade 350 maraging steel annealed at 840 °C by 1h
α′	Martensite
α-Fe_2O_3	Hematite
Al	Aluminum elemento
C	Carbon element
Co	Cobalt element
$CoFe_2O_4$	Cobalt ferrite spinel oxide
CoO-α-Fe_2O_3	Mixture of cobalt and iron oxides
CO_2	Carbon dioxide gas
E_{ocp}	OCP potential
F	Fluorine element
Fe	Iron element
Fe_2(Ti,Mo)	Solid solution Fe(Ti,Mo) or their mixtures
Fe_3O_4	Magnetite – Iron ferrite spinel oxide
γ	Austenite
I_{corr}	Corrosion current density
Mar300	Sample of grade 300 maraging steel
Mar300 5	Sample of grade 300 maraging steel after etching 5 minutes with
min Ar^+	Argonium cations
Mar350	Sample of grade 350 maraging steel
Mar350 5	Sample of grade 350 maraging steel after etching 5 minutes with
min Ar^+	Argonium cations

Mo	Molybdenum element
MoO_3	Molybdenum trioxide
N	Nitrogen element
Ni	Nickel element
Ni_3Mo	Solid solution Ni(Mo) or their mixtures
$Ni_3(Ti,Mo)$	Solid solution Ni(Ti,Mo) or their mixtures
$NiFe_2O_4$	Nickel ferrite spinel oxide
N_2	Nitrogen gas
O	Oxygen element
O_2	Oxygen gas
Ra	Roughness Average
Rp	Max Peak *ht*
Rv	Maximum Depth
Rz	Roughness Maximum
Sa	Arithmetic mean height roughness
Sp	Maximum pick height roughness
Sv	Maximum pit height roughness
Sq	Root-mean-square height roughness
Sz	Maximum height roughness
Ti	Titanium element
TiO_2	Titanium dioxide
UHS	Ultra-high-strength
V_{corr}	Corrosion potential
wt. %	Weight percent

LIST OF CHEMICAL REACTIONS

TABLE OF CONTENTS

PREFACE

Maraging steels are known for their ultra-high strength, with a Ni content of 18% or more, with low carbon and appreciable amounts of cobalt, titanium, and molybdenum. These steels have a martensitic microstructure and, with the help of thermal aging treatment at temperatures between 450-600 ˚C, it is possible to raise their yield limit to 2 GPa. This increase in their mechanical resistance is due to the nanometric precipitation of intermetallic compounds in its martensitic microstructure.

These steels have been the subject of several studies in which their mechanical and magnetic properties are evaluated, resulting in a wide range of applications. The purpose of this research is related to the applications in the manufacture of components of the ultra-centrifuges used to produce nuclear energy. As it is a controlled application, there are few articles published on this issue, and important details of the procedures for obtaining the oxide are omitted, with the few published works dating from the 1980s and 1990s. These works mention that using special atmospheres during the aging heat treatment, it is possible to obtain a thin layer of oxide with spinel-like microstructure (cubic cell containing combinations of tetrahedrons and octahedrons formed by oxygen, iron, nickel, and cobalt atoms), and that this layer protects steel from corrosive and mechanical attack attributed to exposure to fluorine-rich environments.

It is emphasized the importance that the results of this research allowed to establish a standard procedure for obtaining this type of films in maraging steel. Information was also obtained about the phenomena that happen during the formation and growth process of the oxide with spinel-type microstructure in maraging steels and their mechanical properties of adherence and hardness were evaluated. In addition to the previous one, it was possible to observe and verify the influence of different atmospheres on the chemical composition, surface finish and thickness of the oxide.

1 INTRODUCTION

This chapter briefly introduces the maraging steels, the oxidation process and spinel ferrites oxide, the objectives of this thesis and some initial remarks.

1.1 Literature Overview

Maraging steels are a group of steels known for their ultra-high resistance product of the combination of the effect between a martensitic matrix "Mar" with precipitation due to aging "aging" (MAGNÉE *et al*., 1974). These steels were created from research carried out by the International Nickel Company – INCO when seeking the production of steels for the manufacture of submarine hulls (FLOREEN, 1968), the initial chemical composition used had between 20 and 25% of Nickel, for not presenting the required mechanical properties, the addition of other alloying elements such as Aluminum and Titanium was required, which introduce the effect of precipitation due to aging (DECKER, 1979; MAGNÉE *et al.*, 1974). In these steels, the Nickel content varies between 17-19%, with exceptionally low Carbon content, Cobalt in the range of 7-12%, Molybdenum between 3-5%, amounts of Titanium between 0.2-1.6% and 0.1% of Aluminum approximately (MAGNÉE *et al.*, 1974; NICKEL DEVELOPMENT INSTITUTE, 1976).

Alloying elements provide maraging steel with improvements in its mechanical properties. Nickel guarantees the formation of a martensitic microstructure that, by itself, does not confer the high resistance of these materials; it may have a body-centered cubic microstructure (BCC) or, more typical, a body-centered tetragonal (BCT) (MAGNÉE *et al*., 1974). Cobalt increases the transformation temperature of martensite; in percentages between 6-9%, the limit of tensile strength increases and the solubility of molybdenum in martensite decreases, thus allowing the precipitation of intermetallic compounds during aging (NICKEL DEVELOPMENT INSTITUTE, 1976; PETTY, 1970; SCHMIDT; ROHRBACH, 1991). Molybdenum forms intermetallic compounds such as Ni_3Mo during the aging treatment, which hardens steel (MAGNÉE *et al*., 1974; PETTY, 1970). Titanium provides an increase in the resistance limit after the formation of Ni_3Ti during aging. It is important to mention that the ultra-low content of Carbon in the steel is mandatory since it can produce the precipitation of carbides that decreases the

resistance of the material (PETTY, 1970; RACK; KALISH, 1971). Aluminum, on the other hand, increases the resistance limit by hardening the martensite (DECKER, 1979; RACK; KALISH, 1971).

Currently, there are several types of maraging steels with Nickel content of approximately 18%, the differentiation parameter is the yield strength in units of thousands of ksi, as follows: classes or grades 200, 250, 300 and 350 (NICKEL DEVELOPMENT INSTITUTE, 1976). Table 1 presents the typical chemical compositions of maraging steel grades according to Petty (1970) and Nickel Development Institute (1976). The aging heat treatment is carried out at temperatures between approximately 450ºC and 600ºC and, during it, the precipitation of fine intermetallic compounds (Ni_3(Ti,Mo) and Fe_2(Ti,Mo), among others) occurs in the contours of the martensite and in lattice defects such as dislocations (MAGNÉE *et al*., 1974; VISWANATHAN; DEY; ASUDY, 1993). The formation of these precipitates exponentially increases the mechanical resistance of these steels, as can be seen in Table 2 adapted from Maximo (2014):

Table 1 – Chemical composition of the maraging steels classes

Chemical Composition (wt. %)							
Grade	**Fe**	**Ni**	**Co**	**Mo**	**Ti**	**Al**	**C_{max}**
200	Bal.	17,0 - 19,0	8,0 - 9,0	3,0 - 3,5	0,15 - 0,25	0,05 - 0,15	0,03
250	Bal.	17,0 - 19,0	7,0 - 8,5	4,6 - 5,2	0,3 - 0,5	0,05 - 0,15	0,03
300	Bal.	17,0 - 19,0	8,5 - 9,5	4,6 - 5,2	0,5 - 0,8	0,05 - 0,15	0,03
350	Bal.	17,5 - 18.5	12,0 - 12,5	3,8 - 4,6	1,4 - 1,7	0,10 - 0,15	0,03

Source: Petty (1970) and Nickel Development Institute (1976).

Table 2 – Mechanical properties of aged maraging steels

Maraging steels (18% Ni)				
Properties	**Grade 200**	**Grade 250**	**Grade 300**	**Grade 350**
Yield Strength (MPa)	1410	1720	1890	2380
Ultimate Tensile Strength (MPa)	1450	1750	1960	2450
Elongation (%)	13	13	11	9
Area reduction (%)	65	63	55	45

Source: Maximo (2014).

Due to their mechanical and magnetic properties and their weldability, maraging steels are used in different industries such as aeronautics, aerospace, military and nuclear, specifically in the latter, maraging steels have special stealth applications that make them impossible to obtain information due to their military use. Components of uranium isotopic enrichment ultracentrifuges for energy production are manufactured

with these steels and in Figure 1 adapted from Carlos (2011), the scheme of a typical centrifuge used for these purposes is observed.

For the production of nuclear energy, Uranium is used, which in nature is made up of three isotopes: U-238 (99%), U-235 (0.7%) and U-234 (bal.). After the ore is purified, it is converted into gaseous uranium hexafluoride (UF_6), which must be treated to increase the content of U-235 required for energy production. The most widely used enrichment process consists of centrifuges operating at high speeds, with high vacuum and other conditions. In it, the gas enters into the container and, due to the action of the centrifugal force activated by the rotor, the uranium U-238 (heavier) moves towards the extremes, while the U-235 (lighter) remains in the center and is sent to another centrifuge that continues the process until reaching a concentration of approximately 3% of U-235 (AGÊNCIA CÂMARA, 2005).

Figure 1 – Ultracentrifuge used during the Uranium enrichment process

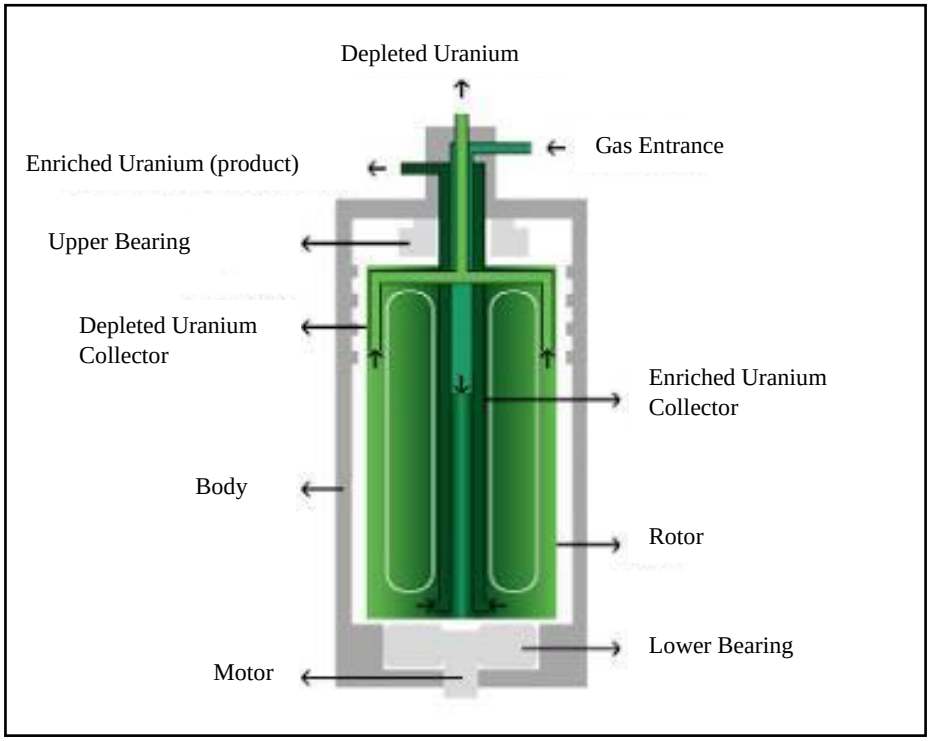

Source: Carlos (2011).

Because during the above process the entry of moisture is possible, there is a risk that it will react with UF_6 and produces small amounts of HF (hydrofluoric acid). For this reason, studies have been carried out on the production of oxides on the surface of maraging steels using different atmospheres during the aging treatment, with the main

objective of improving the corrosion resistance of these steels, it is important to mention that there are few publications available due to the confidentiality of this application of maraging steels.

Oxidation is also known as high temperature corrosion or dry corrosion. It occurs by chemical processes when a metal is exposed to an oxidizing gas at a high temperature (above dew point): the process occurs by the direct reaction between the material and gas, without the presence of liquid electrolyte. The term oxidation is not used for the presence of oxygen in the process, but for the use of an "oxidizing" gas that chemically corrodes the metal through the direct transfer of electrons that each atom of the metal gives up to the oxidizing gas atoms. It is possible to predict the oxidation of metal with the help of thermodynamics. There are Tables showing the enthalpy and free energy of most metal oxide formation reactions at different temperatures, as well as Ellingham diagrams that associate energy free standard with temperature. There are also curves for most metals in different atmospheres and temperatures. With the result of the analysis, it can be seen if the reaction is spontaneous, reversible or non-reversible, understanding that the more negative the value of free energy, the more spontaneous the reaction (GENTIL, 2012; JONES, 1996).

In the oxide formation process, there are several steps. Some authors mention a first contact between the gas and the metal surface, followed by the adsorption of the gas, continuing with chemical reactions that form small nuclei of the oxide and, in sequence, lateral growth to create a continuous film that covers the base metal. Formed a uniform film, the next step is diffusion through it for growth to occur; This will depend on the chemical and physical properties of the oxide. The diffusion process occurs through the concentration gradient due to the variation of the composition at the oxide interfaces, as well as by the electric potential gradient related to the charge differential at the same interfaces. The movement of reactants through the oxide (ionic conduction) occurs when the anions (ions of the elements of the oxidizing gas) go from the outer layer to the base metal (anionic diffusion), and the metal cation diffuses into the outer gas (diffusion cationic). Electrons also move through the oxide layer from the metal to the outer layer in order to form anions (electronic conduction). The species transport process is favored by imperfections in the oxide crystal lattice, such as vacancies (GENTIL, 2012; JONES, 1996; STEHLE *et al*., 2011).

An oxide film may or may not be protective, and this will depend on its various characteristics of it. One is adhesion to avoid flaking and rust detachment, generally the thinner, the more adherent. It is also found that the greater the similarity between the crystal structure of the oxide and that of the metal, the greater the adhesion. The oxides must have good plasticity to avoid fractures. The film must have a coefficient of thermal expansion similar to that of metal. It must have low electrical conductivity to decrease the diffusion of electrons. The ion diffusion coefficient must be low, and this is related to the low number of vacancies in the crystal lattice. A combination of high melting point and low vapor pressure is also required to prevent spoilage and evaporation, respectively (GENTIL, 2012; JONES, 1996).

Any metal material currently used by the industry can corrode when exposed to an oxidizing atmosphere such as oxygen, sulfur, halogens, sulfur dioxide: SO_2, H_2S, water vapor, CO_2, among others. Oxidizing gases act as the cathode in the oxide layer growth process and have an important influence on the properties and characteristics of the film formed. An example of this is the atmospheres containing carbon (CO_2 or CO) that, in contact with ferrous alloys at high temperature, produce two phenomena: carbonation and decarbonization. The first is the diffusion of the reduced carbon within the metallic matrix and it reacts to form carbides with the elements of the steel, generating dissolution processes such as carburizing, which is the surface hardening of the alloy due to the formation of Fe_3C. The decarbonization phenomenon occurs mainly in low-alloy steels in the presence of gases that have an affinity for carbon at high temperature, where the carbon in the metal matrix is removed by its reaction with oxidizing gases (GENTIL, 2012; JONES, 1996).

It is known that water vapor is more aggressive than dry air or oxygen. In steels exposed to such atmosphere at high temperatures, water reacts with Iron forming oxides such as the iron spinel magnetite (Fe_3O_4) or hematite (Fe_2O_3), as well as other by-products of the reaction with water and hydrogen (as shown in reaction 1). It can diffuse into the oxide and reach the metal, causing the damage mentioned above. The by-product water continues the reaction, producing more oxide and more Hydrogen continuing reaction 2 (GENTIL, 2012; JONES, 1996; KLEIN; SHARON; YANIV, 1981; STEHLE *et al*., 2011).

$$3Fe + 8H_2O \rightarrow Fe_3O_4 + 4H_2O + 4H_2 \quad (1)$$

$$3Fe + 4H_2O \rightarrow Fe_3O_4 + 4H_2O \quad (2)$$

The Spinel is a microstructure of complex oxides with typical characteristics of ceramic materials. The structure has a body-centered cubic or tetragonal body-centered cubic symmetry, grouping eight AB_2X_4 units, where A represents a metal cation with valence 3 (A^{3+}), B is a metal cation with valence 2 (B^{2+}) and X is the atom of oxygen (O^{2-}) (DA SILVA, 2016). The best known spinels are those constituted of elements such as Magnesium and Aluminum ($MgAl_2O_4$) (VITOR *et al*., 2006).

There are other types of spinel known as ferrites, which are ferromagnetic ceramics generally considered the combination of hematite (Fe_2O_3) with other metal oxides. They are widely used due to their chemical stability, optical, magnetic and electrical properties, as well as their resistance to corrosion. One of them is Nickel ferrite spinel ($NiFe_2O_4$) which has an inverse structure as the crystallographic formula $[Fe^{3+}]$ $[Ni^{2+}\ Fe^{3+}]\ O_4^{2-}$, widely used in industry due to its high hardness, chemical stability and especially its excellent magnetic properties (RODRIGUES *et al*., 2015).

There is also cobalt ferrite spinel ($CoFe_2O_4$) that has a partially inverse structure with the crystallographic formula $[Fe^{3+}]$ $[Co^{2+}\ Fe^{3+}]\ O_4^{2-}$, and has high hardness, chemical stability and is magnetically hard (resistance to magnetization and demagnetization) (RODRIGUES *et al*., 2015). The best-known iron spinel is magnetite (Fe_3O_4), it has a real composition of $FeO.Fe_2O_3$, and its structure is inverted with the formula $[Fe^{3+}]$ $[Fe^{2+}\ Fe^{3+}]\ O_4^{2-}$. Figure 2 shows how the oxygen ions (red spheres) form a face-centered cubic packing structure (FCC), the Fe^{3+} cations (blue spheres) occupy the tetrahedral sites and a 50:50 mixture of Fe^{2+} and Fe^{3+} (gray spheres) is located at octahedral sites. Magnetite has special properties and is used in biotechnological, magnetic, electrical and catalysis applications, among others (DINIZ *et al*., 2015; PARKINSON, 2016).

Figure 2 – Representation of the iron spinel ferrite (Fe_3O_4)

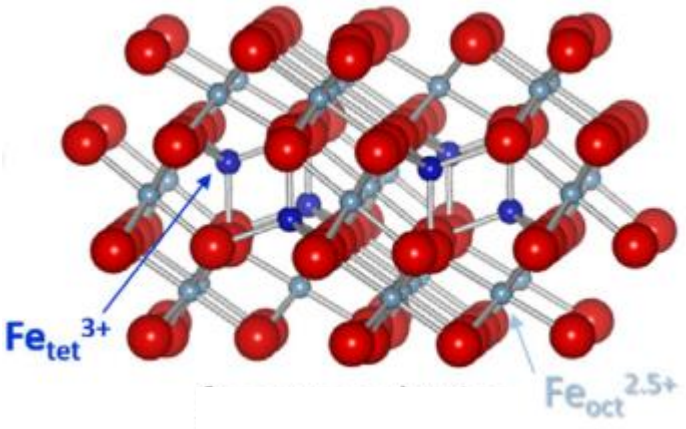

Source: Parkinson (2016).

1.2 State of the art

Klein, Yaniv and Sharon (1981) characterized and studied the process of formation and growth of oxides in Fe-18Ni-8.5Co and Fe-29Ni-17Co steels. They used air and superheated steam during the aging heat treatment performed at 485 °C for 3 hours in the two steels and in both atmospheres, a 2-3 μm thick oxide film was obtained. Two layers were found, which with the help of the analysis performed by X-ray energy dispersive spectroscopy (EDS) and Auger electron spectroscopy (AES), it was discovered that the inner layer had a higher concentration of nickel and cobalt and less content of oxygen and iron, and in the outer layer the opposite situation was found. X-ray diffraction (XRD) measurements confirmed that the outer layer was composed mainly of Fe_3O_4 and concluded that the growth of the layer is mainly due to the cationic migration of iron through the oxide.

Klein, Yaniv and Sharon (1983) studied in 1982 the composition profile, as well as the role of Titanium and Molybdenum in the formation of the oxide film during the aging treatment of grade 250 maraging steel. This was done at 485 °C for 3 hours in an atmosphere of superheated steam. They used samples of pure Titanium (99.99% purity), pure Molybdenum (99.99% purity) and maraging steel grade 250 containing approximately 5% Molybdenum and 0.4% Titanium. In the results obtained by electronic spectroscopy for chemical analysis (ESCA) and by AES, it was observed that in pure metals a uniform oxide layer of these metals was formed, while in maraging steel a film with several layers was discovered, with the outermost one composed of pure Fe_3O_4 (without any other alloying element); the following layers had amounts of Molybdenum

and Titanium, without Cobalt or Nickel, increasing the amount of molybdenum as it approaches the oxide-metal interface, mainly forming the oxides $MoO_3.xH_2O$, MoO_3, Mo_2O_5 or MoO_2, and pure Mo in the last layers; while Titanium appears more at the bottom with a thin layer of TiO_2. The authors concluded that due to the location of TiO_2 within the oxide, the oxidation process does not occur due to the migration of oxygen anions, but rather due to the movement of iron cations towards the oxide-gas interface.

In the work carried out by Greyling, Kotzi and Viljoen (1990), the kinetics of the growth of an oxide film on a grade 300 maraging steel produced by heat treatments in an atmosphere with air was studied, varying the time from 5 to 180 minutes and the temperature from 300 to 600 °C. With the help of characterization techniques, they determined the thickness and chemical composition of the oxide layer formed. They found that at temperatures below 480 °C the oxide growth curves have a rapid increase at the beginning, which then becomes little or zero as time passes, as a consequence of this, there are thinner layers. In the curves found at temperatures above 500 °C, rapid growth was observed that increases with time and exposure temperature; as a result, there are larger layers.

In the previous study, it is mentioned that the kinetics of oxidation occurs through the transport of reactive gas and metallic species through the oxide layer and that this movement depends on the conductive properties of the oxide; thus, the presence of defects in the network will be an obstacle to the circulation of species. The authors discovered with the help of the application of a thin layer of gold on the surface of some samples before the oxidation process, and that by the location of the layer of this metal near the Metal-Oxide interface, it is suggested that the Rust growth is due to external migration of metal ions through the film. They also discovered that the oxides formed at all temperatures had three different crystallographic structures within the layer, the outermost one formed by the CoO-α-Fe_2O_3 phase and with approximately 10% of the total thickness; the second, with 80% of the layer, formed by α-Fe_2O_3; and the third structure, with the remaining 10% of the layer, formed by oxide with an unidentified spinel microstructure.

Rezek, Klein and Yahalom (1997) did a heat treatment in a grade 250 maraging steel for 3 hours in a superheated steam atmosphere, varying the steam flow to obtain a protective oxide. They found that the layer produced with the lowest flow was thinner than the layer formed with the highest flow. When characterizing the oxides, they

found that when high flux was used, two layers were formed: the inner layer (40% of the total thickness) composed of hematite (α-Fe_2O_3) and the outer layer (60% of the total thickness) of magnetite (Fe_3O_4). When a lower flux was used, three layers were formed within the oxide: the innermost layer composed of hematite and with 7% of the total thickness; the next composed of magnetite, with the majority of the total thickness; and finally, a porous, thin layer of hematite. It is important to mention, within the previous phase's small quantities of other alloying elements, such Nickel and Cobalt, were found; these elements were distributed inside the oxide film with a higher content near to the metal matrix, and with a decrease in the more external oxide layer.

More recent works on oxidation of maraging steels through heat treatments were not found, however, works on similar processes in other types of steels have been widely disseminated, among them, those of Luo and Shenz (2008), who studied the KOVAR steel oxidation process (28% Ni, 17% Co, etc.) in 3 conditions of the atmosphere, temperature and various times, thus, N_2-2.31% H_2O-0.95% H_2 at 500 °C, N_2-2.31% H_2O-0.5% H_2 at 1000 °C and N_2-2.31% H_2O at 1000 °C. The results helped to describe kinetic processes and to find that in the first of the treatment, magnetite (Fe_3O_4) was formed entirely, in the second, FeO and in the third, a mixture of these two oxides. Among their conclusions, it is necessary that in the process of diffusion of the oxygen ion from the gas-oxide interface towards the interior, it was in charge of forming the initial films and that the diffusion of Iron ions from the metal-oxide interface to the outside determined the growth of mixed oxide.

Dudziak *et al*. (2017) studied the behavior of advanced steels type 309S, 310S and HR3C, together with Nickel alloys type Haynes 230, alloy 263, alloy 617 and Haynes 282, when they were subjected to conditions of the steam atmosphere of water in an furnace at 800 ºC and for 2000 hours. They found that the materials had a small mass gain. In the chemical analyzes on the surface of the Nickel alloys, they found oxides Cr_2O_3 (alloy 617, Haynes 282, alloy 263 and Haynes 230), $MnCr_2O_4$ (alloy 617, Haynes 282 and Haynes 230), $NiCr_2O_4$ (alloy 617) and TiO_2 (alloy 263, Haynes 282). Cr_2O_3, $MnCr_2O_4$, Mn_7SiO_{12}, FeMn (SiO_4) and SiO_2 were already found in the steels. The kinetics of the reactions was studied, and different techniques were used to characterize the oxides formed.

2 OBJECTIVES

In recent years, the materials characterization laboratory (LACAM) of the Federal University of Ceará – Brazil, has been studying maraging steels, through partnerships with renowned researchers from different universities with whom we have been able to publish several articles on the influence of heat treatments on their mechanical and magnetic properties. Maraging steels are widely used in high-performance applications due to their suitable properties, mainly good toughness, and high resistance to crack propagation and thermal fatigue. Although there are extensive number of works about their excellent combination properties, there is a lack of their behavior in fluoride solutions, and scarce information about their production of spinel oxide films and their oxidation behavior. In this regard, the main objective which this work is focused are:

To study the corrosion behavior of maraging steels in solutions with hydrofluoric acid and understand the influence of chemical composition and thermal treatments (solution annealed and aged) on their corrosion resistance.

Establish a procedure to obtain an oxide layer with the highest amount of spinel-like microstructure on grade 300 and 350 maraging steels, using four different mixtures of gases (N_2, O_2, CO_2 and synthetic air) with steam during the aging heat treatment of these steels.

Identify the characteristics of the oxides formed, such as the chemical composition, crystallographic structure, phases present, thickness, roughness, morphology, as well as their adherence, in order to study their properties and determine what had the best characteristics.

Based on the results achieved, determine the oxidation mechanisms responsible for the formation and growth of oxides for the different conditions studied.

3 METHODOLOGY

3.1 Materials

Two different kinds of maraging steels 300 and 350 (chemical composition for each is summarized in Table 3) were supplied by the Materials Characterization Laboratory of the Universidade Federal do Ceará and used in this research. The samples were cut in 20 mm × 10 mm × 5 mm. Considering the chemical composition, a thermodynamic simulation was performed using the Thermo-Calc® software (TCFE6 database), which allowed to obtain mass fraction diagrams of the phases found in the steel through thermodynamic equilibrium calculations to obtain phase diagrams. The solution annealing temperature (840 ºC) and the aging temperatures (480 ºC and 560 ºC) were selected according to the thermodynamic simulations and the information found in the literature (NICKEL DEVELOPMENT INSTITUTE, 1976; RACK; KALISH, 1971; SCHMIDT; ROHRBACK, 1991; VISWANATHAN; DEY; ASUDI, 1993). The time chosen for the solution annealing was 1 hour and aging heat treatments were 3 h at 480 ºC and 1 h at 560 ºC. The heat treatments were carried out in a muffle furnace and air-cooled.

Table 3 – Chemical composition of maraging steel grades (wt.%)

	Fe	Ni	Co	Mo	Ti	Cr	V	Si	Al	C
Grade 300	Bal.	18.28	9.51	4.80	0.73	0.12	0.10	0.08	0.07	< 0.01
Grade 350	Bal.	17.65	11.65	4.69	1.44	0.05	0.10	0.04	0.06	0.002

Source: Author (2021).

In order to identify the steel phases, X-Ray Diffraction Analysis was carried out using a Panalytical X'Pert Pro diffractometer with CoKα radiation (0.1789 nm). The 2θ angle ranged from 40º to 110º, with an angular step of 0.02º per scan and 3 s of counting time. The voltage and current used were 40 kV and 45 mA, respectively. The identification of the phases was carried out with the X´PertHighScore Plus® software from Panalytical®. The phase quantification through X-ray diffraction (XRD) was carried out using the direct comparison method as described by Pardal *et al*. (2006) and Santos *et al*. (2015), assuming that the chemical composition of the austenite and martensite phases may be different. Three peaks of martensite {111}, {200}, {211}, and three peaks of austenite {111}, {200}, {220}, were analyzed, and in order to minimize the effect of

the texture, the average values of all diffraction peaks were calculated and compared (SANTOS *et al*., 2015).

Microstructural analysis with EBSD was performed, processed, and plotted on the Oxford/HKL Channel 5 software to confirm the phases on the steels in each condition.

Following the heat treatment, the samples were ground using SiC paper up to 2000 mesh with continuous water flow, then polished with 1 μ and 0.05 μ alumina (Al_2O_3), rinsed with distilled water and alcohol, and blow-dried. Two etching steps were used to reveal the microstructure: electrolytic etching with chromic acid H_2CrO_4 (20%) solution for 15 s at 10 V and then etching with Nital 2% for 10 s to reveal the prior austenite grain boundaries. A Zeiss® model AX10 optical microscope was used to observe the microstructure and the ImageJ software was used to calculate the prior austenite grain size through the method described by Silva *et al.* (2019)**,** based on the American Society for Testing and Materials – ASTM E112-96 (ASTM, 2015a). To reveal the martensite microstructure, an electrolytic etching (10 V) was used in a chromic acid H_2CrO_4 (20%) solution for 15 s, and then etched with Marble solution (4g $CuSO_4$ + 20ml HCl + 20ml H_2O) for 10 s. After that, the samples were observed in the Scanning Electron Microscope (SEM) model quanta 450.

Rockwell C hardness tests (HRc) were performed according to ASTM E18 (2003) standard (ASTM, 2105b) using a Microtest model 737 durometer with a conical diamond penetrator. The preload and main load applied were 10 and 150 kgF, respectively. The highest and lowest values were eliminated, and the average was taken from the remaining values.

3.2 Electrochemical measurements in steels

Electrochemical measurements were carried out on a Metrohm® Autolab PGSTAT 302N potentiostat/galvanostat controlled by the NOVA® software for data acquisition. Open Circuit Potential (OCP), Linear Polarization, and Electrochemical Impedance Spectroscopy tests were performed. A conventional three-electrode cell was used. An Ag/AgCl (saturated KCl) electrode was used as a reference, a platinum plate with a geometric area of approximately 130 mm^2 was used as a counter electrode, and the working electrodes were the samples of both maraging steels. Samples were ground up

to 2000 mesh, rinsed with distilled water and ethanol to degrease them and then blow-dried. Before the tests, an exposed area of approximately 30 mm^2 was fixed on the samples. The measurements were taken in a Faraday cage at room temperature. The OCP tests were performed by submerging the samples in 0.01M HF (hydrofluoric acid) solution for 30 min. The linear polarization curves were obtained in a potential range from -200 to +600 mV around the OCP with a scan rate of 1 mV/s in accordance with the literature (KUMAR; SHETTY, 2013; POORMINA; NAYAK; SHETTY, 2010; SANATKUMAR; NAYAK; SHETTY, 2012). The tests ended when the current density reached 1 mA. The Electrochemical Impedance Spectroscopy tests were performed after potential stabilization for 30 min. The sinusoidal disturbance of the corrosion potential was 10 mV, the frequency range used was from 50 kHz to 0.01 Hz, and the reading rate was 10 points per decade of frequency.

After the polarization tests, the surface of the samples was observed in the SEM Phenom XL with EDS detector. Raman spectroscopy analysis was also performed in a Renishaw inVia ™ confocal Raman microscope with a Neon Laser ($\lambda \sim 532$ nm), while the analysis of Raman intensities was performed using the WIRE software.

3.3 Samples preparation for oxidation process

Samples of the grade 300 and 350 maraging steels were solution annealed at 840 ºC for 1 h, and then, ground/polished using SiC paper up to 2000 mesh with continuous water flow and washed with alcohol and blow dried using a dryer. In order to obtain a surface roughness, the specimens were ground and polished, and its roughness was observed using the Atomic Force Microscope (AFM, Dimension D3100) and the resulting images and the superficial roughness analyses were conducted using the WSxM 5.0 software (HORCAS; FERNÁNDEZ, 2007). In order to perfectly assess the surface topography, several parameters were evaluated: including average roughness (Ra), maximum vertical height between the highest peak and the lowest valley (Rz), maximum peak height (Rp) and maximum valley depth (Rv). More information about the mathematical and physical definitions of the roughness parameters, as well as their respective equations, summarized in Gadelmawla *et* al. (2002), Nwaogu, Tiedje and Hansen (2013) and Zhang *et al*. (2020).

3.4 Preliminary oxidation process

The aging heat treatment was carried out in a tube furnace connected to a water vapor generator and N_2 gas injection. The samples were placed in the furnace inside a quartz tube and heated up to 500 °C with N_2 gas flow for 60 min. When the temperature of 500 °C was reached, a combined flow of water vapor and Nitrogen was used for 3 h. The cooling process was taken inside the furnace with N_2 gas flow to prevent the furnace oxygen entrance that could over oxidize the samples.

3.5 Main oxidation process

The main procedure of the oxidation during the aging heat treatment to produce an oxide layer on maraging steels was performed in a tube furnace with a gas inlet connected to 5 lines, one connected to a steam generator and the other four connected to O_2, Air synthetic, CO_2 and N_2 cylinders. The steam generator was used at 150 ºC and it was connected to helium injection as a carrier gas to increase the flow rate. The flow of all gases was measured with a flow meter, and the configuration of the experiment can be seen in the assembly representation in Figure 3.

The samples of each steel (in different experiments) were heated at 300 ºC for 30 minutes under O_2 or Air synthetic or CO_2 or N_2 atmosphere with a flow of 400mL/min. Steam was added and the temperature was increased to 490 ºC for 15 minutes. Shortly thereafter, the O_2 or Air synthetic or CO_2 or N_2 gas was removed, and the temperature was kept at 490 ºC for 3 hours only with steam and helium flow of 600 mL/min (maximum operativity of the flowmeter). The cooling step at room temperature was performed for 3 h with a N_2 flow (400 mL/min) to avoid over oxidation of the samples.

Figure 3 – Experimental configuration of the devices used for the oxidation treatments

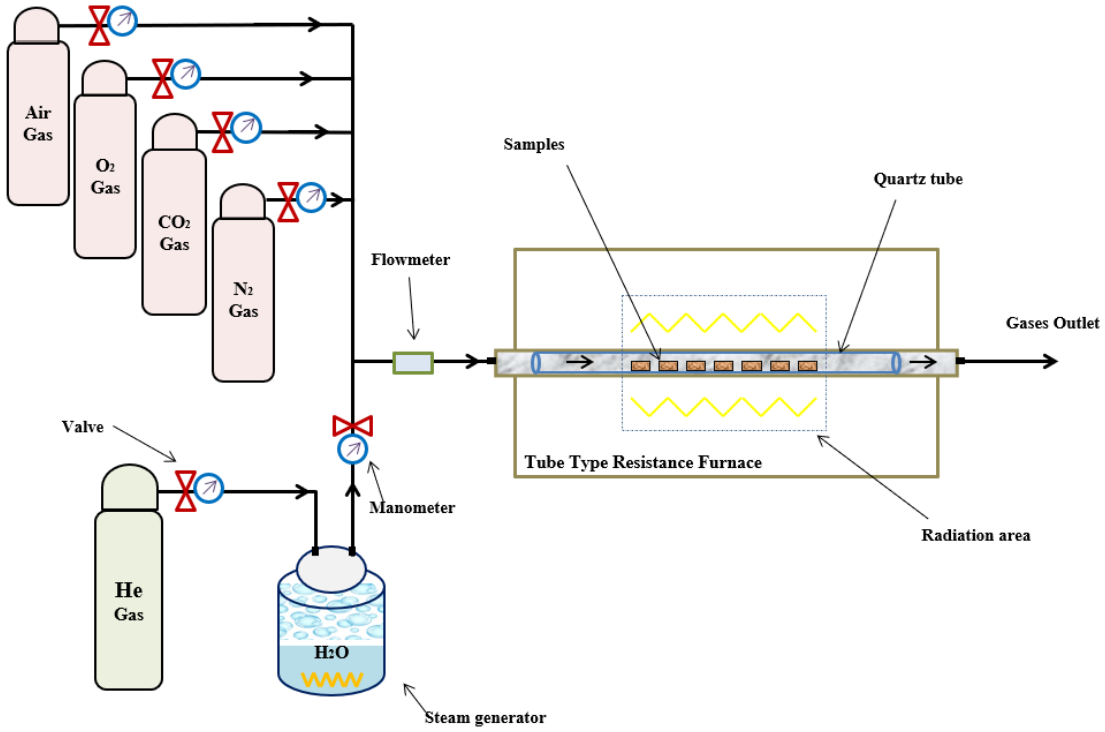

Source: Author (2021).

3.6 Oxide characterization

After the oxidation treatments, the sample's surface of all steels was characterized by different advanced techniques in order to understand the oxidation process and to know the different phases formed. The Carl ZEISS LSM 800 confocal laser microscope (CLSM), the White Light Interferometry (WLI, Veeco Wyko 9300NT) and the Atomic Force Microscope (AFM, Dimension D3100) were used to observe the surface morphology and to obtain the oxide roughness. Furthermore, the roughness parameters obtained in the interferometer were measured to quantitatively assess the oxide layer topography by using the Filmetrics® software, which includes: the arithmetic mean height (Sa), the maximum height (Sz), the maximum peak height (Sp), the maximum pit height (Sv) and the root mean square height (Sq). More information related to the roughness parameters is available in Dong, Sullivan and Stout (1994a; 1994b) and Flamant *et al*. (2016). The roughness observed by the AFM and the resulting images and the superficial roughness analyses were conducted by using the WSxM 5.0 software with the procedure mentioned before.

For the identification of the components presents on the oxide layer, low angle X-ray diffraction (XRD), Fourier Transformation Infrared (FT-IR) spectroscopy, RAMAN spectroscopy and X-ray photoelectron spectroscopy (XPS) measurements were used. The XRD using the Philips X'Pert equipment (Co Kα radiation source) with a wavelength (λ) of 1.789 nm and monochromator. The XRD spectra were conducted from $15^{o} \leq 2\theta \leq 80^{o}$, the low angle configuration using the following parameters: 3^{o} angle with an angular step of 0.02^{o} per scan and counting time of 3 s, with voltage and current of 40 kV and 45 mA, respectively. The results were performed and analyzed using the X´PertHighScore Plus® software by Panalytical®, and the semi-quantification (%) of the phases was done using the software mentioned applying the reference intensity ratio (RIR) based on the Chung (1974) methodology and mentioned by Zhou *et al*. (2018). The Furier Transformation Infrared (FT-IR) spectroscopy was used on the Fourier Nicolet 6700 infrared spectrometer (Thermo Scientific), using the KBr pellet method at room temperature. The RAMAN was performed on the Renishaw's inVia Qontor Raman microscope with a neon laser with λ ~ 532 nm, with intensity analysis performed in Raman Environment (Wire ™) software.

Finally, the third one X-ray photoelectron spectroscopy (XPS) measurements were performed on the Physical Electronics spectrometer (PHI Versa Probe II Scanning XPS Microprobe) with monochromatic X-ray radiation Al Kα (1400 μm, 26.6 W, 5 kV, 1486.6 eV) and a double beam neutralizer. The experiments were carried out after cleaning the surface for two pickling cycles with argon (Ar) ions at 0.5 eV for 1 min and 1 keV for 5 min, respectively. XPS spectra were processed using the MultiPak 9.0 package. The binding energy values were referenced to the C 1s adventitious signal at 284.8 eV and the recorded spectra were fitted using Gauss-Lorentz curves. The atomic concentration percentages of the constituent elements on the surfaces of the samples were determined taking into account the sensitivity factor of the corresponding area for the different measured spectral regions.

Phenom XL Desktop SEM microscope and SEM (Quanta 450 FEG - FEI), both with EDS detectors, were used to observe the oxide and obtain the chemical composition measurements. Furthermore, the oxide layer thickness, the wall chemical composition maps, as well as their microstructure were determined by focused ion beam (FIB) milling of cross-sections and SEM inspection, it was done by using a dual beam workstation, Zeiss Neon 40. A thin platinum layer was deposited on the sample prior to

milling process with the aim of reducing ion-beam damage. A Ga+ ion source was used to mill the surface at a voltage of 30 kV. The final polishing process of the cross-section was performed at a current of 500 pA and 30 kV acceleration voltage.

3.7 Sliding properties of the oxides

Nano-scratch tests were made with a nano-scratch attachment of the Nanoindenter XP that allows lateral force measurements. A Berkovich indenter was used to scratch the surface under increasing load at a velocity of 10 μm/s for a total scratch length of 500 μm up to a maximum load of 100 mN. Three different scratches were performed on each sample. The distance between scratch was held constant and equals to 500 μm to avoid any overlapping effect. The tests were made according to the ASTM C1624 “Standard Test Method for Adhesion Strength and Mechanical Failure Modes of Ceramic Coatings by Quantitative Single Point Scratch Testing” (ASTM, 2015c), and the work developed by Ghasemi Parizi *et al*.

Damage induced during the nanoscratch process was investigated by SEM inspection, using the Phenom XL Desktop SEM and the Zeiss Neon 40 SEM microscopes.

4 RESULTS

To fulfill the above-mentioned objectives, the results of this thesis were organized in sub-chapters based on a transcription of papers (published and/or in process to be published) covering all the qualitative and quantitative analysis of the results obtained through the techniques cited in the methodology. Each of these sub-chapters contains a review, results with discussion, and finally its conclusions.

In the sub-chapter 4.1, an experimental study about the characterization and corrosion evaluation of grade 300 and 350 maraging steels is shown. In the 4.2 sub-chapter, a preliminary procedure was studied to produce a spinel-like oxide layer on grade 300 maraging steel.

At this point, a new procedure for the oxidation process using different atmospheres during the steps was established and applied on grade 300 and 350 maraging steels.

In the 4.3 sub-chapter the new procedure was applied, the process was used with two oxygen rich atmospheres (i.e.: air, O_2), and with steam and nitrogen. The 4.4 sub-chapter shows the results of the oxidation procedure using a CO_2 atmosphere, and steam/N_2 in different steps. Finally, in sub-chapter 4.5 the nitrogen/steam atmospheres were used during the oxidation procedure, and a spinel-like oxide was produced.

4.1 Microstructural characterization of grade 300 and grade 350 maraging steels and electrochemical study in hydrofluoric solution

4.1.1 Review

The electrochemical behavior of solution-annealed grade 300 and grade 350 maraging steels subjected to two different aging temperatures in an aqueous hydrofluoric acid (HF) medium was evaluated. The microstructural and hardness studies showed the effects of the chemical composition and heat treatments on the material properties. Although it is not possible to observe them, the fine intermetallic composites deposited during aging allow a significant increase in the hardness of materials, which was reduced when aged at 560 ºC, where there was the formation of reverted austenite. The results showed that, in both steels, solution-annealed samples that were not aged showed a better

corrosion behavior than the aged samples. The reversion of austenite during aging at temperatures above 560 ºC increases the phase limits quantity and its susceptibility to corrosion. The greater amount of cobalt and titanium in grade 350 maraging steel increases the amount of fine intermetallic precipitate rich in molybdenum and titanium during aging, therefore improving its mechanical properties, but also reducing its corrosion resistance.

Maraging steels are used in the manufacture of centrifuge rotors to enrich uranium for the production of nuclear fuel. In these applications, maraging components are exposed to atmospheres rich in fluorine and fluoride acid residues that are highly corrosive (BARZASHKA; OELRICH, [*s.d.*]; BRADHURST; HEUER, 1981; GLASER, 2008). Bradhurst and Heuer (1981) investigated the susceptibility of grade 350 maraging steel to crack propagation by performing tensile tests in closed chambers containing an atmosphere rich in uranium hexafluoride (UF_6) and/or hydrofluoric acid (HF) at 70 ºC. The results showed that when the UF_6 was dry, the steel showed good resistance to cracking. However, in conditions in which hydrofluoric acid cracks appeared, the failure stress decreased. They concluded that this hydrogen embrittlement failure mechanism is linked to the hydrogen produced in reactions with the metal. It is also mentioned in the literature that fluorine may react, forming metallic fluorides that would be protective, and even the use of anodizers to improve the corrosion resistance was suggested (BARZASHKA; OELRICH, [*s.d.*]), but no test showed any result that confirms this information.

Poormina, Nayak and Shetty (2010) studied in two works grade 250 maraging steels solution annealed at 815 ºC for 1 h and aged (without information on aging conditions) using polarization tests and electrochemical impedance spectroscopy in various concentrations of phosphoric acid solution. They concluded that the increase in the acid concentration decreases the corrosion resistance of this steel, showing a higher corrosion rate. They also mentioned that the solution-annealed steel showed better corrosion behavior than the aged one because of the presence of intermetallic precipitates (with different matrix composition), causing deformation fields to form around these precipitates (due to the incompatibility of the network between the precipitate and the matrix) and deterioration of the steel, leading to the corrosion of aged samples when compared with the solution-annealed ones.

Sanatkumar, Nayak and Shetty (2012) and Kumar and Shetty (2013) studied welded grade 250 maraging steel in different concentrations of hydrochloric acid (HCl) solutions. They used the polarization and electrochemical impedance techniques and found that as the acid concentration increases, the aged steel has less corrosion resistance and the corrosion rate increases, but the corrosion potential shifts to less negative values. They observed the surface of the samples using SEM after the corrosion tests and found that the surface was deteriorated, with signs of intergranular corrosion.

This work aims to characterize both maraging steel grades, 300 and 350, and to study the electrochemical behavior in hydrofluoric acid solution. It also aims to understand the influence of chemical composition and heat treatments such as solution annealing and aging on their corrosion resistance. All this sub-chapter was published in January/27/2021 in the Journal of Fluorine Chemistry (CERRA FLOREZ *et al*., 2021).

4.1.2 Results and Discussion

The chemical composition of the steels allowed the performance of a thermodynamic simulation in the Thermo-Calc® software, where mass fraction diagrams were generated to show the quantities of the phases found in the steels according to the temperature. The mass fraction diagram for grade 300 and 350 maraging steels are shown in Figure 4a and 4b, respectively. This result made it possible to identify areas of stability for the predicted phases. At temperatures between 670 ˚C and 1380 ˚C, austenite (FCC) is the only phase present in this steel. At higher temperatures, the liquid is produced, and at lower temperatures, martensite (BCC) is formed and the Mu and Ni_3Ti phases are segregated. As the temperature decreases, the amount of martensite increases proportionally to the austenite decrease. The segregated phases reach a maximum amount that remains fixed until reaching room temperature, with the particularity that the Mu phase is slightly larger than the titanium nitride phase.

In Figure 4b the same phases found in the grade 300 maraging steel diagram were identified, and it is possible to find minor differences. One of these differences is that the austenite stability area (FCC) is slightly smaller, and the temperatures at which this phase is the only phase present are in the range of 690-1340 ˚C (solution annealing). The temperatures at which martensite (BCC), Mu, and Ni_3Ti are formed are slightly higher. The number of segregates is relatively equal at temperatures below 450 ˚C.

Figure 4 – Mass fraction diagram of grade 300 and 350 maraging steel

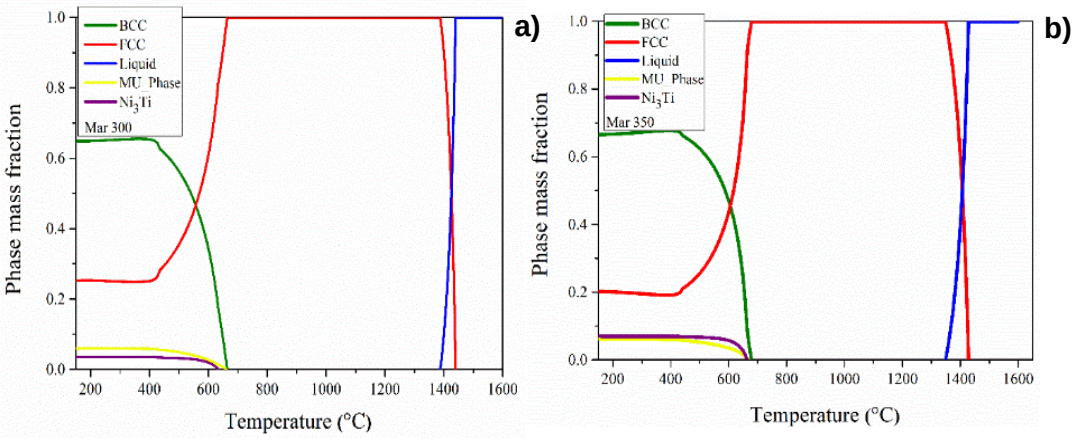

Source: Author (2021).

The prior austenite grain boundaries of the solution annealed steels condition, area observed in Figure 5a (for maraging 300) and Fig 5b (for maraging 350), the average grain size is 24.6 μm and 108.69 μm, respectively, all the values are indicated in Table 4. Figure 5c and 5e show the SEM images of the microstructure of this material (of grade 300 and 350 respectively) comprises well-defined martensite laths and is similar in all heat-treated conditions.

In the same way, Figures 5e and 5f show the prior grain boundaries of grade 300 and 350 maraging steel respectively, both solution annealed at 840 ºC for 1 h and aged at 480 ºC for 3 h, while the martensitic microstructure for both steels is shown in Figures 5g and 5h. The average grain size is 28.6 μm and 103.4 μm, respectively. In the microstructure, it was possible to observe the martensite laths along the characteristic grains. The prior grain boundaries of the grade 300 and 350 maraging steels, solution annealed at 840 ºC for 1 h and aged at 560 ºC for 1 h, are shown in Figure 5i and Figure 5j, and the average grain size is 28.1 μm and 107.2 μm, respectively. SEM images of grade 300 (Figure 5k) and 350 (Figure 5l) show the typical martensite laths of the microstructure.

Figure 5 – Optical microscopy images and SEM of the microstructure of the solution annealed at 840 °C, aged at 480 °C and aged at 560 °C conditions

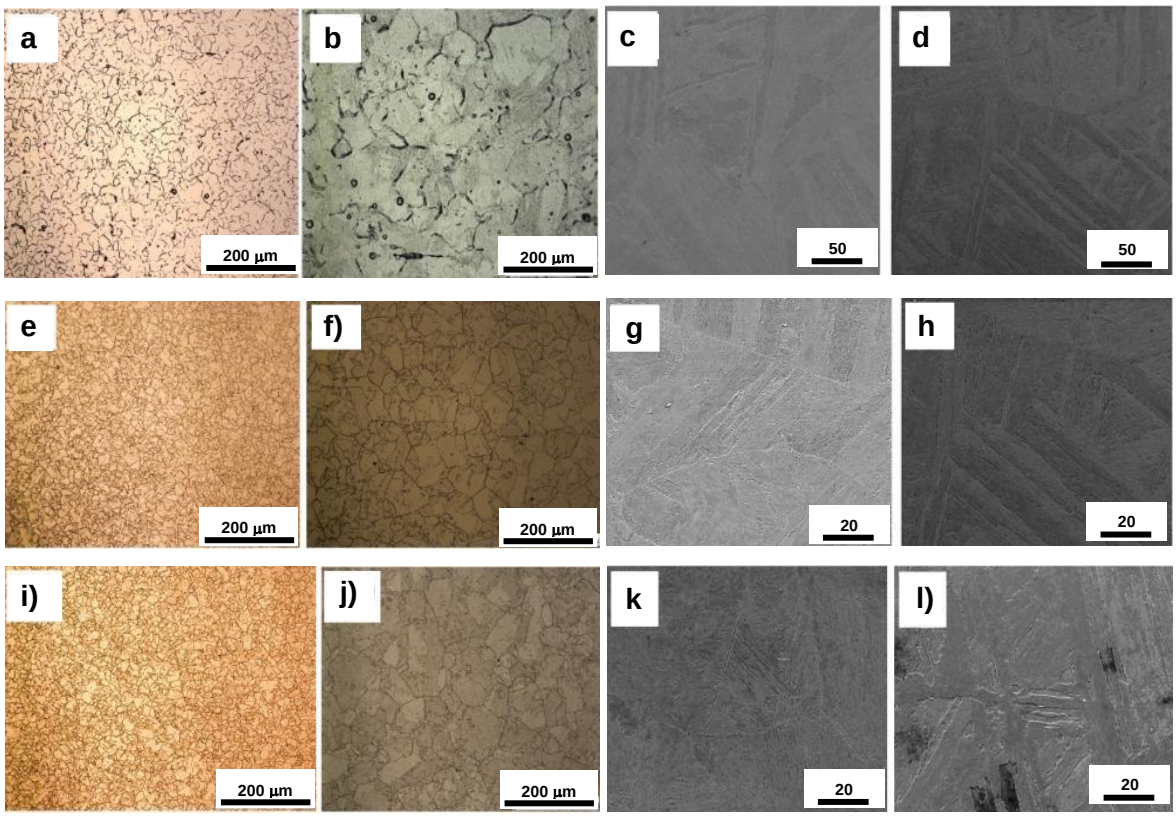

Source: Author (2021).

Figure 6a shows the diffractograms of grade 300 and 350 maraging steels solution annealed at 840 ºC for 1 h. Only peaks of body-centered cubic (BCC) α' phase are found (SILVA *et al*., 2019). This transformation occurs because of the high nickel content, the low carbon content and the shear phenomenon, and it is a structural modification that occurs with any cooling rate. The martensite formed is softer and more resistant than the tetragonal one (BCT) (LIMA FILHO; BARROSA; GOMES DE ABREU, 2017; MASOUMI *et al*., 2019; SANTOS *et al*., 2015). Figure 6b shows the diffractogram of grade 300 and grade 350 maraging steels solution annealed at 840 ºC for 1 h and aged at 480 ºC for 3 h. It can be observed that the existing peaks are the same as in the solution annealed condition and correspond to 100% of the α' martensite phase (BCC), which is characteristic of this material, with orientation {111}, {200} and {211} (SILVA *et al*., 2019). It is also worth mentioning that the intermetallic precipitates produced during aging were not found in the diffractograms. According to Santos *et al*. (2015) and Lima Filho, Barrosa and Gomes de Abreu (2017), this is due to the technique limitations to detect fractions below 5% in volume.

Figure 6c shows the diffractogram of grade 300 and grade 350 maraging steels solution annealed at 840 ºC for 1 h and aged at 560 ºC for 1 h. It can be observed that the existing peaks are the same as in the previous conditions and correspond to the α' martensite phase (BCC), but peaks were also found corresponding to the γ- austenite phase (FCC) in both steels, with orientation {111}, {200} and {220} (CONDE *et al*., 2019). The volume fraction of reverted austenite was determined using the direct comparison method described in the literature (PARDAL *et al*., 2006; SANTOS *et al*., 2015), with 13 vol.% on grade 350 maraging steel and 8 vol.% on grade 300 maraging steel, approximately. The austenite precipitation during aging is attributed to the nickel and molybdenum contents in both martensite and intermetallic compounds. Austenite precipitates in the contours of the martensite slats, absorbing these elements from the dissolution of the martensite into intermetallic compounds rich in Ni, Ti and Mo (SANTOS *et al*., 2015; SILVA *et al*., 2019).

To complement the previous result, Figure 7 shows SEM/EBSD images taken from the sample of grade 300 maraging steel aged at 560ºC for 1 h. In Figure 7a, a general area is shown where thin slats with high relief corresponding to another phase are observed. Figure 7b shows the area where the EBSD analysis was performed and where the previously mentioned slats are also seen, and in Figure 7c it is possible to see the EBSD phase map showing the BCC martensitic matrix that confirms reverted austenite (slat-shaped austenite) as described by Santos *et al*. (2020). Figure 7d shows the color key for the phases. Likewise, no intermetallic compounds were detected by XRD and EBSD in this condition.

Figure 6 – X-ray diffraction pattern of the grade 300 and 350 maraging steel samples solution treated at 840 ˚C (5a), aged at 480 ˚C for 3 h (5b), and aged at 560 ˚C for 1 h (5c)

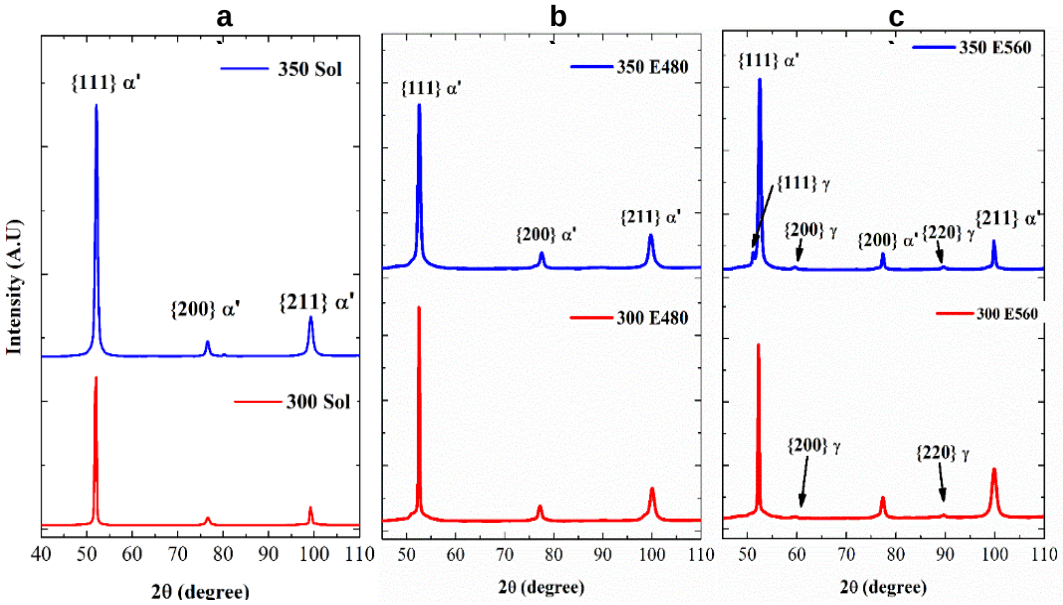

Source: Author (2021).

Figure 7 – SEM/EBSD image for the sample of grade 300 maraging steel aged at 560 ºC for 1 h. In (a) the general region for the analyses, (b) selected region for the EBSD analyses, (c) EBSD map detecting the phases and (d) color legend for the phases

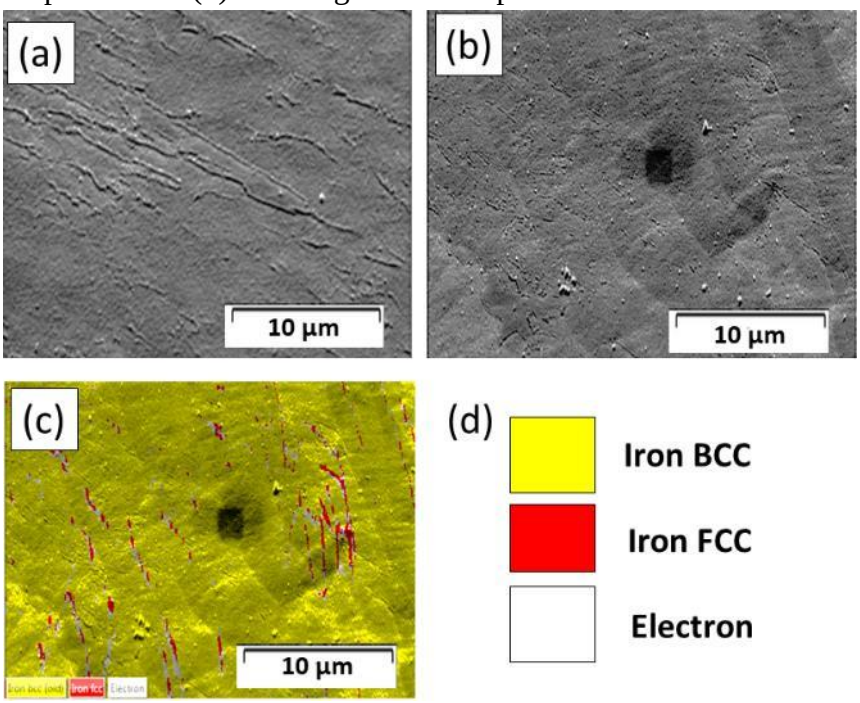

Source: Author (2021).

Table 4 shows the hardness measurements and the grain size for each heat treatment carried out in both maraging steels grades 300 and 350. According to the results, steels in the solution annealing condition have an average hardness lower than in the aged condition, and among them grade 350 maraging steel showed slightly higher values when compared with grade 300 maraging steel. This difference could be explained by the chemical composition of the steels, according to Lima Filho, Barrosa and Gomes de Abreu (2017), who analyzed the solution treatment at various temperatures, indicating that at temperatures above 1000 ºC, Ni_3Ti precipitation could occur in grade 300 maraging steels. With a temperature of 840 ºC, the considerable increase of titanium content in grade 350 maraging steel (twice as much as grade 300 maraging steel) could have caused the formation of this compound at the temperature used in this work. This can be confirmed by the thermodynamic diagrams in Figure 4. They clearly show that the temperature for the formation of Ni_3Ti increases and the amount of Ni_3Ti formed in grade 350 maraging steel is higher when compared with the diagram for grade 300 maraging steel.

Table 4 – HRC hardness and prior austenite grain size of the grade 300 and 350 maraging steels in all the conditions studied.

Steel	Condition	Average hardness (HRc)	error	Grain size (µm)
Mar 300	Sol. 840/1h	34	0	24.6
Mar 350	Sol. 840/1h	38	0	108.6
Mar 300	Sol. 840/1h + Aged 480/3h	53.75	0.5	28.6
Mar 350	Sol. 840/1h + Aged 480/3h	58.75	1	103.4
Mar 300	Sol. 840/1h + Aged 560/1h	50.75	1	28.1
Mar 350	Sol. 840/1h + Aged 560/1h	55.75	1.9	107.2

Source: Author (2021).

The analysis of the aging conditions shows that grade 350 maraging steel had greater hardness than grade 300 maraging steel because of the higher amount of cobalt and titanium found in the former. The effect of cobalt on the precipitation of intermetallic compounds formed by molybdenum, nickel, and titanium during aging is well known (MAGNÉE *et al.*, 1974; VISWANATHAN; DEY; SETHUMADHAVAN, 2005). Understandably, a greater amount of cobalt and titanium in grade 350 maraging steel increases the amount of precipitates, leading to a greater hardness in the material when compared with grade 300 maraging steel.

When comparing the values obtained from the two types of aging, aging at 560 ºC for 1 h resulted in an average hardness lower than the in the aging at 480 ºC for 3

h. This can be explained by the formation of reverted austenite. The precipitation of this phase during the aging of maraging steel leads to a decrease in their mechanical properties (MAGNÉE *et al*., 1974; RACK; KALISH, 1971; SANTOS *et al*., 2015; SILVA *et al*., 2019). This is because of the dissolution of intermetallic compounds rich in nickel and molybdenum and the transformation of martensite into austenite, and the decrease in these phases impairs the mechanical properties (RACK; KALISH, 1971; SILVA *et al*., 2019; VISWANATHAN; DEY; SETHUMADHAVAN, 2005). In all conditions studied, the grains of the grade 350 maraging steel were bigger than the grains of grade 300 maraging steel, which can be an effect of the composition or manufacture process of these steels.

The curves for the open circuit potential, linear polarization, and EIS are shown in Figure 8a, 8b and 8c, respectively. The OCP values were taken with the sample in equilibrium with the solution. The corrosion current density values were obtained using the Tafel curves, while the corrosion resistance value was estimated considering the initial value of the arc along with the resistance value of the solution by extrapolating the arc to the point where it would cut the Z real axis.

Figure 8a shows the OCP curves of maraging steels in hydrofluoric acid solution for all conditions studied. The quantitative results for the OCP measurements are shown in Table 5. Changes in the potential and direction of each curve show that the reactions are taking place on the surface, which indicates their electrochemical nature (EL-MAHDY *et al.*, 2013). The solution treated samples (300 Sol and 350 Sol) in general showed a more noble behavior than the aged samples, in accordance with Poormina, Nayak and Shetty (2010), El-Mahdy *et al*. (2013), Madhusudhan Reddy and Srinivasa Rao (2015) and Avelino *et al*. (2018), and the curve of grade 350 maraging steel showed more noble potentials than grade 300 maraging steel. This can be associated with the greater amount of alloying elements such as cobalt and titanium in grade 350 maraging steel. It can also be observed that between the two aging conditions, samples treated at 480 ºC (300 E480 and 350 E480) showed a more noble behavior than those treated at 560 ºC (300 E560 and 350 E560), which can be attributed to the fact that no austenite was formed in the first condition. Finally, it should be noted that according to the curves and the E_{ocp}, in the two aging conditions studied, grade 300 maraging steel showed a relatively more noble behavior than grade 350 maraging steel. This can be associated with the greater amount of precipitated intermetallic compounds in grade 350 maraging steel when compared with the aged grade 300 maraging steel.

Figure 8b shows the linear potentiodynamic polarization curves for both maraging steel grades under study and Table 5 shows the corrosion potential (Vcorr) and corrosion current density (Icorr). The analysis of these curves shows that none of the maraging steel grades had passivation in the anodic branch as reported by Poormina, Nayak and Shetty (2010), Sanatkumar, Nayak and Shetty (2012), El-Mahdy *et al.* (2013) and Madhusudhan Reddy and Srinivasa Rao (2015), who studied the behavior of these steels in acid solutions. The same behavior found in OCP curves can also be found in the linear potentiodynamic polarization curves. The solution annealed samples showed better performance than the aged ones. Among the aged samples, samples 300 E480 and 350 E480 showed better performance than samples 300 E560 and 350 E560, and in all aging conditions, grade 300 maraging steel showed better results than grade 350 maraging steel.

The solution treated sample of grade 350 maraging steel had a more noble corrosion potential (V_{corr}) than the other samples. The I_{corr} for the other samples were about the same, but the corrosion potential varied. Thus, the noblest behavior was found for the sample 300 Sol, followed by 300 E480, 350 E480, 300 E560, and finally 350 E560, similarly to the OCP results. The behavior in the cathode branch of all curves is similar. According to El-Mahdy *et al*. (2013), the evolution of hydrogen reduction reaction on the steel surface is under activation control, while the anodic branch suggests dissolution of the material. The absence of film formation can be explained by observing the studies of Poormina, Nayak and Shetty (2010), Sanatkumar, Nayak and Shetty (2012), El-Mahdy *et al*. (2013) and Madhusudhan Reddy and Srinivasa Rao (2015), where the samples were immersed in solutions with phosphoric acid and hydrochloric acid. These studies mention the reactivity of the phosphorus ions and mainly the chlorine ion as the causes for the breakdown of the formed protective film, allowing the solution to continue dissolving the material. In this study, it is possible to associate the same behavior due to the well-known reactivity of the fluoride ion.

The impedance curves in Figure 8c and Table 5 show the corrosion resistance values, confirming the same behavior pattern found in both OCP and polarization curves. They show that the solution annealed samples had a larger capacitive loop than the aged ones, and among these samples, those treated at 480 ºC had a larger loop than those treated at 560 ºC. It is also possible to state that the semicircular shape of the arcs shows that corrosion is controlled by the charge transfer process between the solution and the metal surface (AVELINO *et al.*, 2018; SANATKUMAR; NAYAK; SHETTY, 2012). It is

important to highlight how the effect of the chemical composition and the intermetallic precipitates formed during the aging cause a decrease in the corrosion resistance of the material. This occurs due to differences in composition between the formed phases, with a more noble behavior in the solution annealed condition, and between the two steels, with grade 350 maraging steel showing better corrosion resistance because of its greater amount of alloying elements such as titanium and cobalt. In the aging condition, grade 300 maraging steel showed better behavior, and the samples treated at 560 ºC had the lowest capacitive arc due to the influence not only of intermetallic compounds but also of the reversion of austenite in their microstructure.

Figure 8 – OCP curves (8a), Linear polarization curves (8b) and EIS (Nyquist) curves (8c) of the grade 300 and 350 maraging steels in 0.01M HF aqueous solution

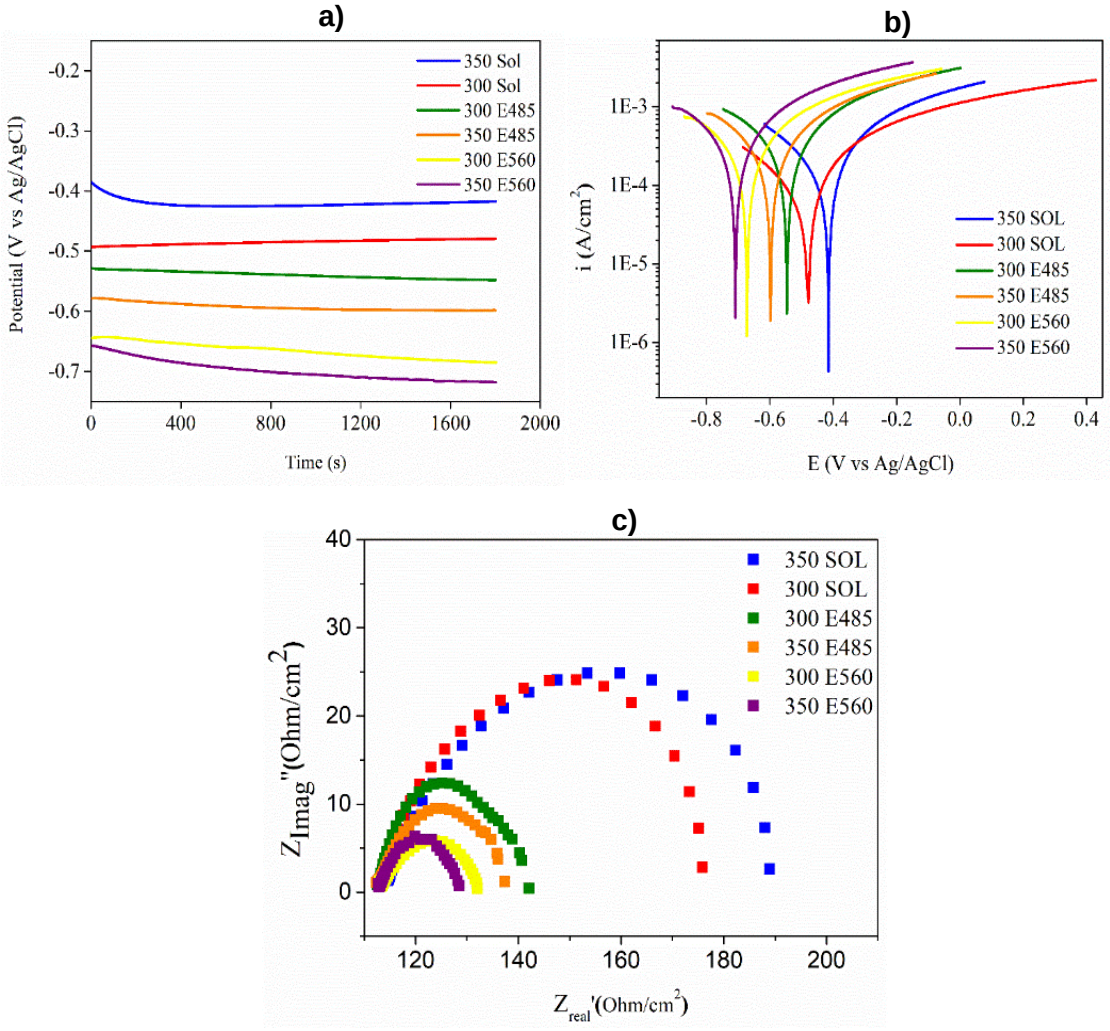

Source: Author (2021).

Table 5 – Electrochemical parameters taken from the electrochemical tests

Sample	$Z_{real'}$ (Ohm/cm^2)	OCP (V vs Ag/AgCl)	E_{corr} (V vs Ag/AgCl)	I_{corr} (A/cm^2)
350 Sol	76	-0.42	-0.42	1.57×10^{-4}
300 Sol	63	-0.48	-0.48	1.28×10^{-4}
300 E480	29	-0.54	-0.54	1.97×10^{-4}
350 E480	24.5	-0.60	-0.60	1.70×10^{-4}
300 E560	19.3	-0.68	-0.68	1.70×10^{-4}
350 E560	15.5	-0.71	-0.71	2.30×10^{-4}

Source: Author (2021).

The behavior of each steel can be explained according to the corrosion potential, current density, capacitive arc, as well as the chemical composition and the microstructure of the material. With solution annealed maraging steels, their behavior may have been influenced by the distribution of the alloy elements and uniformity of the martensitic phase, and the good performance of grade 350 maraging steel is mainly due to the higher content of cobalt and titanium. The poor performance of aged steels is due to the precipitation of intermetallic compounds during the aging heat treatment. This precipitation leads to the depletion from the metallic matrix of elements such as nickel, molybdenum and titanium, which are known for their good corrosion resistance. As a result, small galvanic piles are formed, reducing the corrosion resistance of the material (EL-MAHDY *et al.*, 2013; POORMINA; NAYAK; SHETTY, 2010; SANATKUMAR; NAYAK; SHETTY, 2012).

With samples aged at 480 ºC, small, deformed loops were formed linking the capacitance distribution with the inhomogeneity on the electrode surface (SANATKUMAR; NAYAK; SHETTY, 2012). Grade 300 maraging steel had a higher capacitive arc than grade 350 maraging steel, which can be explained by the chemical composition of the steels. The steel with higher cobalt and titanium content could be expected to have better corrosion resistance. However, as mentioned earlier, during aging, the higher cobalt content leads to greater precipitation of the intermetallic compounds, while the higher titanium content causes the formation of more precipitates, thus improving the mechanical properties but also decreasing the corrosion resistance by increasing galvanic pairs between the intermetallic phases and the steel matrix. This same relationship applies to the steels aged at 560 ºC.

The poorer corrosion resistance of the steels aged at 560 ºC results from precipitation of austenite inside the material, as mentioned before. The reverted austenite is rich in nickel and molybdenum, forming a new focus of galvanic pair within the metal

together with the increase in the interphase between austenite and martensite, which are areas more reactive to corrosion (EL-MAHDY *et al.*, 2013; MADHUSUDHAN REDDY; SRINIVASA RAO, 2015).

Figure 9 shows the SEM images of the sample surfaces after the polarization test, corresponding to 300Sol (Figure 9(a)), 300E480 (Figure 9(b)), 300E560 (Figure 9(c)), 350 Sol (Figure 9(d)), 350E480 (Figure 9(e)) and 350E560 (Figure 9(f)). A surface covered with a thin layer of high degradation can be observed in all samples. It is also possible to observe pits and cracks in some areas of the material, suggesting dissolution. These cracks and pits have similarities with the degradation found by Masoumi *et al.* (2019), Dai *et al.* (2020) and Pawel *et al.* (1994). This degradation arises from the hydrogen reaction and inter-granular corrosion caused by the stress produced by the precipitation of intermetallic compounds in the grain boundaries and the preference of the HF to dissolve these regions, as mentioned in the literature (BELLANGER; ROMEAU, 1996; CRUM *et al.*, 1999; DAI *et al.*, 2020; MASOUMI *et al.*, 2019; MADHUSUDHAN REDDY, G.; SRINIVASA RAO, 2015; PAWEL, 1994; POORMINA; NAYAK; SHETTY, 2010; 2011; ZHANG *et al.*, 2014).

Figure 9 – SEM images of the surface degradation of 300 (a, b, c) and 350 (d, e, f) maraging steels after polarization tests

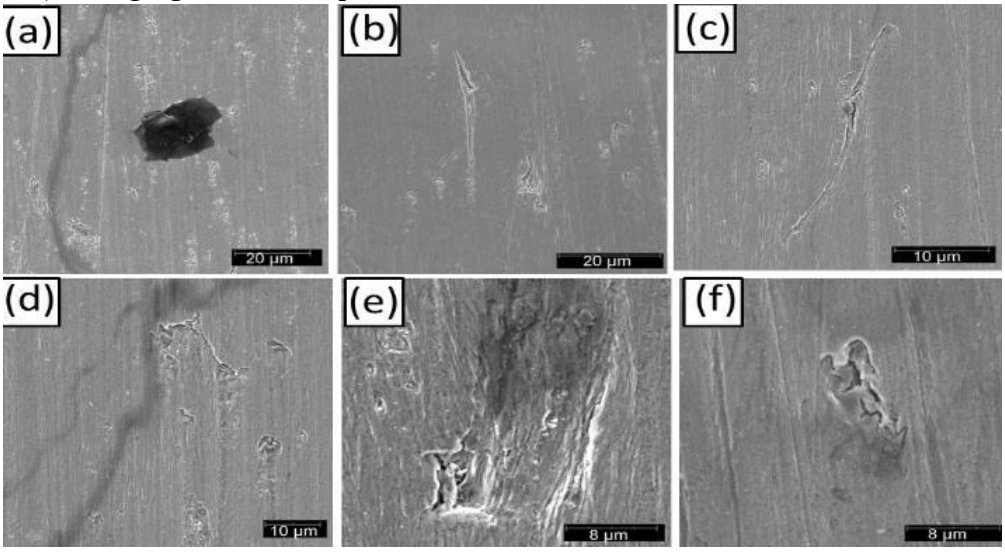

Source: Author (2021).

Linear EDS analysis was also performed on the surface of the steels. This result is shown in Figure 10a and Table 6. The chemical composition detected in the most degraded areas showed fluorine and oxygen, together with the alloying elements of the

steel. No morphological differences were found between the surfaces of grade 300 and grade 350 maraging steels under the conditions studied, but slight differences were found in the amount of elements in the corrosion product. With grade 350 maraging steel, more cobalt and titanium were detected, which is the opposite result of grade 300 maraging steel. Figure 10b shows that the areas most affected by degradation had increased percentage of fluoride in the chemical composition of the corrosion product.

Table 6 shows the quantification of the chemical composition at points A (inside the dark crack) and B (degraded surface) on the degraded surface of grade 350 maraging steel in Figure 10a. The large molybdenum content found is attributed to the formation of oxide in this metal. According to Zhang *et al*. (2014) this oxide has good stability in solutions with hydrofluoric acid, but the great affinity of iron, nickel, and cobalt to react with fluorine reduces the passive character of this oxide. Note that the oxygen and fluorine in the tables of this study have only been taken into account for illustrative purposes.

Figure 10 – a) SEM image and b) Linear EDS of the degraded surface of the grade 350 maraging steels

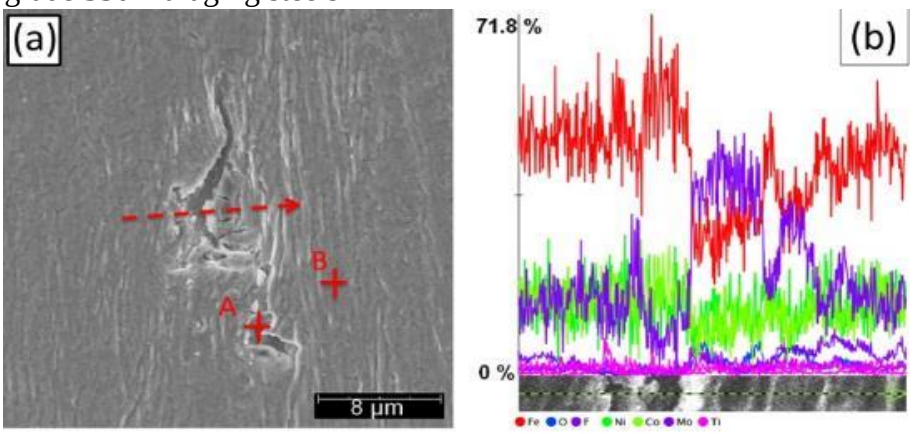

Source: Author (2021).

Table 6 – Spot EDS measurements taken at the locations shown in the SEM image in Figure 10a

EDS quantitative analysis from A and B points (wt. %)			
Element Number	**Element Symbol**	**Point A**	**Point B**
26	Fe	48.34	49.43
8	O	4.75	6.84
9	F	15.02	9.69
27	Co	9.60	9.81
28	Ni	14.94	14.36
42	Mo	6.61	8.71
22	Ti	1.04	1.16

Source: Author (2021).

Figure 11 shows two Raman spectra of the steel surface after polarization tests, one for grade 300 and the other for grade 350 maraging steel. It is important to highlight that the study presented by Avelino *et al*. (2018) was used as a reference to show the possible corrosion products formed on the steel surface, considering that no references were found in studies related to corrosion resistance in maraging steel using HF solution. It was necessary to observe the few existing studies involving these steels with other acid solutions. The peaks found in samples of grade 300 maraging steel correspond to hematite Fe_2O_3 (293 cm^{-1}, 611 cm^{-1} and 1321 cm^{-1}) (DE FARIA; LOPES, 2007; GUO *et al.*, 2020), FeF_2 (370 cm^{-1}, 500 cm^{-1} and 1080 cm^{-1}) (CHINN; ZEIGER, 1971), NiO (740 cm^{-1}, 910 cm^{-1} and 1040 cm^{-1}) (MIRONOVA-ULMANE *et al.*, 2007), MoO_3 (667 cm^{-1}, 822 cm^{-1} and 1006 cm^{-1}) (ZHAO *et al.*, 2020), and CoF_2 (787 cm^{-1}, 1118 cm^{-1} and 1214 cm^{-1}) (HOFF; GRUNGERG; KONINGSTEIN, 1972). In all conditions studied for grade 350 maraging steel, in addition to the previous compounds, TiO_2 peaks were also found (220 cm^{-1}, 440 cm^{-1} and 605 cm^{-1}) (ABDULLAH *et al.*, 2020; MAZZA *et al.*, 2007). This can be attributed to the greater number of this element in this steel, which produces this oxide on the metal surface. The formation of all these corrosion products is the result of the HF dissociation process in H+ and F- ions (YU *et al*., 2015).

Figure 11 – Raman spectrum collected from the surface samples after polarization tests

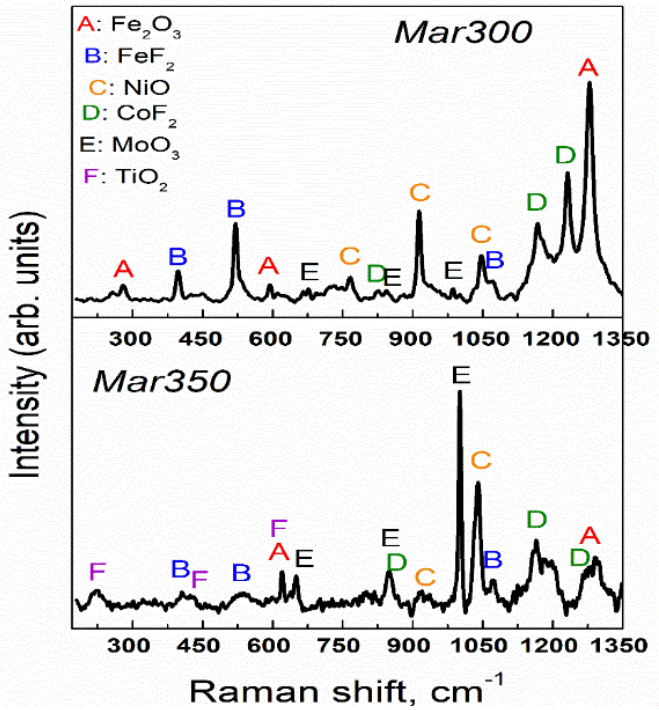

Source: Author (2021).

Fluoride ion is highly reactive and reacts very easily with the alloying elements of the maraging steel, forming compounds of Metal-F_2 (MF_2) type (BARZASHKA; OELRICH, [*s.d.*]; BRADHURST; HEUER, 1981; CRUM *et al.*, 1999), such as MoF_2, TiF_2, FeF_2, CoF_2, NiF_2. Soon after, depending on the HF concentration (low), some of these compounds react with water to form oxides according to the reaction in reaction 3 (CRUM *et al.*, 1999).

$$MF_2 + H_2O \rightarrow MO + 2HF \quad (3)$$

Together with the previous reaction that provides oxygen, it is possible to form the MoO_3, Fe_2O_3, NiO, and TiO_2 oxides found on the steel surface. MoO_3 and TiO_2 oxides are known as protectors, but the low amount of these elements in steel is not sufficient to cover the entire surface (ZHANG *et al.*, 2014), and a large amount of iron and nickel leads to the formation of much more Fe_2O_3 and NiO, which are not protective. It is important to observe the formation of HF that causes the continuous steel dissolution reaction. An important finding of Dai *et al.* (2020) and Zhang *et al.* (2014) shows that iron has a high affinity to the reaction with fluorine and that the availability of this element increases the dissolution rate.

4.1.3 Conclusions

The results of the tests showed the effect of chemical composition and heat treatments on the microstructure, mechanical properties, and corrosion resistance of grade 300 and grade 350 maraging steels.

The effect of the chemical composition led to some changes in the areas of phase stability shown in the thermodynamic diagrams. Although these results are similar in the two steel grades studied, some temperatures and quantities (mainly of intermetallic compounds) showed significant variations.

The maraging steels in the solution annealed condition showed a completely martensitic microstructure. Due to their size, it was not possible to detect and observe the intermetallic compounds precipitated in the aged conditions. The hardness values allowed to evaluate the influence of aging heat treatments on the well-known mechanical

properties of these steels. Grade 350 maraging steel showed a higher hardness in all conditions, as expected. Both steels showed their lowest hardness values in the solution annealed condition. Among the aging conditions, it is possible to confirm that the aging condition at 480 ºC for 3 h resulted in the highest hardness values because of the precipitation of nanometric intermetallic compounds. Lastly, the samples aged at 560 ºC for 1 h showed a decrease in the hardness values precisely because of the reversion of austenite for both steels, which was detected by XRD and EBSD.

The electrochemical results showed that aging has a negative effect on the corrosion resistance of maraging steels. Solution annealed steels had a more noble behavior, and in this heat treatment condition, the higher amount of cobalt and titanium resulted in better corrosion resistance in grade 350 maraging steel compared to grade 300 maraging steel. The higher amount of intermetallic precipitates due to the increase of cobalt and titanium in grade 350 maraging steel decreased its corrosion resistance against grade 300 maraging steel in the aged conditions. This effect is caused by a larger area of phase contours and chemical composition differentials between the martensitic phase and these nanometric compounds that produce galvanic couple. In the aged conditions, it is possible to observe the effect that an additional phase (austenite) has in the decrease of the electrochemical behavior of the steels aged at 560 ºC for 1 h. A greater area of grain boundaries and composition between phases increases the susceptibility of these steels.

The high reactivity of the fluoride ion (despite the low concentration of the solution) was decisive for the reaction with the alloy elements, mainly with iron and cobalt. Raman analysis results showed the formation of fluoride cobalt and iron compounds that are the primary effect of the steel dissolution. Some oxides that should protect the material, such as MoO_3 and TiO_2, were found. However, their effect is diminished by their low quantity and the high reactivity of fluorine in the dissolution of the other elements. The morphology of the steel surface after the polarization test was also observed, showing the deterioration of the steel with many cracks associated with hydrogen susceptibility.

4.2 Oxidation behavior of maraging 300 alloy exposed to nitrogen/water vapor atmosphere at 500 ºC

4.2.1 Review

Aging heat treatments in maraging steels are fundamental to achieve the excellent mechanical properties required in several industries, i.e., nuclear, automotive, etc. In this research, samples of maraging 300 alloy were aged using a novel procedure that combines different steps with two atmospheres (nitrogen and water vapor) for several hours. The oxidized surface layer was chemical, microstructural and micromechanically characterized. Due to the thermodynamic and kinetic conditions, these gases reacted and change the surface chemistry of this steel producing a thin iron-based oxide layer of a homogeneous thickness of around 500 nm. Within the afore-mentioned information, porosity and other microstructural defects showed a non-homogeneous oxide, mainly constituted by magnetite, nickel ferrite, cobalt ferrite, and a small amount of hematite in the more external parts of the oxide layer. In this sense, from a chemical point of view, the heat treatment under specific atmosphere allows to induce a thin magnetic layer in a mixture of iron, nickel, and cobalt spinel ferrites. On the other hand, the oxide layer presents an adhesive force 99 mN, value that shows the capability for being used for tribological applications under sliding contact tests.

The present research aims to induce an oxide layer with different nature depending on the atmosphere employed during the thermal treatment on maraging 300 alloy. Subsequently, the oxide layers will be chemically, microstructural and either as under sliding contact tests. All this sub-chapter was All this sub-chapter was published in June/24/2021 in the journal METALS 11 (2021) 1021 with DOI: https://doi.org/10.3390/met11071021 (CERRA FLOREZ *et al*., 2021).

4.2.2 Results and Discussion

The diffractogram spectrum of the maraging 300 alloy after solution annealing heat treatment at 840 °C for 1 h is depicted in Figure 12. All the peaks correspond to the martensitic (α'-) phase (with a body-centered cubic structure, bcc),

characteristic of this material. The spectrum is in agreement with those reported in Viana, Dos Santos and De Abreu (2013).

Scanning electron microscope (SEM) micrograph of the surface after polishing is shown in Figure 13a, where some grinding marks are clearly visible. On the other hand, the main energy dispersive X-ray spectroscopy (EDS) chemical element maps are showed in Figure 13b. From the chemical measurement it is evident that the main elements (Fe, Ni, Co, Mo, and Ti) are homogenously distributed along the specimen after solution annealing. In this sense, no heterogeneities in terms of chemical composition are visible in the modified surface.

Figure 12 – X-ray diffraction (XRD) spectrum of the maraging 300 alloy after solution annealing treatment at 840 °C showing α'- peaks

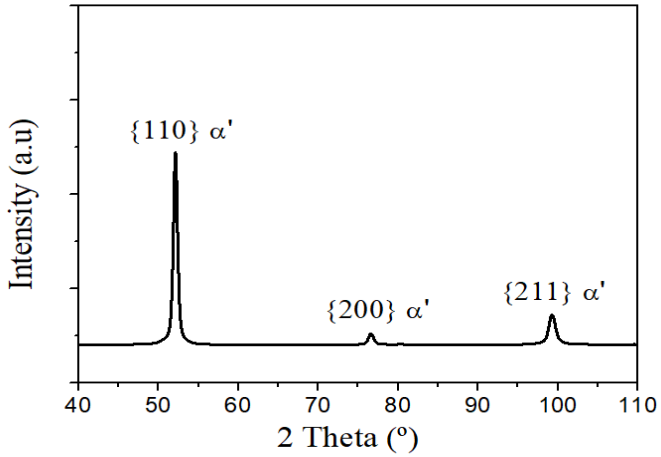

Source: Author (2021).

Figure 13 – (a) Scanning electron microscope (SEM) micrograph of the grade 300 maraging steels surface after treatment and (b) energy-dispersive X-ray spectroscopy (EDS) elements map of the main constituents

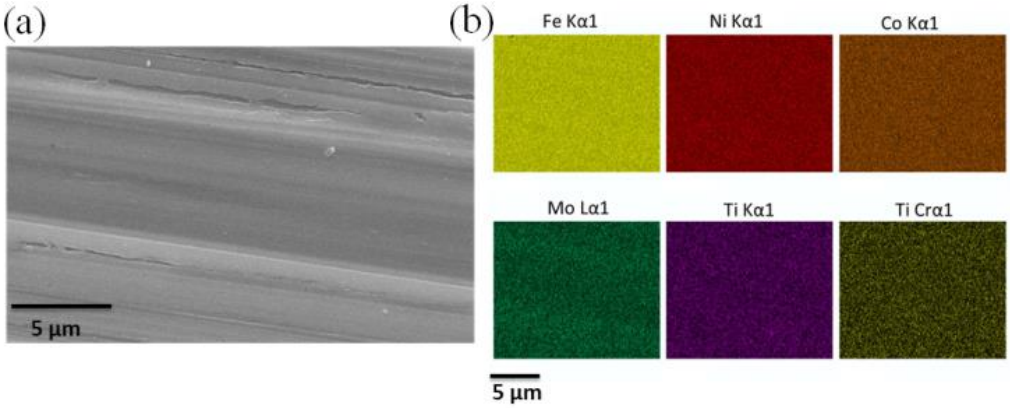

Source: Author (2021).

Figures 14a and 14b show the laser scanning confocal microscopy (LSCM) micrographs, where clearly exhibits different kinds of defects like ridges, valleys, and peeling heterogeneously distributed in the oxide layer. In order to get more details about the surface quality of the oxidation process, the morphology of the surface of these images were done by using the atomic force microscopy (AFM) technique. Figures 14c and 14d shows the topographic AFM images (3D-view) at different magnifications; 40 × 40 μm^2 and 6.6 × 6.6 μm^2, respectively. From these images it is possible to extract the main roughness parameters (i.e.: maximum roughness, maximum and minimum roughness peak; Rz, Rp and Ry, respectively), as summarized in Table 7.

Figure 14 – (a,b) laser scanning confocal microscopy (LSCM) surface micrographs observation, and topographic atomic force microscopy (AFM) image (3D view) of the (c) initial surface and (d) the oxide layer growth on maraging 300 alloy.

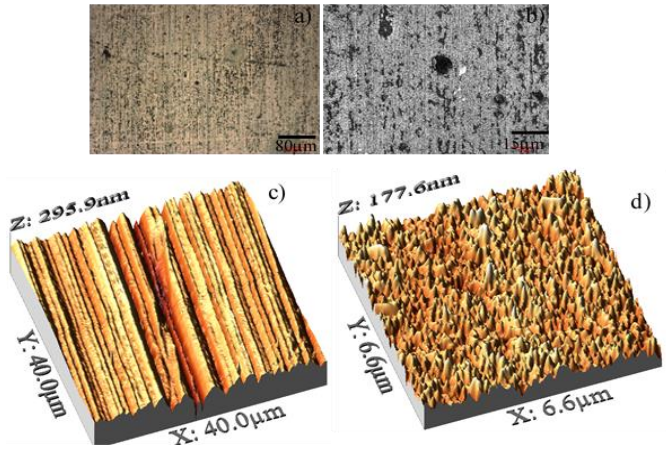

Source: Author (2021).

Table 7 – Summary of the main roughness parameters for the reference sample and the oxide layer

Roughness (nm)		
Parameter	**Steel surface**	**Oxide surface**
Roughness Average (R_a)	52 ± 5	17 ± 0.5
Roughness Maximum (R_z)	295	177
Max Peak *ht* (R_p)	110	96
Maximum Depth (R_v)	-185	-81

Source: Author (2021).

The X-ray diffraction (XRD) low angle (10º) spectra for each specimen investigated here are presented in Figure 15. Several peaks, {012}, {104}, {110}, {113}, {024}, {116}, {214} and {300}, confirm the formation of hematite (Fe_2O_3), in fair agreement with the values reported in ICDD (1975). Also, the (Fe, Co, Ni) spinel oxide

appears at {111}, {220}, {311}, {400}, {422}, {511} and {400} in agreement with Dąbrowa *et al.* (2018). On the other hand, the peak {111} at 2θ around 51°, indicates the presence of the austenitic (γ-) phase (CERRA FLOREZ *et al.*, 2021; CONDE *et al.*, 2019). This γ-phase is rich in Fe, Co, and mainly in Ni, as found in Cerra Florez *et al.* (2021), Klein, Sharon and Yaniv (1981), Klein, Yaniv and Sharon (1981; 1983) and Rezek, Klein and Yahalom (1997). This layer will act as a bonding layer and will enhance the adhesion between the oxidized layer and the metallic substrate. By using the methodology presented in Chung (1974) and Gadelmawla *et al*. (2002), it was possible to quantify the spinel and hematite contents present in the oxidized layer, being their values of 61 and 39 %, respectively. It is important to highlight that the spinel peaks present in the XRD spectrum also fit with the Fe_3O_4, $NiFe_2O_4$, and $CoFe_2O_4$, which have similar crystallographic parameters. However, this technique does not lead to isolate each contribution as reported Klein, Sharon and Yaniv (1981).

Figure 15 – X-ray diffraction (XRD) spectra of the oxide layer formed on maraging 300 alloy. Peaks corresponding to γ-phase, Hematite and (Fe,Co,Ni) spinel are visible in the spectra

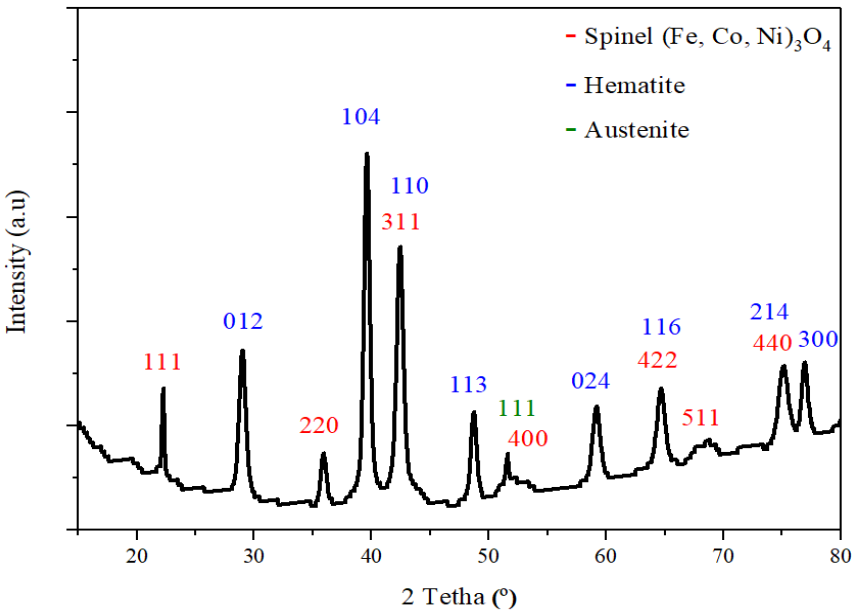

Source: Author (2021).

Scanning electron microscope (SEM) micrographs of the oxide layer are given in Figure 16. Several heterogeneities and/or defects, heterogeneously distributed along the oxidized layer, are visible (indicated with red circles). In this sense, the oxidized layer presents several nodules (Figure 16a), holes (Figure 16b), and porosity, as depicted in Figures 16c and 16d. Furthermore, several morphological irregularities with different depth, that suggest a non-homogeneous oxide layer, are depicted in Figure 16e. Finally, an oxidized cross section of the layer is shown in Figure 16f, showing a non-homogeneous layer thickness of around 2.9 ± 0.4 μm. Energy-dispersive X-ray spectroscopy (EDS) measurements made in several points A (oxide surface) and B (elongated white formations) are presented in Figure 16d and summarized in Table 8. The values obtained reveal two types of chemical compositions, one rich in Fe and the other with appreciable amounts of Fe, Co, and Ni, suggesting that the first corresponds to hematite while the second one to spinel. It is essential to indicate that oxygen was only taken into account for comparative purposes.

Figure 16 – Scanning electron microscope (SEM) micrographs of the oxide produced on maraging 300 alloy, showing different heterogeneities, such as, (a) nodules, (b) holes, (c) porosity and (d,e) depicted on the surface; and (f) cross section of the oxide layer

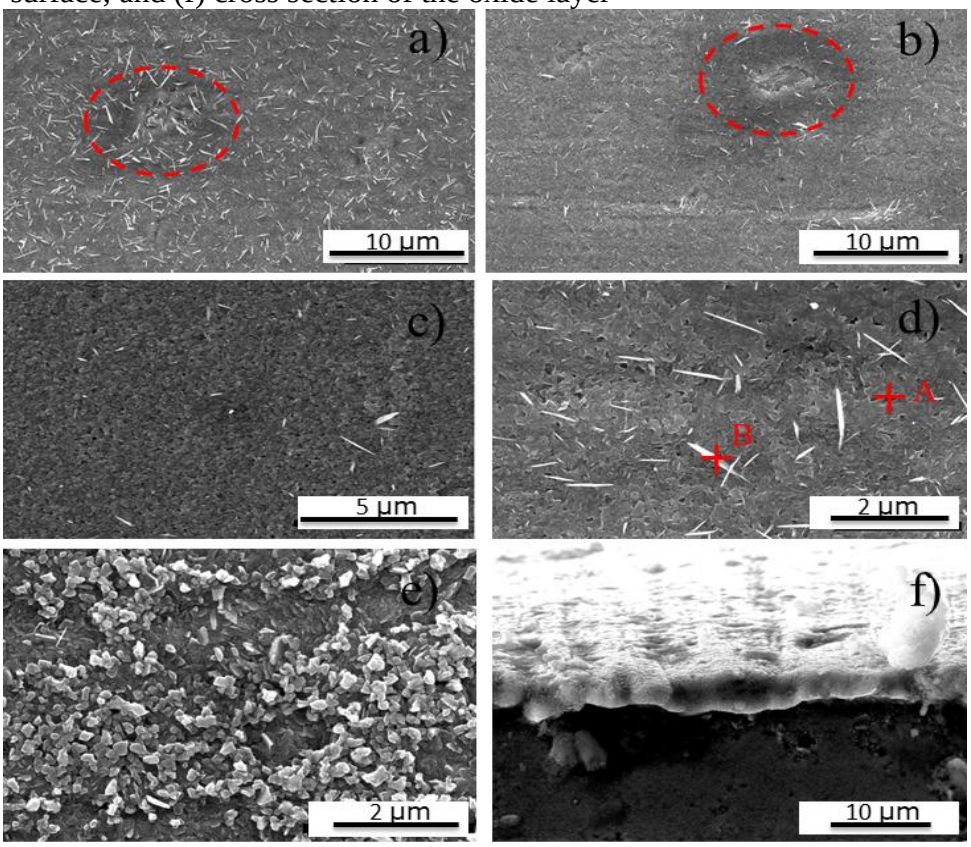

Source: Author (2021).

Table 8 – Energy-dispersive X-ray spectroscopy (EDS) analysis performed at two different points (as shown in Figure 16d)

EDS quantitative analysis from A and B points (wt. %)			
Element Number	**Element Symbol**	**Point A**	**Point B**
26	Fe	38.87	33.46
8	O	36.37	62.30
27	Co	11.19	1.91
28	Ni	12.93	2.33
42	Mo	0.54	-
22	Ti	0.10	-

Source: Author (2021).

The energy-dispersive X-ray spectroscopy (EDS) maps conducted in different zones of the oxidized surface are depicted in Figure 17. The oxide layer has a homogeneous element distribution, as presented in Figures 17a and 17b. On the other hand, when the oxide layer presents discontinuities (i.e. holes, etc.), the EDS maps highlight that this layer is enriched on Mo and Ti, while less content of Ni and Co are present in those discontinuities. Figure 17e shows the line scan (red dash line) analysis

through one of the discontinuities (being this discontinuity a detachment of the oxide layer) present in the oxide layer. This element profile is in fair agreement with the chemical maps presented in Figure 17d conducted on the red square in Figure 17c. Furthermore, this analysis confirms that within these discontinuities there is an increase in the amount of Mo and Ti, which can be associated mainly with two different phenomena: (1) the presence of titanium nitrides (TiN) formed during steel manufacture, with appreciable amounts of N and Ti (DESCOTES *et al.*, 2015; 2020), and (2) an area rich in Fe, Ni, Mo, and Ti, which leads to create different intermetallic compounds (Ni_3Ti, Ni_3Mo, Fe_3Ti, and Fe_3Mo) that precipitate during the aging treatment, in agreement with Magnée *et al.* (1974), Moshka *et al.* (2015), Petty (1970), Rack and Kalish (1971) and Rodrigues, Bernardi and Otubo (2014). It is worthy to mention that these intermetallic phases are very stable and do not form oxides, breaking the homogeneity of the oxidized layer.

In order to observe the microstructure, as well as be able to determine the oxide layer thickness, a cross section micrograph was done by means of focused ion beam (FIB) (Figure 18a). From this micrograph, it is possible to discern a homogeneous oxide layer with a thickness of around 467 ± 33 nm and a metal fine grain microstructure just below (112 ± 24 nm). On the other hand, a closer inspection (Figure 18b), dark shades are visible that suggest the presence of different phases. This assumption was confirmed by performing energy-dispersive X-ray spectroscopy (EDS) chemical analysis in three different regions (A: oxide film, B: oxide layer/metal base interface and C: metal base), as shown in Figure 18c and summarized in Table 9. It is essential to indicate that oxygen was only taken into account for comparative purposes. These results highlight that the oxidized layer presents a uniform distribution from a chemical point of view. As it is evident in Table 9, Ni shows a higher concentration in the oxide layer near the metal base interface. This fact may be related to the generation of an γ- bonding layer at the oxide layer/metal base interface, in fair agreement with Klein, Sharon and Yaniv (1981), Klein, Yaniv and Sharon (1981; 1990), Rezek, Klein and Yahalom (1997) and Cerra Florez *et al.* (2021), and also found by X-ray diffraction XRD (see Figure 15). A decreasing compositional gradient towards the surface was also observed on Figure 18d, suggesting the formation of oxide compounds. The obtained results are in concordance with those reported in Klein, Yaniv and Sharon (1981; 1990) and Cerra Florez *et al.* (2021).

Figure 17 – (a, c, e) Scanning electron microscope (SEM) micrographs (of the oxide produced on maraging 300 allow) of the analyzed surface, (b, d) Energy-dispersive X-ray spectroscopy (EDS) chemical maps and (f) chemical elements profiles conducted on the through the red dash line of the Figure 17e.

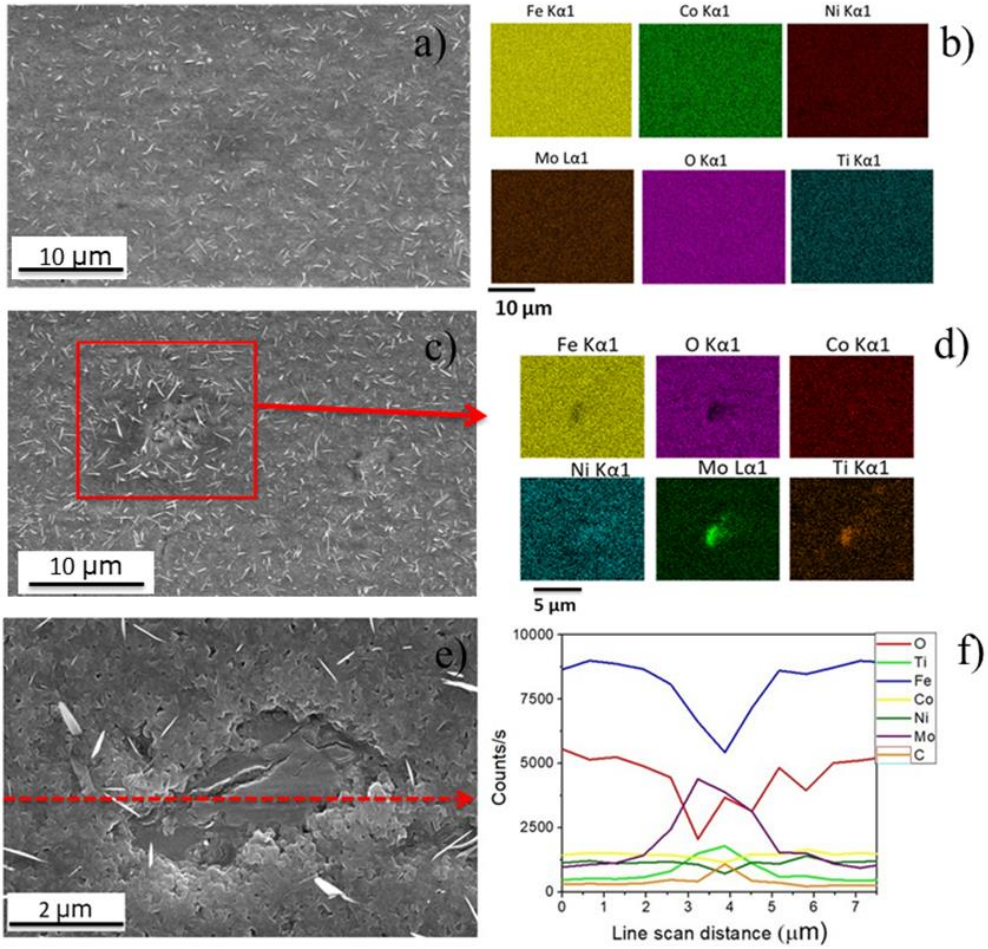

Source: Author (2021).

In order to identify the spinels, Raman spectroscopy technique was used. Figure 19a shows the Raman spectrum obtained from the oxide layer, in which it is possible to see some peaks of hematite according to De Faria and Lopes (2007) and Guo *et al.* (2020), and some of spinel's. Furthermore, by doing a magnification at a Raman shift ranged between 350 and 715 cm^{-1}, the spinel peaks are most clearly visible (see Figure 19b). Also, in the same representation it is possible to observe the hematite and spinel's (Fe_3O_4 [KUMAR *et al.*, 2014; ROBINSON *et al.*, 2019], $NiFe_2O_4$ [ROBINSON *et al.*, 2019; GAO *et al.*, 2020] and $CoFe_2O_4$ [WANG *et al.*, 2015; ROUTRAY; SAHA; BEHERA, 2020]) peaks. On the other hand, no Ti or Mo oxide peaks were found.

Figure 18 – Scanning electron microscope (SEM) micrographs of the oxide layer formed in maraging 300 alloy, (a) focused ion beam (FIB)-cross section micrograph of the oxide layer, (b) thickness of the oxide layer, c) magnification of the oxide layer showing the three different points where the chemical composition were determined, and d) energy-dispersive X-ray spectroscopy (EDS) maps analysis for different metallic elements present in the oxide later (Fe, O, Ni, Co, Mo and Ti) in the region described in Figure 18c

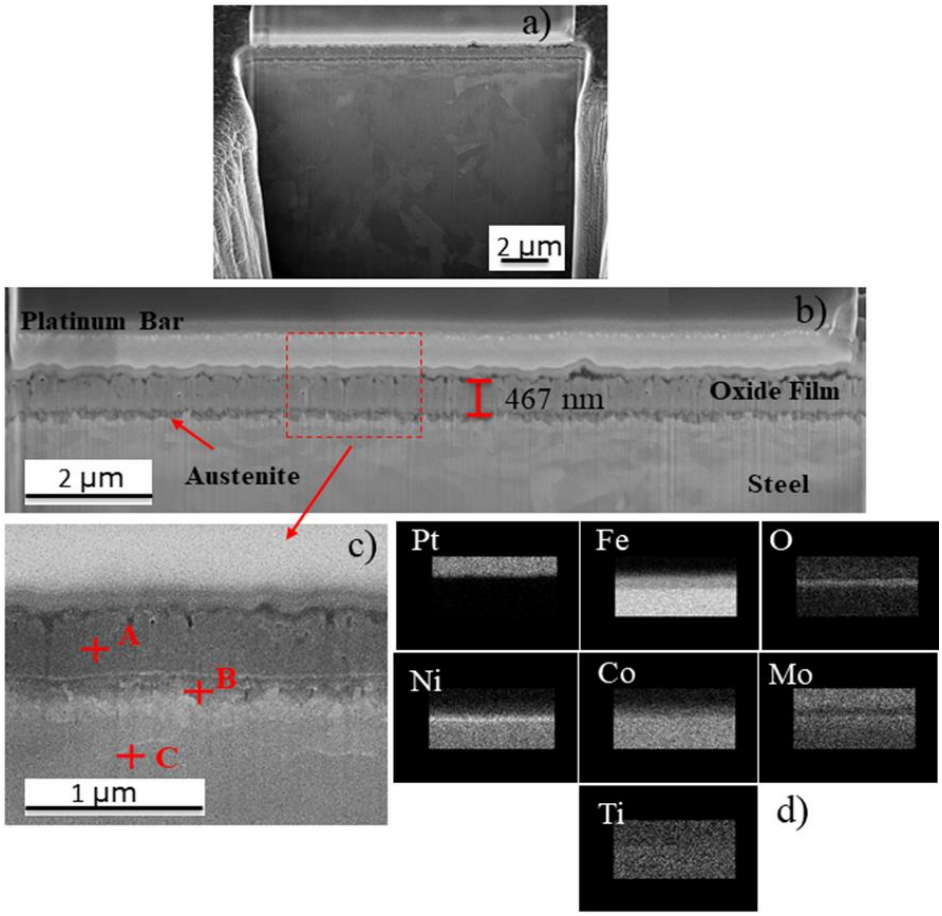

Source: Author (2021).

Table 9 – Energy-dispersive X-ray spectroscopy (EDS) measurements for the three different points shown in Figure 18d.

EDS quantitative analysis from points A, B and C (wt. %)				
Elem. Number	Elem. Symbol	Point A	Point B	Point C
26	Fe	44.08	38.11	63.69
8	O	26.07	2.33	-
27	Co	13.28	11.40	12.08
28	Ni	15.81	44.17	19.64
42	Mo	0.63	3.27	3.99
22	Ti	0.15	0.72	0.60

Source: Author (2021).

Figure 19 – Raman spectrum collected from the oxide layer produced on maraging 300 alloy, showing the main compound peaks. (a) General view and (b) a high magnification ranged between 195 and 715 cm^{-1}.

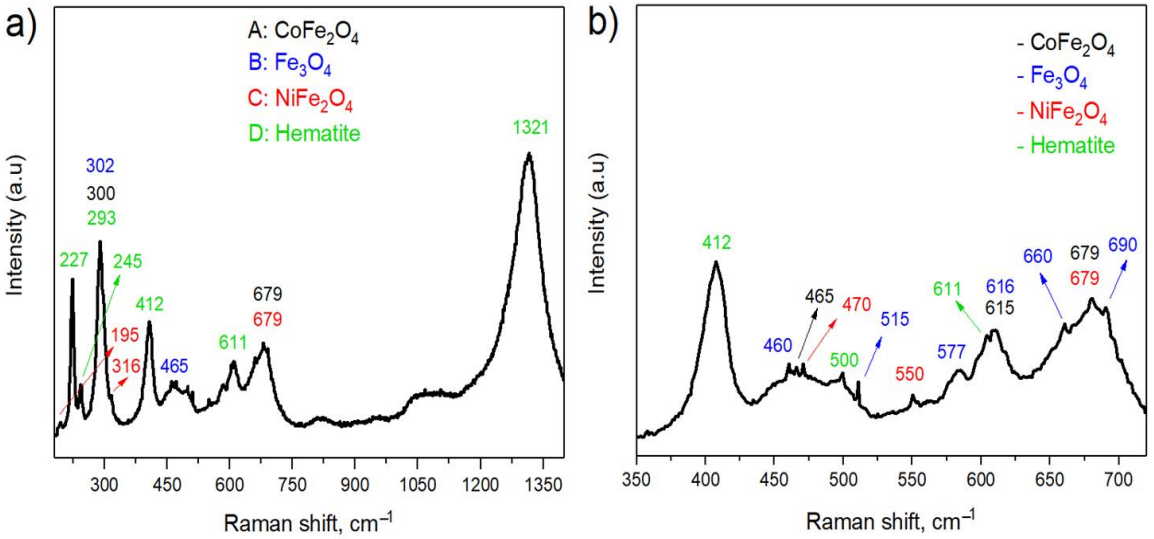

Source: Author (2021).

The highly oxidizing water vapor effect can explain the oxidation process of maraging 300 alloy at temperatures above 300 °C (LUO; SHEN, 2008). In this sense, the oxide formation has the following steps: (1) decomposition of H_2O in mixed gases, (2) adsorption of dissociated oxygen on the steel surface, and (3) reaction between oxygen ions and metal ions (KLEIN; SHARON; YANIV, 1981; LUO; SHENZ, 2008). Thus, it can be said that, in the initial stage of oxidation, metal atoms become ions that quickly diffuse together with electrons and react with oxygen to form the first layer (KLEIN; SHARON; YANIV, 1981; KLEIN; YANIV; SHARON, 1981; LUO; SHENZ, 2008). Surman (1973) and Subbaraman, Deshmukh and Sankaranarayanan (2013) identified values of the oxide formation energies for Fe, Ni, Co, Mo, and Ti, in atmospheres containing water vapor. They mentioned that all these elements oxidize at the same time in the initial stage and in the case of titanium, due to its greater reactivity, it could form TiO_2. This compound was not found in this research, but the energy-dispersive X-ray spectroscopy (EDS) maps showed a higher concentration of this element in the oxide layer/metal base interphase, indicating its existence. Authors mentioned above indicate that MoO_3, CoO, FeO, and NiO, form initially; but due to the limited diffusion rate of Ti, Mo, Co, and Ni ions, they are covered by the Fe oxide. It is also said that this oxide acts as a barrier to the migration of Mo and Ti ions.

The growing oxide layer process mainly depends on the partial pressure of oxygen at-tributed to transport of ionic species, and electrons through the formed layer (KLEIN; YANIV; SHARON, 1981). It has been explained in the literature that the oxide growth in maraging steels depends mainly on the movement of metal ions through the FeO oxide layer; that is, it grows through the oxide layer/gas interface (GREYLING; KOTZI; VILJOEN, 1990; KLEIN; YANIV; SHARON, 1981; 1983; REZEK; KLEIN; YAHALOM, 1997). Furthermore, hematite phase is formed due to the atmospheres used during aging process. Zhang *et al.* (2016) and Hong *et al.* (2019) described that during oxidation between 375 and 526 °C in atmospheres containing water vapor, the outermost layers are exposed to a higher concentration of oxygen, and part of the magnetite oxidizes to hematite ($Fe_3O_4 \rightarrow \alpha\text{-}Fe_2O_3$) (HONG *et al.*, 2019; JEON *et al.*, 2013; SUBBARAMAN; DESHMUKH; SANKARANARAYANAN, 2013; ZHANG *et al.*, 2016).

Previous works (LUO; SHEN, 2008; VISWANATHAN; DEY; ASUDI, 1993; WANG *et al.*, 2015) mentioned that during aging, thermodynamic and kinetic conditions are created that favor the preferential formation of Fe_3O_4 spinel. Small amounts of Co and Ni can be found in the oxide as substitutional combinations in the magnetite microstructure, but not forming different compounds (GREYLING; KOTZI; VILJOEN, 1990; JEON *et al.*, 2013; SUBBARAMAN; DESHMUKH; SANKARANARAYANAN, 2013). However, in this research Ni and Co ferrites ($NiFe_2O_4$ and $CoFe_2O_4$, respectively) have been found and fully identified within the oxide as it has been through the chemical and microstructural analysis presented above. This is due to the differences in the chemical composition of the studied steels because the employed maraging 300 alloy has a greater amount of Mo, Ti, and Co, and these elements, during the thermal treatment in atmospheres containing water vapor, induce an increase in the diffusion process of Co^{2+} and Ni^{2+} ions from the metal base to-wards the outer part of the material, being able to create the aforementioned oxide layer due to a replacement of Fe^{2+} ions located in the octahedral sites of the spinel transforming part of the magnetite into $NiFe_2O_4$ and $CoFe_2O_4$ (BLIEM *et al.*, 2015; DĄBROWA *et al.*, 2018; GENUSIO *et al.*, 2016; PARDAVI-HORVATH, 2000; RODRIGUES *et al.*, 2015; TSUKIMURA; SASAKI; KIMIZUKA, 1997).

Finally, in the scratch tests (used to determine the adhesive damage denoted as Pc2) there is a large shear stress on the surface caused by friction between the indenter

and the material (ATSM, 2015c; CERRA FLOREZ *et al.*, 2021; GHASEMI PARIZI *et al.*, 2020). Figures 20a and 20b shows the top-view Field emission scanning electron microscopy (FE-SEM) micrographs of the scratch track performed under linear increasing applied load up to 100 mN for the investigated specimen. The behavior is clearly discerned by com-paring the micro-fracture events and damage features in regions close to track edges. Some interesting features and damage events as decohesion are clearly visible on the sides of all grooves one can observe pileups as well as loose material in the form of flakes produced by the flow of plastically deformed material and which is responsible of the serrated shape along the scratch track. The Pc2 directly determined from the FE-SEM micrograph is 49 mN. This Pc2 value shows that the film presents excellent adherence comparing with the result published by Cerra Florez *et al.* (2021), and the results shows the capability for being used for tribological applications under sliding contact tests (ASTM, 2015c; CERRA FLOREZ *et al.*, 2021).

Figure 20 – (a) Field emission scanning electron microscopy (FE-SEM) micrograph for the nanoscratch track and (b) magnification of the top-view (FE-SEM) image of nanoscratch tracks where the first adhesive damage appears for the reference sample

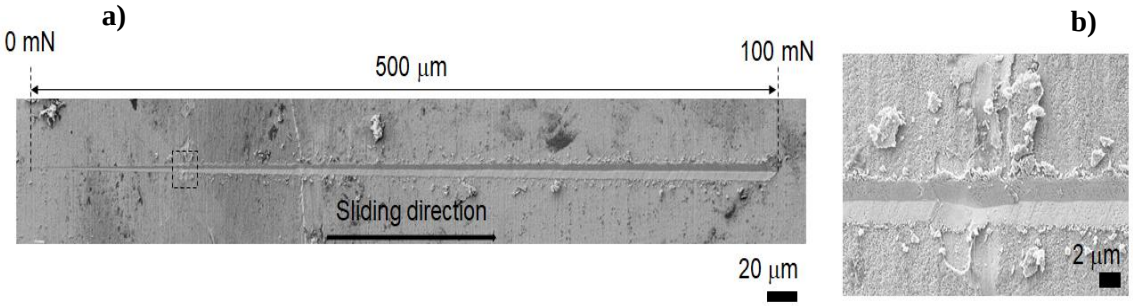

Source: Author (2021).

4.2.3 Conclusions

This study of the oxidation behavior of maraging 300 alloy in water vapor and nitrogen at 500 °C showed that, although there are considerable amounts of elements known for their corrosion resistance, the kinetic and thermodynamic phenomena did not allow the formation of oxides that could protect the steel from the chemical degradation imposed by the exposure conditions. In this sense, such phenomena are the precipitation of intermetallic compounds rich in these elements during the aging heat treatment and the more incredible iron diffusion speed through the oxide layer.

The heat treatment highlights the formation of a homogeneous oxide layer of a dual phase material (hematite and mainly spinel) of around 467 ± 33 nm, covering the entire surface with some imperfections, like holes.

From the innermost towards the oxide surface exists a variable composition that confirms the formation of different compounds due to the oxidation and diffusion of Fe, Ti, Mo, and Co. A Ni rich austenitic bonding layer is formed on the oxide layer/metal interface, contrary to the findings reported by other authors who found TiO_2, MoO_3, NiO, and CoO oxides.

Due to the chemical composition, kinetic and thermodynamic conditions during the heat treatment, there was diffusion of Co and Ni ions through magnetite initially formed and they replaced the Fe atoms that are located in the octahedral holes of the spinel's structure, being this process the main responsible of the transformation of magnetite into $CoFe_2O_4$ and $NiFe_2O_4$, as highlighted by the results obtained by Raman spectroscopy.

The scratch tests show an excellent adherence between the formed oxide layer and the metallic substrate and demonstrate its capability for being used under aggressive conditions mainly for tribological applications under sliding contact tests. The chemical and adhesion characteristics of the oxide produced make this film have potential for applications in coatings that can improve the electrochemical behavior, in addition to applications in equipment manufactured with maraging steels used for processing minerals where it is subjected to wear.

4.3 Characterization of oxides produced on grade 300 and 350 maraging steels using two oxygen rich/steam atmospheres

4.3.1 Review

The growing process of a spinel-like oxide film can be obtained through different atmospheres; in this sense Air, O_2, steam, and nitrogen atmospheres were used in different steps during the aging heat treatment at 490 ºC of maraging 300 and 350 alloys. The oxidation layer produced under different atmospheres was chemically, microstructurally and mechanically characterized by means of advanced techniques. The results showed (in both alloys) a non-homogeneous mix oxide formed by magnetite,

nickel and cobalt ferrites and MoO_3 heterogeneously distributed along the oxide thickness. It was also founded TiO_2 in the innermost areas and a particularly important quantify of hematite on the external surface. A nickel-rich austenite phase was produced at the interphase due to the combination of nickel stability and the preference of cobalt, molybdenum, and iron diffuses through the film as ions. The highest thickness values were found in the oxides produced in maraging 300 steels which could indicate greater susceptibility to oxidation comparing with grade 350 maraging steel. The oxide films produced in both maraging alloys using air atmosphere presents excellent adherence, and the results show the capability for being used for tribological applications under sliding contact tests.

In the present article an oxide spine layer was investigated on two different maraging alloys (300 and 350) by using two atmospheres (synthetic air and O_2) at 490 ºC, procedure similar to applicated by Cerra Florez *et al.* (2021). Subsequently, the spinel layer for both maraging alloys were chemically, microstructurally and also tribologically investigated at the micrometric length scale.

4.3.2 Results and Discussion

Figure 21 exhibits the X-ray diffraction spectra for the maraging 300 and 350 alloys prior induce the oxide layer (also labeled as reference samples). Three main peaks are visible in both spectra -{110}, {200} and {211}-, which corresponds to martensite α' in agreement with the data reported in Conde *et al*. (2019) and Viana, Dos Santos and De Abreu (2013).

Figure 21 – X-ray diffraction (XRD) spectra for the different reference maraging alloys investigated here

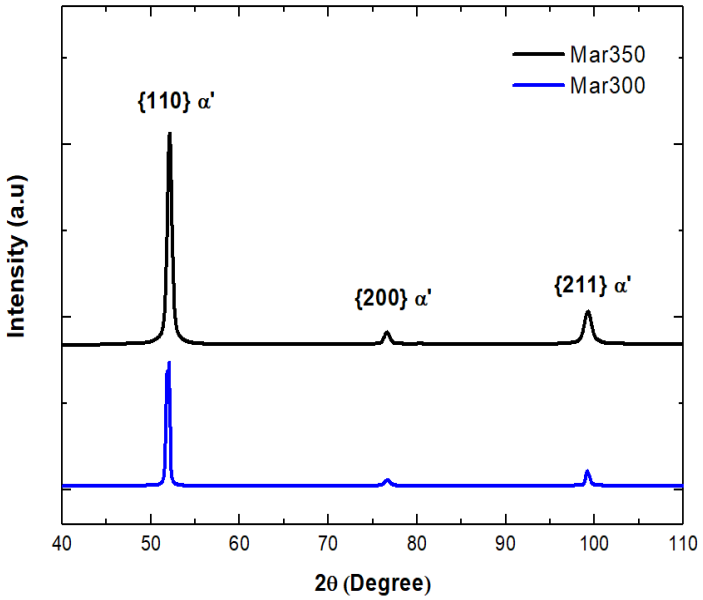

Source: Author (2021).

Figure 22 shows the X-ray diffraction (XRD) low angle spectra of the different oxide layers growth in both maraging alloys investigated here. Two different heat treatments were analyzed; (1) oxide layer produced in Air/Steam/N_2 atmospheres (Figure 22a) and (2) produced in O_2/Steam/N_2 atmospheres (Figure 22b). All oxide layers present the same kind of phases labeled as A, B, C, D and E. The phase labelled as A, which corresponds to a spinel ferrite, present the following peaks {111}, {112}, {121}, {004}, {321} and {224} in the XRD spectrum in agreement with ICDD (1975), DĄBROWA *et al.* (2018) and Cerra Florez *et al.* (2021). The peaks identified for the phase B in the XRD spectrum are: {012}, {104}, {110}, {113}, {024}, {116} and {214} correspond to hematite (Fe_2O_3) according to JCPDS No.084-0308 (ICDD, 1975). In C, the peaks {110}, {101} and {200} were identified as the titanium oxide (TiO_2) according to JCPDS No.034-0180 (ICDD, 1975). Furthermore, the XRD spectrum show several peaks {002}, {-112}, {022}, {220} and {112} labelled as D phase and identified as molybdenum oxide (MoO_3) according to JCPDS No.080-0347 (ICDD, 1975), and also as reported by Zhao *et al.* (2020). In E, it is possible to see two different peaks - {111} and {200}- that correspond to the austenitic (γ-) phase (CERRA FLOREZ *et al.*, 2021; CONDE *et al.*, 2019), which is rich in Ni, Fe and Co in agreement with Klein, Sharon and Yaniv (1981), Klein, Yaniv and Sharon (1981; 1983), Rezek, Klein and Yahalom (1997) and Cerra

Florez *et al*. (2021). The γ-phase is formed during the oxidation process, when iron (Fe), cobalt (Co), molybdenum (Mo) and titanium (Ti) diffuses through the layer, leaving the maraging alloy surface with a high nickel content.

The phase composition obtained through XRD spectra and present in the different oxide layers produced on maraging 300 and 350 alloys under different atmospheres are summarized in Table 10. The values of the phase's quantification performed on the oxides shows similar amount of each compound for all conditions. The oxides produced on the maraging 350 alloy under the different investigated conditions present the lowest proportion of spinel, however, a greater amount of MoO_3 and TiO_2 is evident. This phenomenon may be related to the greater amount of Co and Ti in the chemical composition of the maraging 350 alloy (see Table 3). This effect is in agreement with the data reported in Magnée *et al.* (1974), Lima Filho, Barrosa and Gomes de Abreu (2017), Cerra Florez *et al*. (2021), Vasudevan, Kim, and Wayman (1990) and Sha, Cerezo and Smith (1993), and it is attributed that the thermal treatment helps to increase the number of intermetallic precipitates rich in Mo and Ti along with the oxide layer. The amount of hematite formed in all oxides is relatively similar, which indicates that, although two different atmospheres were used in the first stages, in both processes the kinetic and thermodynamic conditions are favorable to produce the formation of this phase.

Figure 22 – X-ray diffraction spectra of the different oxides produced under different atmospheres for each maraging alloy

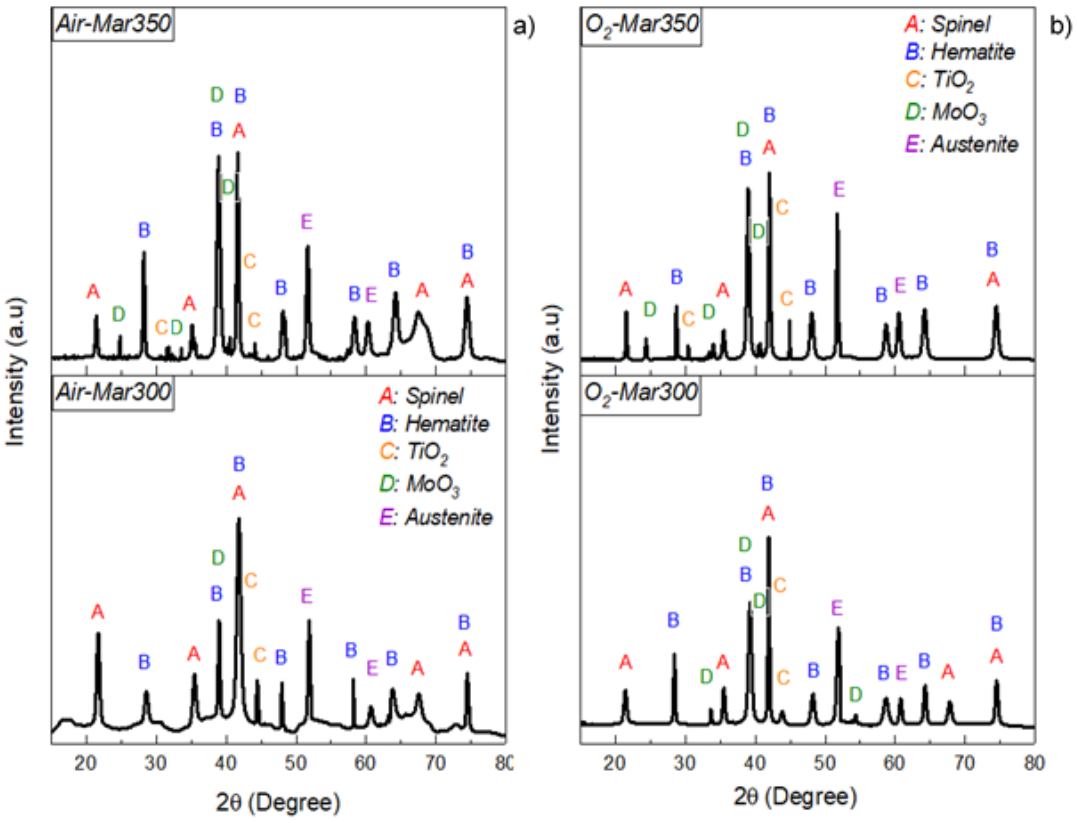

Source: Author (2021).

Table 10 – Vol. % content for each constitutive phase present in the oxide layer produced in both maraging alloys

Atmosphere	Steel	Vol. % Spinel	Vol. % Hematite	Vol. % MoO_3	Vol. % TiO_2
Air/Steam/N_2	M300	45	47	5	3
	M350	44	42	9	5
O_2/Steam/N_2	M300	43	51	5	1
	M350	42	45	9	4

Source: Author (2021).

Figures 23 and 24 exhibit the optical (left-hand side) and laser scanning confocal microscope (LSCM) (right-hand side) micrographs of the oxide layer for the air/steam/N_2 and O_2/steam/N_2 atmosphere for each investigated system, respectively. As it is evident, all the different layers present the same type of heterogeneities, such as ridges, valleys, cracks and peeling. These defects were created due to the difference in volume, thermal expansion coefficient and density between the different constitutive phases that form the oxide layer. As well as external factors such as condensation of vapor on the surface, which can help the creation of these defects.

Figure 25 shows the 3D topography image (650 × 470 μm^2) obtained by interferometry of each investigated specimen. In the images, it's possible to see a heterogeneous surface with several nodules, high peaks and deep valleys along the surface that suggests a non-uniform growing process. The main roughness parameters (S_a and S_z) are described in Table 11. As it is evident in these images, the bands that appear in the interferometric images are related to the ground/polishing patterns induced prior to the oxidation process. Furthermore, the Sa is similar for all the different investigated samples, although the surface of the oxide produced in the maraging 300 alloy under Air/Steam/N_2 atmospheres presents greater variations between the highest peak and the deepest valley. The small differences found between the roughness of the samples do not indicate any relationship with the chemical composition of the steels and perhaps they are more reactive with the heat treatment itself.

Figure 23 – Optical (a, c, e) and laser scanning confocal microscope – LSCM (b, d, f) micrographs of several defects heterogeneously distributed on the oxide layer produced under air/steam/N_2 atmosphere for each maraging alloy

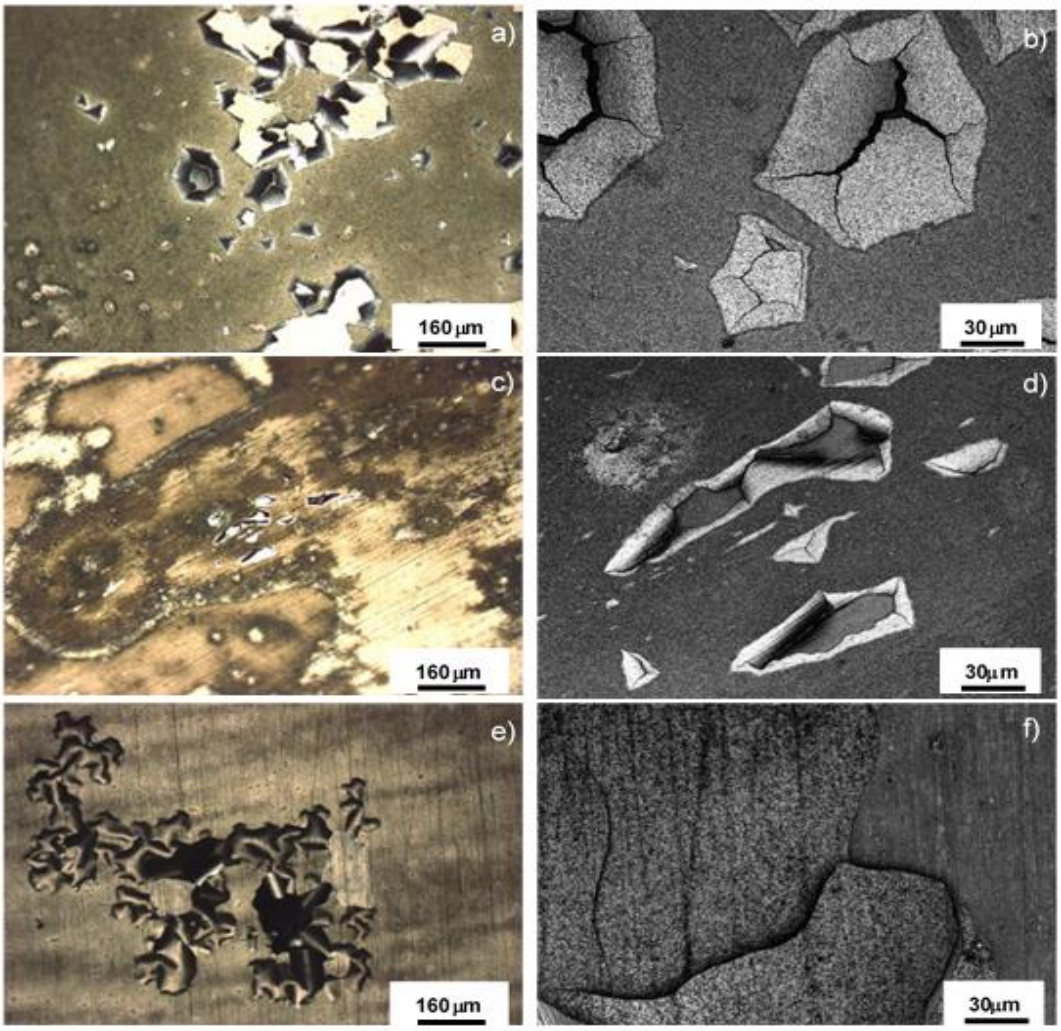

Source: Author (2021).

Figure 24 – Optical (a, c, e) and laser scanning confocal microscope – LSCM (b, d, f) micrographs of several defects heterogeneously distributed on the oxide layer produced under O_2/steam/N_2 atmosphere for each maraging alloy.

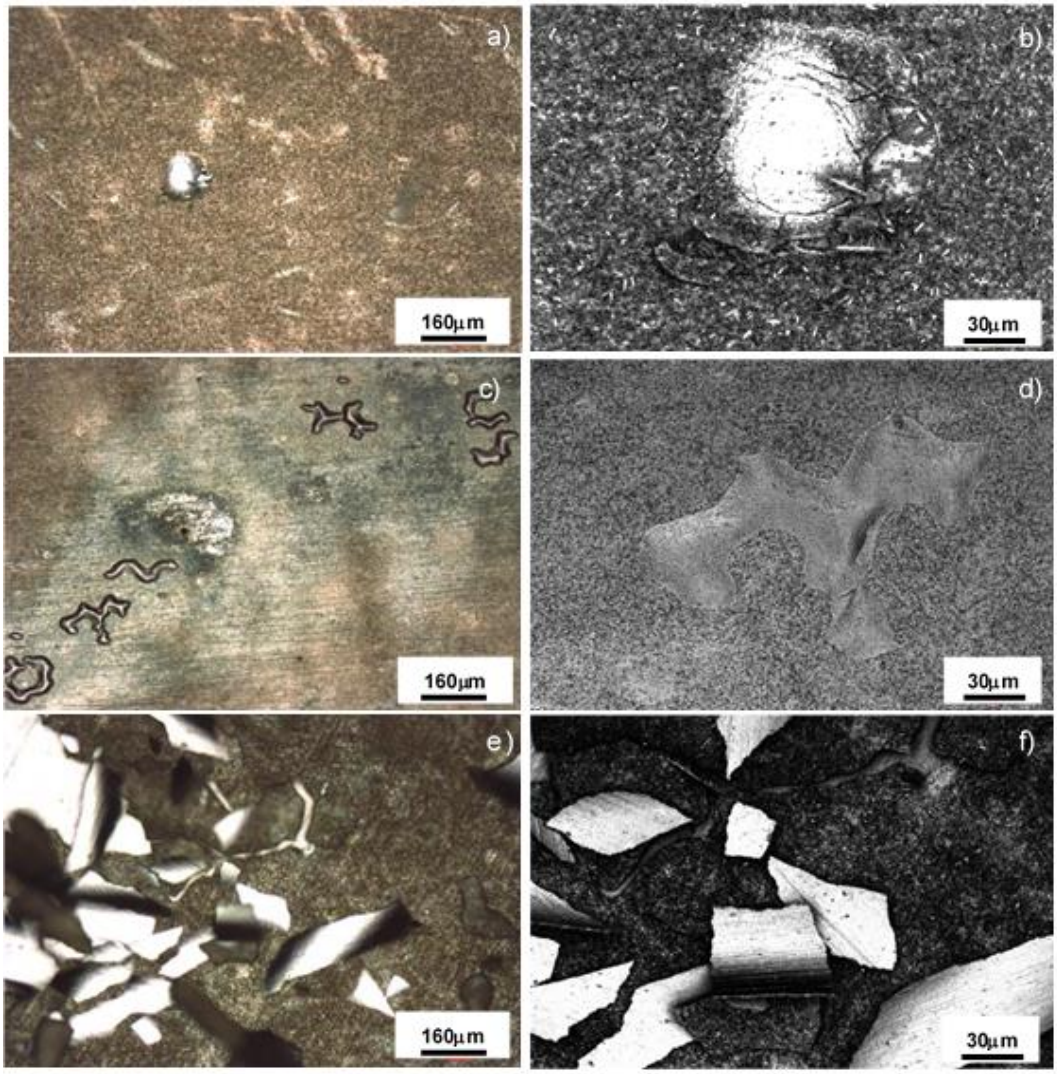

Source: Author (2021).

Figure 25 – Interferometry 3D topography of the oxide surface produced in each maraging alloy (a)-(b) maraging 300 alloy and (c)-(d) maraging 350 alloy

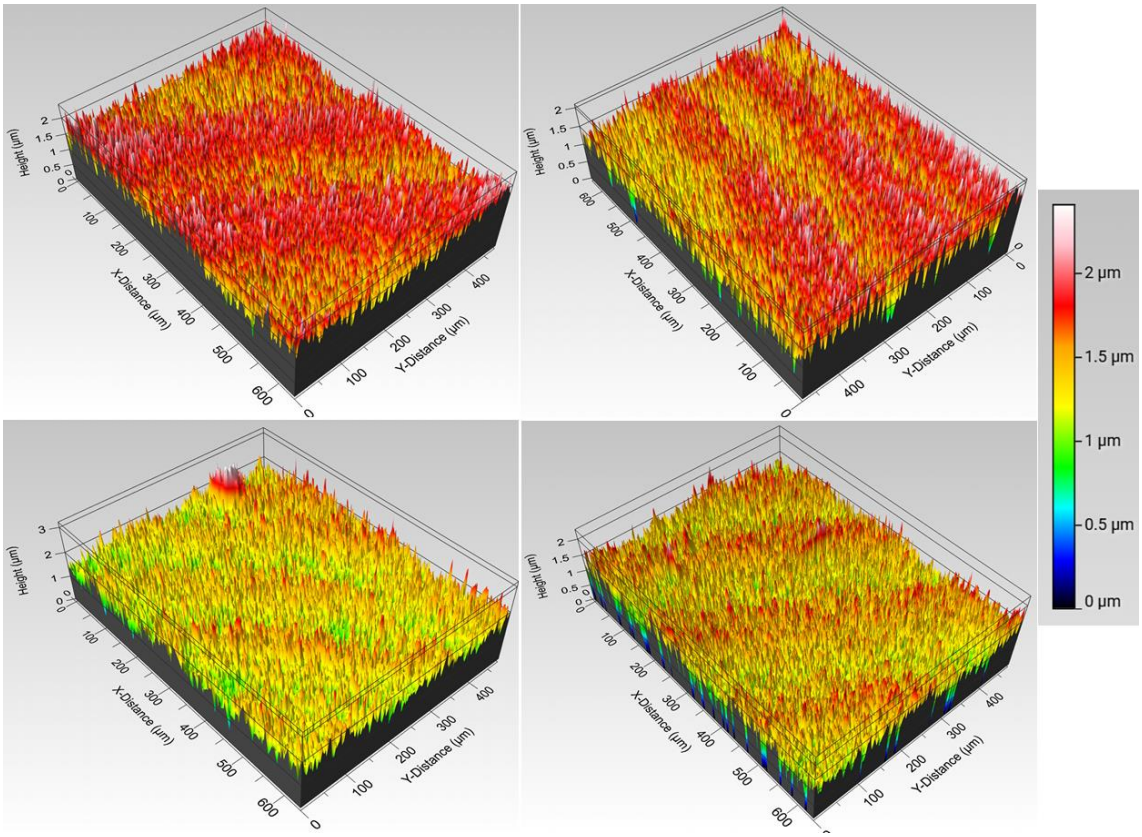

Source: Author (2021).

Table 11 – Roughness parameters (in µm) for each investigated system according to ISO 25178

	Air/Steam/N_2 - Mar300	**Air/Steam/N_2 - Mar350**	**O_2/Steam/N_2 - Mar300**	**O_2/Steam/N_2 - Mar350**
Arithmetic mean height (S_a)	0.18	0.18	0.22	0.17
Maximum Height (S_z)	2.41	2.09	3.21	2.29
Maximum Peak Height (S_p)	0.85	0.83	1.66	1.10
Maximum Pit Height (S_v)	1.56	1.26	1.55	1.19
Root Mean Square Height (S_q)	0.22	0.23	0.28	0.22

Source: Author (2021).

Figure 26 shows scanning electron microscopy (SEM) micrographs of the oxide layer produced under Air/Steam/N_2 atmosphere on maraging 300 alloy. In Figure 26a the oxide layer looks homogeneous, with high content of defects, like porosity, nodules (Figures 26b and 26c). Table 12 summarizes the chemical composition obtained by energy-dispersive X-ray spectroscopy (EDS) near the nodule as depicted in Figure 26c. These measurements show that there are variations in its chemical composition, therefore, the typical area of the oxide (with greater porosity) presents a high Co content (point B in Figure 26c), while in the upper region of the nodule (point A in Figure 26c)

presents a high Ni and Mo content. Also, it is necessary to highlight that in the different regions the Fe content is homogeneous, while the content of Ti changes considerably – points A and B the Ti content is homogeneous while at point C is deficient of this element. It is essential to indicate that in this research, the EDS oxygen value was only taken into account for comparative purposes.

Figure 26 – Scanning electron microscopy (SEM) micrographs of the oxide layer on maraging 300 alloy growth under Air/steam/N_2 atmospheres

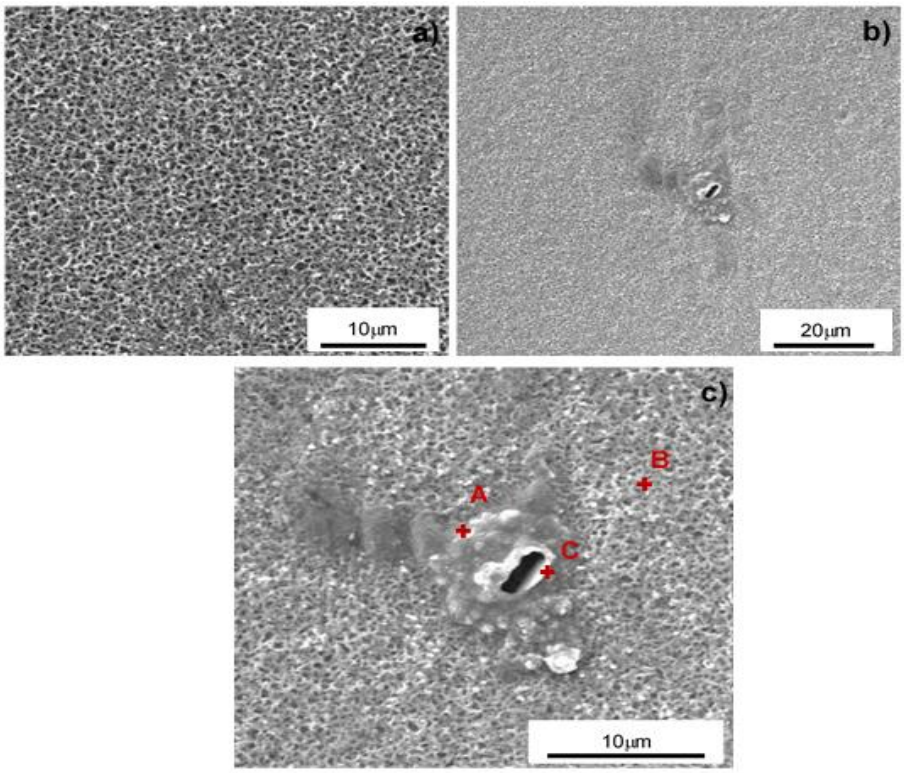

Source: Author (2021).

Table 12 – Summary of the chemical composition determined by energy-dispersive X-ray spectroscopy (EDS) measurements taken at different locations (see Figure 26c)

EDS quantitative analysis from points A, B and C (wt.%)				
Elem. Number	Elem. Symbol	**Point A**	**Point B**	**Point C**
26	*Fe*	57.52	58.54	63.44
8	*O*	33.98	34.26	29.74
27	*Co*	4.77	6.25	4.33
28	*Ni*	2.88	0.53	2.00
42	*Mo*	0.69	0.32	0.48
22	*Ti*	0.15	0.10	-

Source: Author (2021).

Figure 27 exhibits the scanning electron microscopy (SEM) micrographs of the different heterogeneities dispersed in the oxide layer for the maraging 350 alloy growth under Air/Steam/N_2 atmosphere, such as protuberances, cracks, ridges and oxide decohesion. Four different chemical measurements were done by energy-dispersive X-ray spectroscopy (EDS) (see Figure 27c) and summarized in Table 13. On the other hand, Figure 28 shows the SEM micrographs for the oxide layer growth under O_2/Steam/N_2 atmosphere on maraging 300 alloy. These micrographs show similar kinds of defects (such as cracks and ridges). The chemical composition near an oxide defect is summarized in Table 14. The quantification on the tables 13 and 14 confirms the existence of an element's concentration profile in the different oxide layer, the inner base is richer in elements such as nickel, titanium, cobalt and molybdenum, and in the upper part the iron is abundant.

Figure 27 – Scanning electron microscopy (SEM) micrographs of the oxide layer growth under air/steam/N_2 on maraging 350 alloy

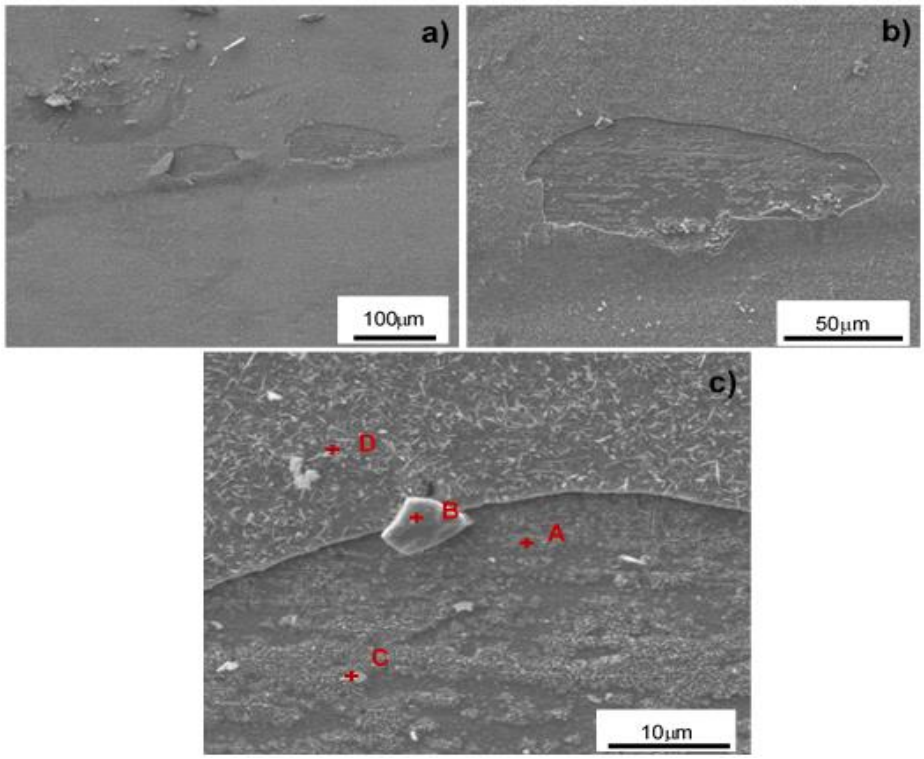

Source: Author (2021).

Table 13 – Summary of the chemical composition determined by energy-dispersive X-ray spectroscopy (EDS) measurements taken at the different locations indicated in Figure 27c

EDS quantitative analysis from points A, B, C and D (wt. %)					
Elem. Number	Elem. Symbol	**Point A**	**Point B**	**Point C**	**Point D**
26	*Fe*	38.68	48.51	53.37	67.04
8	*O*	19.94	22.05	30.32	29.44
27	*Co*	11.35	7.21	4.77	2.16
28	*Ni*	17.60	9.47	4.08	0.54
42	*Mo*	10.32	10.52	6.24	0.67
22	*Ti*	2.10	2.24	1.22	0.14

Source: Author (2021).

Figure 28 – Scanning electron microscopy (SEM) micrographs of the oxide layer growth under O_2/steam/N_2 atmosphere on maraging 300 alloy

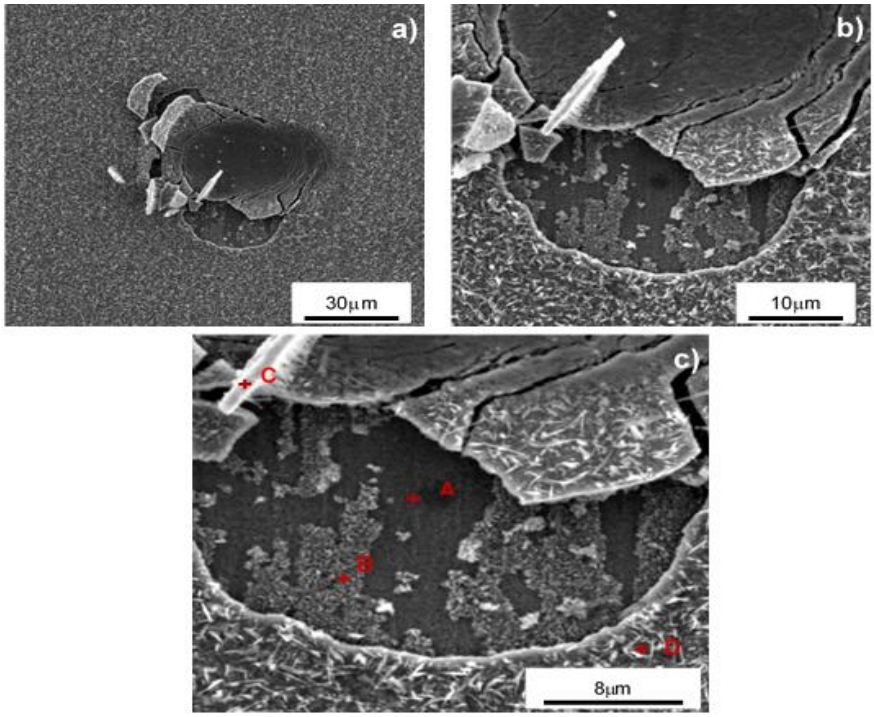

Source: Author (2021).

Table 14 – Summary of the chemical composition determined by energy-dispersive X-ray spectroscopy (EDS) measurements taken at the different locations indicated in Figure 28c

EDS quantitative analysis from points A, B, C and D (wt. %)					
Elem. Number	Elem. Symbol	**Point A**	**Point B**	**Point C**	**Point D**
26	*Fe*	46.16	55.05	63.36	66.93
8	*O*	20.70	33.99	36.64	28.89
27	*Co*	8.29	4.07	-	2.72
28	*Ni*	13.34	2.37	-	0.74
42	*Mo*	10.44	4.11	-	0.67
22	*Ti*	1.07	0.41	-	0.06

Source: Author (2021).

The surface of the oxide layer produced under O_2/Steam/N_2 atmospheres on maraging 350 alloy are shown in Figure 29, where some heterogeneities like protuberances are clearly visible (see Figure 29a and 29b). Scanning electron microscopy (SEM) magnification of this defect is appreciated in Figure 29c. Also, in this image, two different punctual energy-dispersive X-ray spectroscopy (EDS) analysis was also carried out on and also at the vicinity of the defect to determine the chemical composition (see Table 15). The chemical composition and morphological differences indicate the existence of different phases or compounds dispersed in the surface of the oxide in fair agreement with the XRD spectra presented in Figure 22.

Figure 29 – Scanning electron microscopy (SEM) micrographs of the oxide layer growth under O_2/steam/N_2 atmosphere on maraging 350 alloy

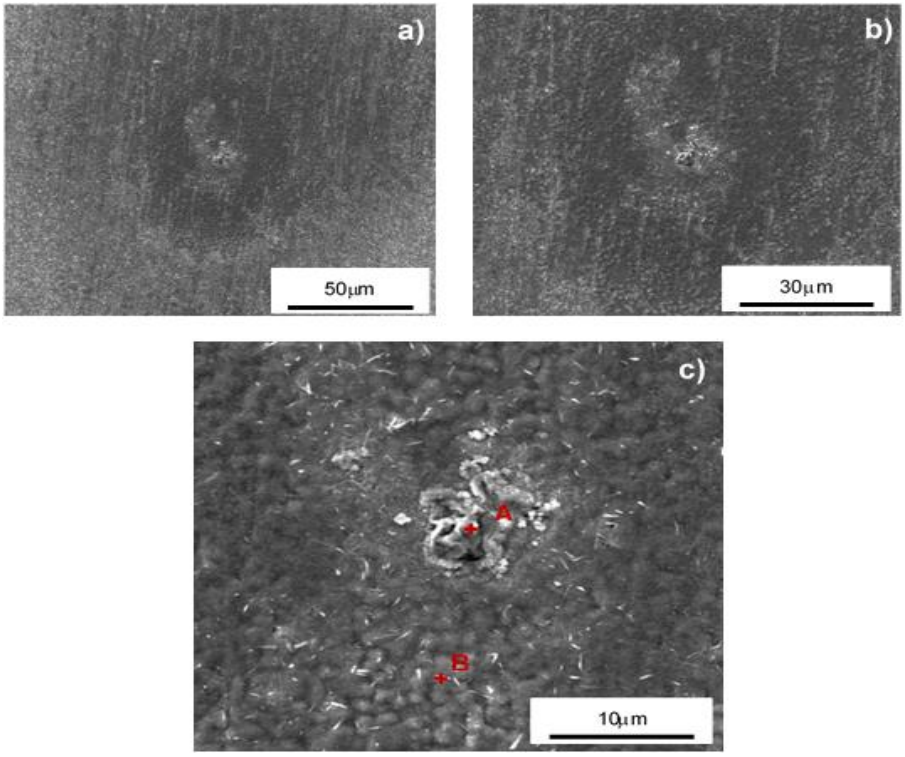

Source: Author (2021).

Table 15 – Summary of the chemical composition determined by energy-dispersive X-ray spectroscopy (EDS) measurements taken at the different locations indicated in Figure 29c

EDS quantitative analysis from points A and B (wt. %)			
Elem. Number	Elem. Symbol	**Point A**	**Point B**
26	*Fe*	41.72	56.15
8	*O*	38.00	34.05
27	*Co*	5.47	5.27
28	*Ni*	3.04	2.16
42	*Mo*	11.53	1.99
22	*Ti*	0.26	0.38

Source: Author (2021).

Scanning electron microscopy (SEM) micrographs in Figure 30 (a,c,e,g) shows a line scan (white dash line) energy-dispersive X-ray spectroscopy (EDS) analysis (Figure 30 (b,d,f,h)) crossing the main defects present in the oxide layer of each maraging alloys investigated here. The chemical profiles through the defect present on the oxide layer by using air/steam/N_2 atmospheres on maraging 300 alloys, it is possible to see a rectangular shape with straight edges. This inclusion is rich in Ti that corresponds to a specific defect of the material. It is well investigated (CAPURRO; CICUTTI, 2018; CERRA FLOREZ *et al.*, 2021; SILVA *et al.*, 2008) that in these alloys with an appreciable Ti and N content, it is possible the formation of titanium nitrides (TiN) during the solidification process. On the other hand, for the oxide layer present in maraging 350 alloys under air/steam/N_2 atmospheres, the chemical composition map shows the composition differences between the inner layer (rich in Ni, Mo, Co and Ti) and the outer layer is rich in Fe. This differential in composition is in agreement with the finding reported in Klein, Sharon and Yaniv (1981), Klein, Yaniv and Sharon (1981; 1983) and Cerra Florez *et al.* (2021). In Figure 30e-f and 30g-h are shown the surface oxide layer growth under O_2/steam/N_2 atmospheres on maraging 300 and 350 alloys respectively. Two types of holes are clearly visible. The hole present on maraging 300 alloy presents an increase of the Ni, Co, Ti and Mo content. This phenomenon can be attributed to an enrichment area of intermetallic compounds like Ni_3Ti, Ni_3Mo, Fe_3Ti, and Fe_3Mo that precipitate during the aging treatment of maraging steels in concordance with Magnée *et al.* (1974), Petty (1970), Rack and Kalish (1971), Cerra Florez (2021), Rodrigues, Bernardi and Otubo (2014) and Moshka *et al.* (2015). It is worthily to mention that these intermetallic phases are very stable and do not form oxides, breaking the homogeneity of the oxidized layer. On the other hand, the oxide layer growth on maraging 350 alloy

shows a hole with an increase in the Mo and Ti content. This can be associated with two different phenomena: (1) the presence of TiN and (2) the presence of the different intermetallic compounds (Ni_3Ti, Ni_3Mo, Fe_3Ti, and Fe_3Mo) that do not form oxides. Comparing the microstructural defects present in the oxide layer as well as the chemical composition determined by EDS, both maraging alloys present the same typology of defects and the chemical composition are more or less similar.

Figure 30 – Scanning electron microscopy (SEM) and linear energy-dispersive X-ray spectroscopy (EDS) spectrum of the oxide formed on grade 300 and 350 maraging steel in each condition

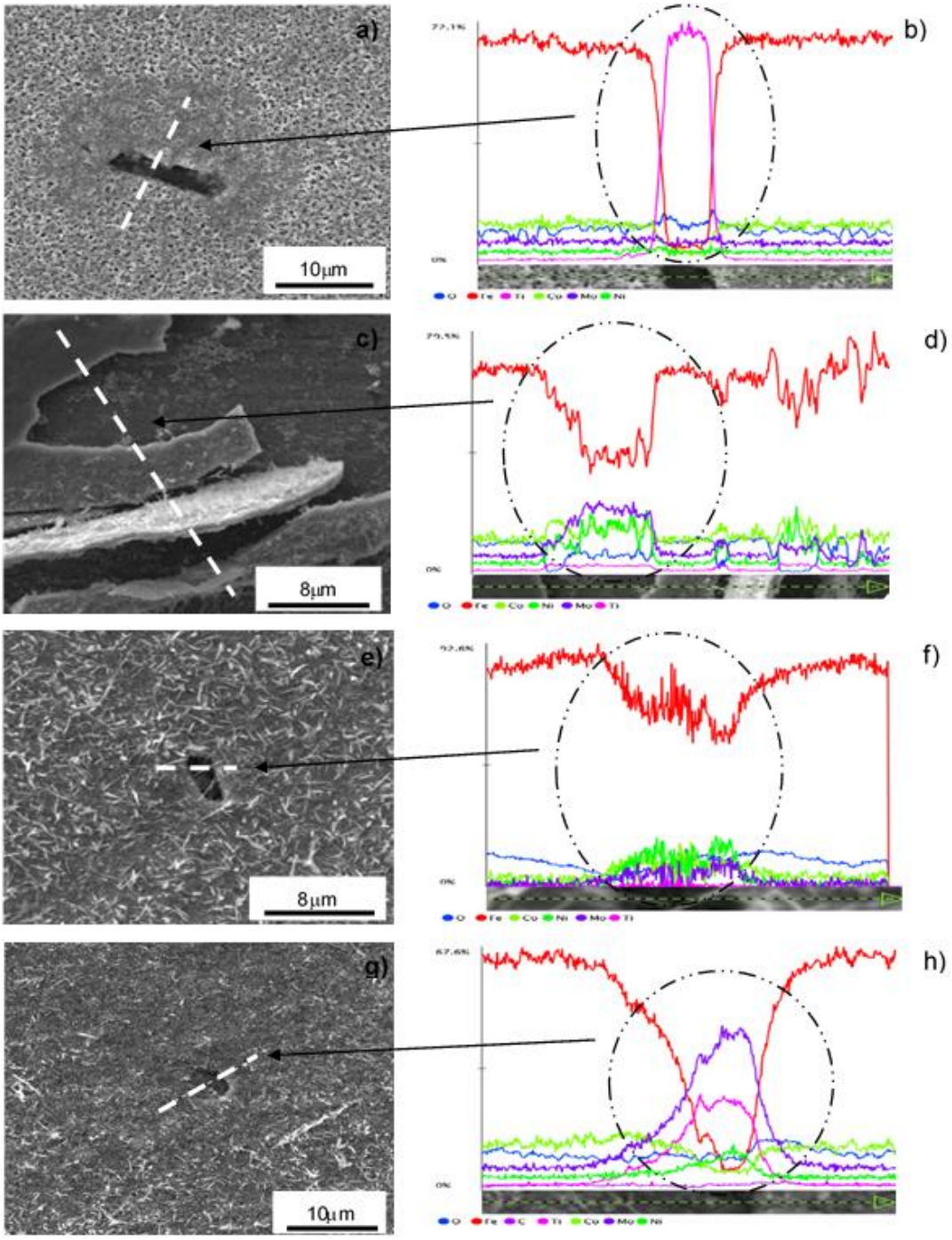

Source: Author (2021).

For the identification spinel's types formed on the samples, Raman spectroscopy technique was used. Figures 31a and 31b show the Raman spectrum obtained from the oxide layer growth under Air/Steam/N_2 and O_2/Steam/N_2 atmospheres on both alloys, respectively. It is possible to find the same species in all the spectrums.

Three spinel's were found, iron ferrite (Fe_3O_4) labeled as A, with the bands located at 302, 460, 616, 660 and 690 cm^{-1} (KUMAR *et al.*, 2014; ROBINSON *et al.*, 2019), Nickel ferrite ($NiFe_2O_4$) identified as B, with the bands at 195, 316, 470 and 679 cm^{-1} (GAO *et al.*, 2020; WANG *et al.*, 2015), and Cobalt ferrite ($CoFe_2O_4$) labeled as C and located in the bands 300, 465, 615, and 679 cm^{-1} (CERRA FLOREZ *et al.*, 2021; DE LA FIGUERA *et al.*, 2015; GAO *et al.*, 2020; ROUTRAY; SAHA; BEHERA, 2020; WANG *et al.*, 2015). It was also found hematite (α-Fe_2O_3) with the bands located at 227, 246, 293, 412, 500, 611 and 1321 cm^{-1} (CERRA FLOREZ *et al.*, 2021; DE FARIA; LOPES, 2007; GUO *et al.*, 2020) labeled as D, and the molybdenum oxide (MoO_3) was also identified (E) by the bands at 280, 663, 816 and 901 cm^{-1} (ALMODÓVAR *et al.*, 2021; FARZI-KAHKESH; FATTAH; BAGHER RAHMANI, 2021; REED *et al.*, 2019; YANG *et al.*, 2019). With this result, the existence of all expected spinel's was confirmed.

Figure 31 – Raman spectra of the oxide layer growth under different atmospheres on maraging 300 and 350 alloy

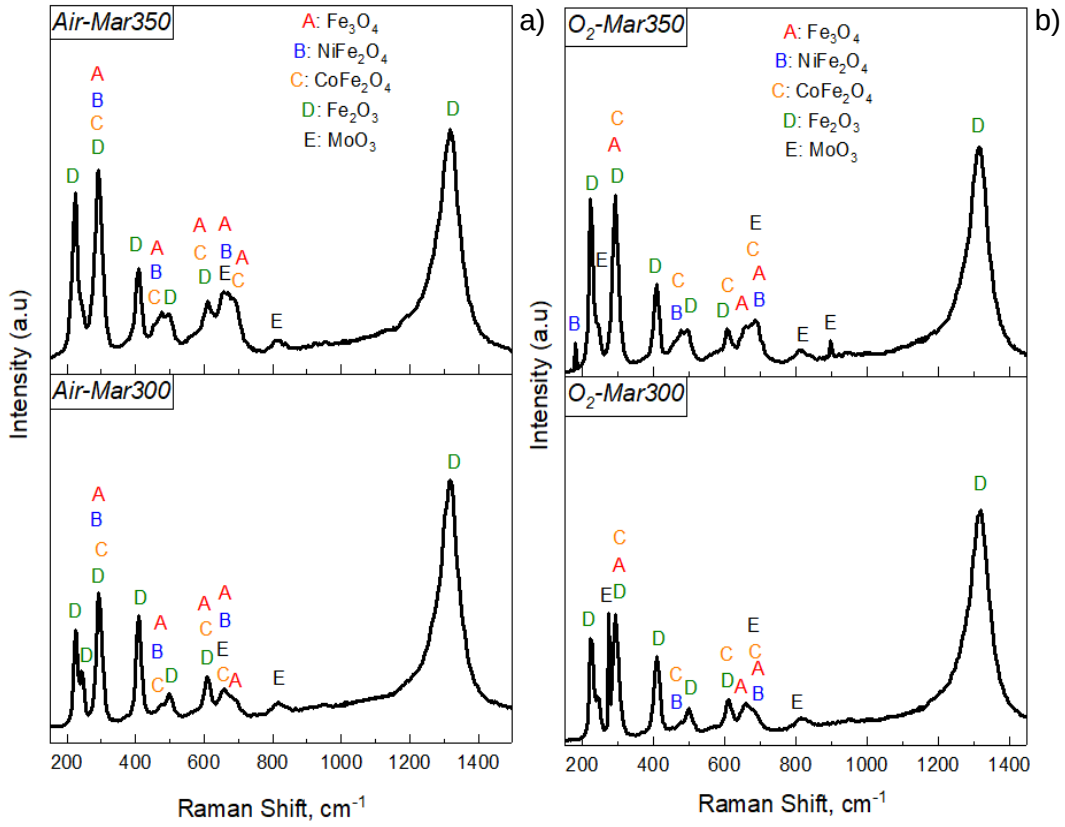

Source: Author (2021).

The examination and the determination of the oxide layer thickness are essential to reach a proper understanding of the oxidation process under the different atmospheres used on the maraging alloys. To observe and determine the thickness of each oxide layer, cross-sections were done using the focused ion beam (FIB) technique. Figure 32 presents two field emission scanning electron microscopy (FE-SEM) micrographs performed on each oxide layer, one general and one magnified to observe the oxide in more detail and measure the thickness of the layer. The oxides produced in the atmosphere with synthetic air in maraging steel 300 correspond to Figures 32a and 32b, and those formed in maraging steel 350 are in Figures 32c and 32d. On the other hand, the oxides produced in the atmosphere with O_2 in maraging 300 steel are in Figures 32e and 32f, and those formed in maraging 350 steel correspond to Figures 32g and 32h.

Generally speaking, in all oxides, non-homogeneous thicknesses are observed and with several defects in the different layers of the films, such as porosity, small holes and roughness. Darker areas in the internal parts of the oxides are due to the junction of pores and the consequent formation of larger defects such as holes and even cracks, the generation of these phenomena is related to differences in the expansion coefficient between the different constitutive phases, as well as being related to chemical heterogeneities along with the oxide layer. In all the micrographs it is possible to observe the small fine-grained microstructure with a different shade just below the metal–oxide interface, it is an austenitic-rich phase in Ni and Co formed due to the oxidation process (CERRA FLOREZ *et al.*, 2021; KLEIN; YANIV; SHARON, 1981; 1983; KLEIN; SHARON; YANIV, 1981; REZEK; KLEIN; YAHALOM, 1997).

The oxides showed a dendritic-type metal-oxide interface, which was more evident in the micrographs of the oxides produced in maraging 300 steel. This phenomenon may be due to the oxidation process in which metal ions leave the steel and travel through the oxide formed to the outermost layers (CERRA FLOREZ *et al.*, 2021; KLEIN; YANIV; SHARON, 1981; 1983; MAGNÉE *et al.*, 1974). Table 16 shows the values of the average thickness measured for each oxide. The highest values were found in the oxide produced in maraging 300 steels (where the oxidation dendrites are more visible), which could indicate a greater susceptibility to oxidation of this steel, this makes sense due to the greater amount of alloying elements that would bring some greater degree of stability to maraging steel 350 (CERRA FLOREZ *et al.*, 2021; LIMA FILHO;

BARROSA; GOMES DE ABREU, 2017; MAGNÉE *et al.*, 1974; SHA; CEREZO; SMITH, 1993; VASUDEVAN; KIM; WAYMAN, 1990).

Table 16 – Thickness average measured from the field emission scanning electron microscopy (FE-SEM) micrographs for the oxide produced by each condition

Maraging alloy	Atmosphere	Thickness Average (μm)
300	Air	2.0
	O_2	2.4
350	Air	1.6
	O_2	1.3

Source: Author (2021).

Figure 32 – Field emission scanning electron microscopy (FE-SEM) cross-section micrographs though the oxide layer produced using in air synthetic atmosphere on grade 300 (a,b) and 350 maraging steels (c,d) and O_2 atmosphere on grade 300 (e,f) and 350 maraging steels (g,h)

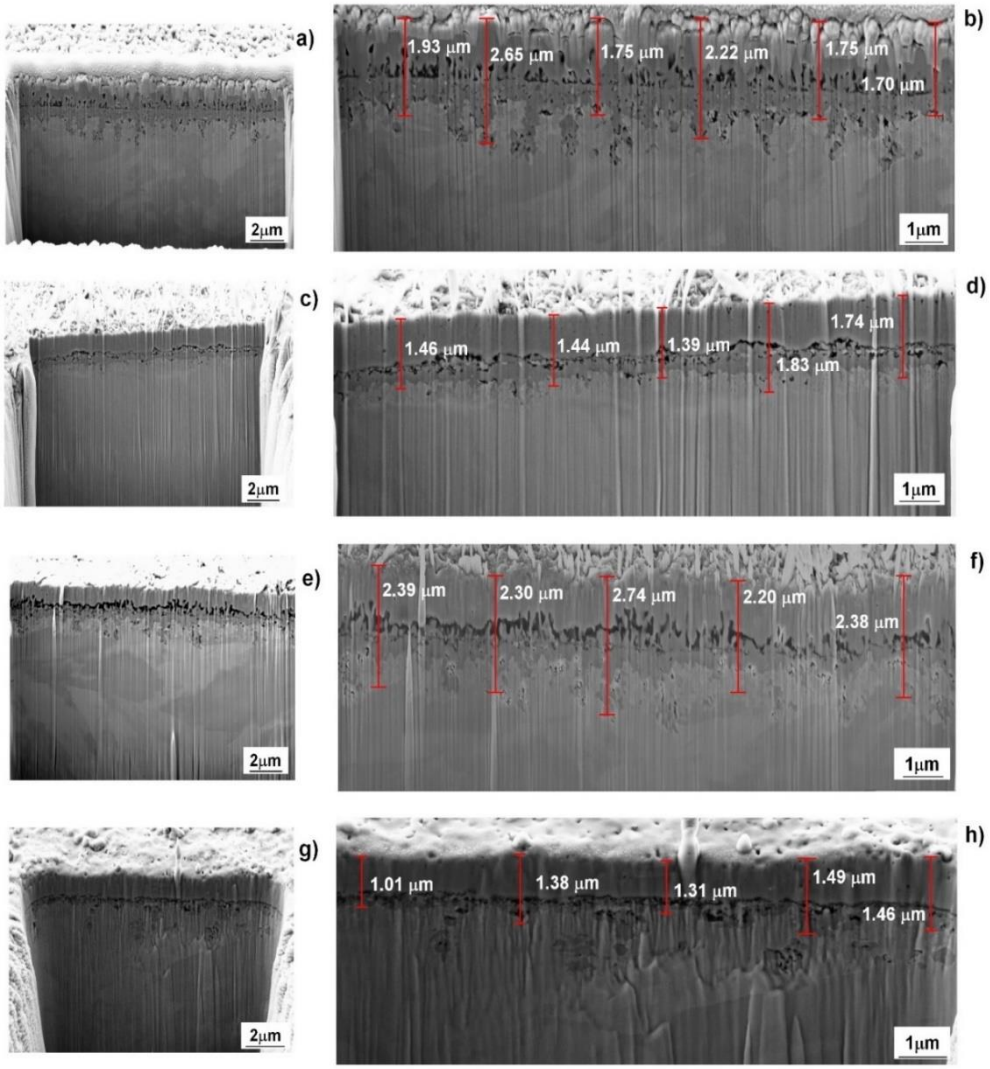

Source: Author (2021).

The results on all oxides showed a heterogeneous layer, with different surface defects and formed by the same constitutive phases. The chemical composition of the oxide layer has variations from the metal/oxide interphase to the external surface, these differences are due the oxidation process of each element in the maraging alloy. Several authors commented about the formation and growth processes, and different points of view have been found. Klein, Sharon and Yaniv (1981), Cerra Florez *et al.* (2021) and Luo and Chenz (2008) mentioned that the formation of the oxide in maraging alloys at temperatures above 300 ºC is explained by three different steps: (1) decomposition of the H_2O or O_2, (2) dissociated oxygen are adsorbed on the steel surface and (3) oxidation reactions between oxygen and metal ions. General oxidation reactions and thermodynamic parameters are presented by Klein, Sharon and Yaniv (1981) and Klein, Yaniv and Sharon (1981) in order to explain the formation of an Iron spinel, as shown in the following reactions:

$$3Fe + 8H_2O \rightarrow Fe_3O_4 + 4H_2O + 4H_2 \qquad \textit{Steam atmosphere} \ (4)$$

$$3Fe + 2O_2 \rightarrow Fe_3O_4 \qquad \textit{Oxygen atmosphere} \ (5)$$

Previous works (GREYLING; KOTZI; VILJOEN, 1990; JEON *et al.*, 2013; KLEIN; SHARON; YANIV, 1981; KLEIN; YANIV; SHARON, 1981; 1983; LUO; SHENZ, 2008; REZEK, KLEIN; YAHALOM, 1997; SUBBARAMAN; DESHMUKH; SANKARANARAYANAN, 2013) mentioned the preferential formation of an iron ferrite (Fe_3O_4) during the maraging oxidation, and also commented that it's possible to find small quantities of Co and Ni as substitutional combinations in the magnetite microstructure, but not forming different compounds. However, in the present work, Ni and Co ferrites ($NiFe_2O_4$ and $CoFe_2O_4$) were found and fully identified within the oxide. The formation of this spinel's are associated to the thermodynamic and kinetic conditions for the transformation of the previous magnetite formed, by the diffusion of Co and Ni in the form of Co^{2+} and Ni^{2+} species from the metallic matrix, these ions end up occupying the octahedral sites on magnetite, replacing the Fe^{2+} ion and displacing it to the outside of the film, were exposed to a higher concentration of oxygen, they are oxidized to Fe^{3+} (BLIEM *et al.*, 2015; CERRA FLOREZ *et al.*, 2021; DĄBROWA *et al.*, 2018; GENUZIO *et al.*, 2016; PARDAVI-HORVATH, 2000; RODRIGUES *et al.*, 2015;

TSUKIMURA; SASAKI; KIMIZUKA, 1997). These ions transform part of the magnetite in the other two spinels.

Due to the thermodynamic and kinetic conditions in temperatures ranged between 375 and 526ºC in oxygen rich atmospheres as the used in the heat treatments, make possible that the outermost layer of magnetite transforms into Hematite ($Fe_3O_4 \rightarrow \alpha\text{-}Fe_2O_3$) (CERRA FLOREZ *et al.*, 2021; HONG *et al.*, 2016; JEON *et al.*, 2013; SUBBARAMAN; DESHMUKH; SANKARANARAYANAN, 2013; ZHANG *et al.*, 2016). The transformation process occurs very fast depending on the chemical composition and the defects in the crystalline network (CERRA FLOREZ, 2021; GENUZIO *et al.*, 2016). According to Genuzio *et al.* (2014; 2016) the hematite grows dendritically and has morphological differences comparing with the magnetite. These morphological differences are like the white elongated protuberances found in the oxides produced on both steels in all conditions.

Mo was found in all the oxide layer, with high quantities in the innermost part of the film. Mo is forming MoO_3 oxide as detected by XRD. It is important to mention that previous works commented that this type of compound was only in the inner parts of the oxide because Fe oxides have greater growth kinetics covering the other compounds, however, the greater amounts of Mo and mainly Co in the composition steel chemistry allowed a greater availability of Mo for oxidation. Co decreases the solubility of Mo in steel which, during the thermal aging treatment, produces fine intermetallic precipitates rich in Mo (CERRA FLOREZ *et al.*, 2021; LIMA FILHO; BARROSA; GOMES DE ABREU, 2017; MAGNÉE *et al.*, 1974; SHA; CEREZO; SMITH, 1993; VASUVEDAN; KIM; WAYMAN, 1990).

TiO_2 is formed in the first stage of the oxidation process (SUBBARAMAN; DESHMUKH; SANKARANARAYANAN, 2013; SURMAN, 1973), but due to its low kinetics, it is covered by the other compounds in the innermost parts of the oxide, which is why it was not detected by Raman spectroscopy (CERRA FLOREZ *et al.*, 2021; SUBBARAMAN; DESHMUKH; SANKARANARAYANAN, 2013; SURMAN, 1973).

Tribological properties in terms of scratch testing lead to determine the adhesive damage, known as the minimum interfacial force between the oxide layer and the metallic substrate alloy and represent as *Pc2* (ASTM, 2015c; CERRA FLOREZ *et al.*, 2021; GHASEMI PARIZI *et al.*, 2020). Figure 33 (left-hand side) exhibits the whole

scratch track made on the oxide produced on the steel and treatment described on each image. The behavior is discerned by comparing the micro-fracture events and damage features in regions close to track edges. Figure 33 (right-hand side) shows top-view Field emission scanning electron microscopy (FE-SEM) images of nanoscratch tracks (corresponding to each oxide described on the side) where some interesting features and damage events are clearly visible (i.e. chevron cracks, decohesion, etc.). On the sides of all grooves, one can observe pile-ups as well as loose material in the form of flakes produced by the flow of plastically deformed material and which is responsible of the serrated shape along the scratch track. Furthermore, the Pc2 directly determined from the FESEM micrographs are summarized in Table 17. From Figure 33 and the data summarized in Table 17, it can be shown that the oxide layers grown on maraging 300 alloy requires a higher force in order to produce the decohesion. On the other hand, the O_2 atmosphere produces an embrittlement of the oxide coating and a chipping effect is clearly visible while the oxide coating growth under air atmosphere does not present these damage mechanisms. Furthermore, as it is evident for maraging 300 alloy treated under air atmosphere, no decohesion is visible along the entire scratch track. A similar trend is observed for maraging 350 alloy. However, for this system, the adhesive load is 96% smaller than for the maraging 300 alloy. The oxide films produced in both maraging alloys using air atmosphere presents good adherence comparing with the result published by Cerra Florez *et al.* (2021) and Ghasemi Parizi *et al.* (2020), and the results of the oxides produced in air atmosphere show the capability for being used for tribological applications under sliding contact tests (CERRA FLOREZ *et al.*, 2021; GHASEMI PARIZI *et al.*, 2020) and as coatings for improve the electrochemical behavior of maraging alloys and in equipment's manufactured for use for processing minerals where it is subjected to wear.

Table 17 – *Pc2* directly determined from the field emission scanning electron microscopy (FE-SEM) micrographs for the oxide produced by each condition

Maraging alloy	Atmosphere	Pc2 (mN)
300	Air	> 100
	O_2	2
350	Air	65
	O_2	5

Source: Author (2021).

Figure 33 – Field emission scanning electron microscopy (FE-SEM) (left) image for the nanoscratch track and (right) magnification of the top-view FE-SEM images of nanoscratch tracks where the first adhesive damage appears

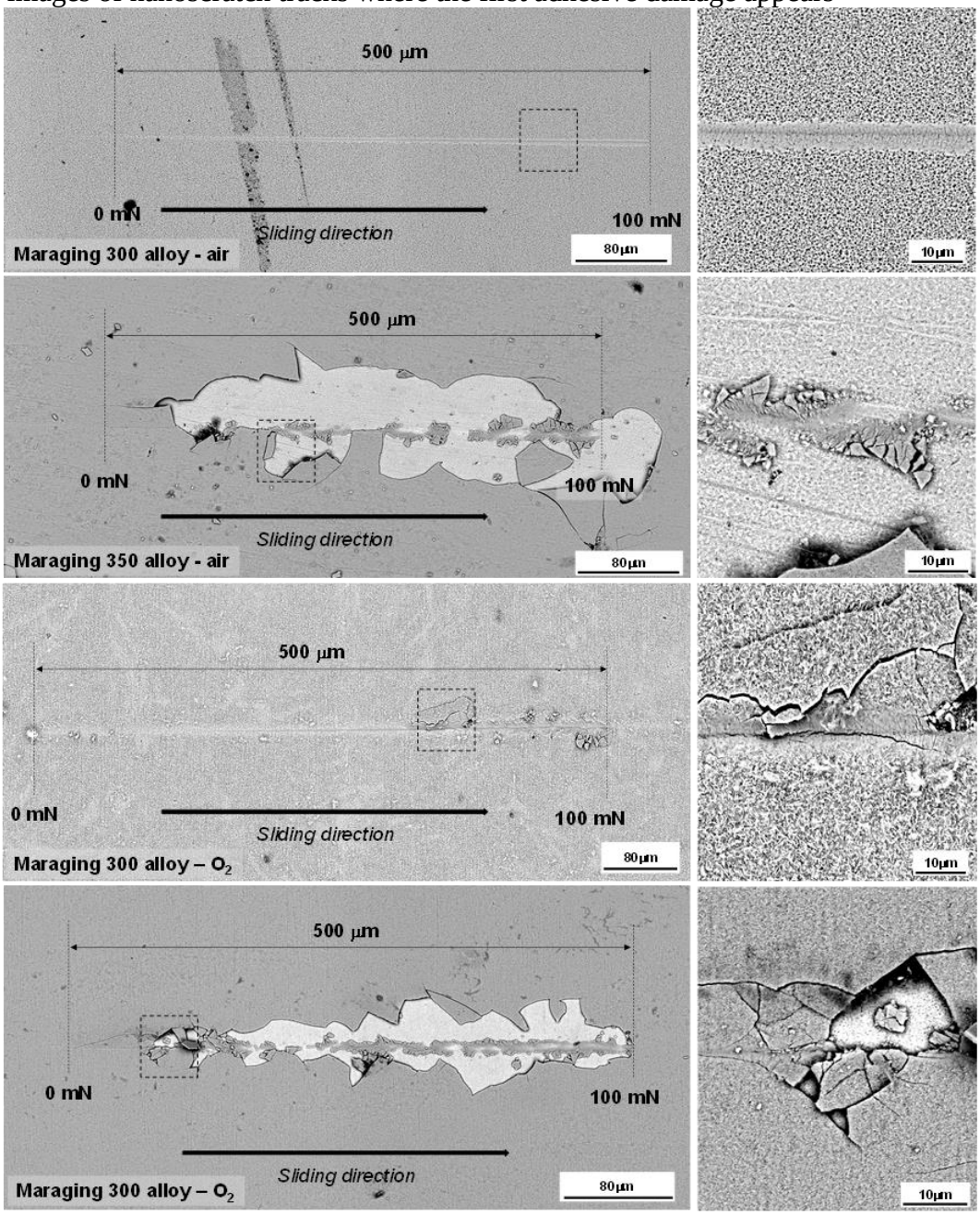

Source: Author (2021).

4.3.3 Conclusions

The oxides produced in both maraging alloys presents heterogeneous oxide layer, with the presence of several defects spread on all the surface, such as holes, cracks and porosity. The differences in terms of roughness of all the samples do not indicate any

relationship with the chemical composition of the different investigated alloys, therefore, it depends on the atmosphere used during the heat treatment itself.

It was possible to confirm the variable chemical composition from the innermost towards the oxide surface. Higher concentrations of alloy elements such Ni, Ti, Mo, and Co are found in the oxide layer/metal interface.

The phases present on the oxide layer grown in both conditions are iron spinel ferrite (Fe_3O_4), nickel spinel ferrite ($NiFe_2O_4$), cobalt spinel ferrite ($CoFe_2O_4$), hematite (α-Fe_2O_3), molybdenum oxide (MoO_3) and titanium oxide (TiO_2). It was found the lowest proportion of spinel on the oxides produced on maraging 350 alloy, may be related to the chemical composition of the steel, during the aging treatment, a higher quantity of the intermetallic precipitates rich in Mo and Ti is produced.

The oxygen availability during the first stages of the heat treatment, makes the kinetic and thermodynamic conditions suitable for the formation and growth of the hematite along with the oxide layer.

FIB cross-sections showed that the oxide films present a heterogeneous coating thickness. The oxides showed a dendritic-type metal-oxide interface, and this phenomenon probably may be related to the oxidation process. The highest thickness values were found in the oxide produced in maraging 300 steels which could indicate a greater susceptibility to oxidation of this steel.

The oxide film produced in both maraging alloys using air atmosphere presents excellent adherence between the oxide layer and the metallic substrate either under O_2 atmosphere. It demonstrates their capability for being used under aggressive conditions, such as, coatings for can improve the electrochemical behavior of maraging alloys and in equipment's manufactured for use in processing minerals where it is subjected to wear.

4.4 Characterization study of an oxide film layer produced under CO_2/steam atmospheres on two different maraging steel grades

4.4.1 Review

Currently, surface treatments lead to inducing a superficial layer of several nanometers up to micrometer, which in some cases can be protective. In this experimental

work, an oxide layer was generated under different atmospheres (CO_2 and steam atmospheres) during the thermal aging treatment of two different maraging grades, 300 and 350. Afterwards, this layer was microstructural and mechanically characterized by advanced characterization techniques at the micro- and submicron length scale to highlight some information related to the generated oxide layer. The results showed that the oxide layer (in both grades) was made up of several compounds like: TiO_2, MoO_3, hematite (α-Fe_2O_3), and $CoFe_2O_4$, this being the majority compound distributed homogeneously throughout the layer. Furthermore, a nickel-rich austenitic phase at the interphase was mainly made-up cobalt ions (Co^{2+}), instead of iron ions (Fe^{2+}), within the spinel lattice.

In this sub-chapter of the research, the microstructure and mechanical properties of the oxide layer process generated under different atmospheres (CO_2, water vapor, and nitrogen) for two different maraging steel grades (300 and 350) are investigated. All this sub-chapter was published in Cerra Florez *et al*. (2021).

4.4.2 Results and Discussion

X-ray diffraction (XRD) diffractograms after the annealing treatment conducted at 840 °C for 1 h for both of the maraging steel grades investigated here are depicted in Figure 34. The peaks {110}, {200}, and {211} correspond to the martensitic (α'-) phase in fair agreement with preliminary works (CONDE *et al*., 2019; VIANA *et al*., 2013).

Figure 34 – X-ray diffraction (XRD) diffractograms for the thermally treated specimens for both maraging steel grades

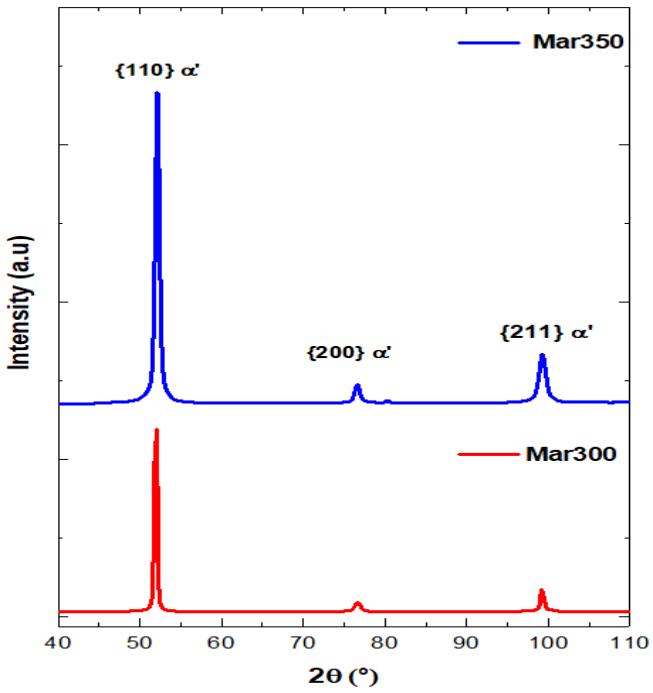

Source: Author (2021).

The oxide layer for both samples was observed by laser scanning confocal microscope (LSCM) covering the entire surface. Both maraging steel grades presented several heterogeneities distributed along the created oxide layer, such as ridges, valleys, cracks, and peeling, as shown in Figure 35. The different defects present in the oxide layer may be related to the expansion coefficient between the phases heterogeneously distributed along the entire oxide layer. Additionally, the present defects could be related with the presence of water molecules condensed on the surface of the oxide layer, which starts to degrade the oxide layer.

The roughness profile for each oxide layer was investigated by optical interferometry, and the 3D topography profiles are shown in Figure 36. From this image it is possible to determine the main roughness parameters, such as arithmetic mean height (Sa) and maximum height (Sz), as well as other parameters that are described and summarized in Table 18. From this observation, it is possible to conclude that the oxide layer does not grow homogeneously due to the presence of several nodules.

Figure 35 – Optical (a,c,e,g,i) and laser scanning confocal microscope (LSCM) (b,d,f,h,j) micrographs of the heterogeneities found on the oxide layer for each maraging steel grade investigated here

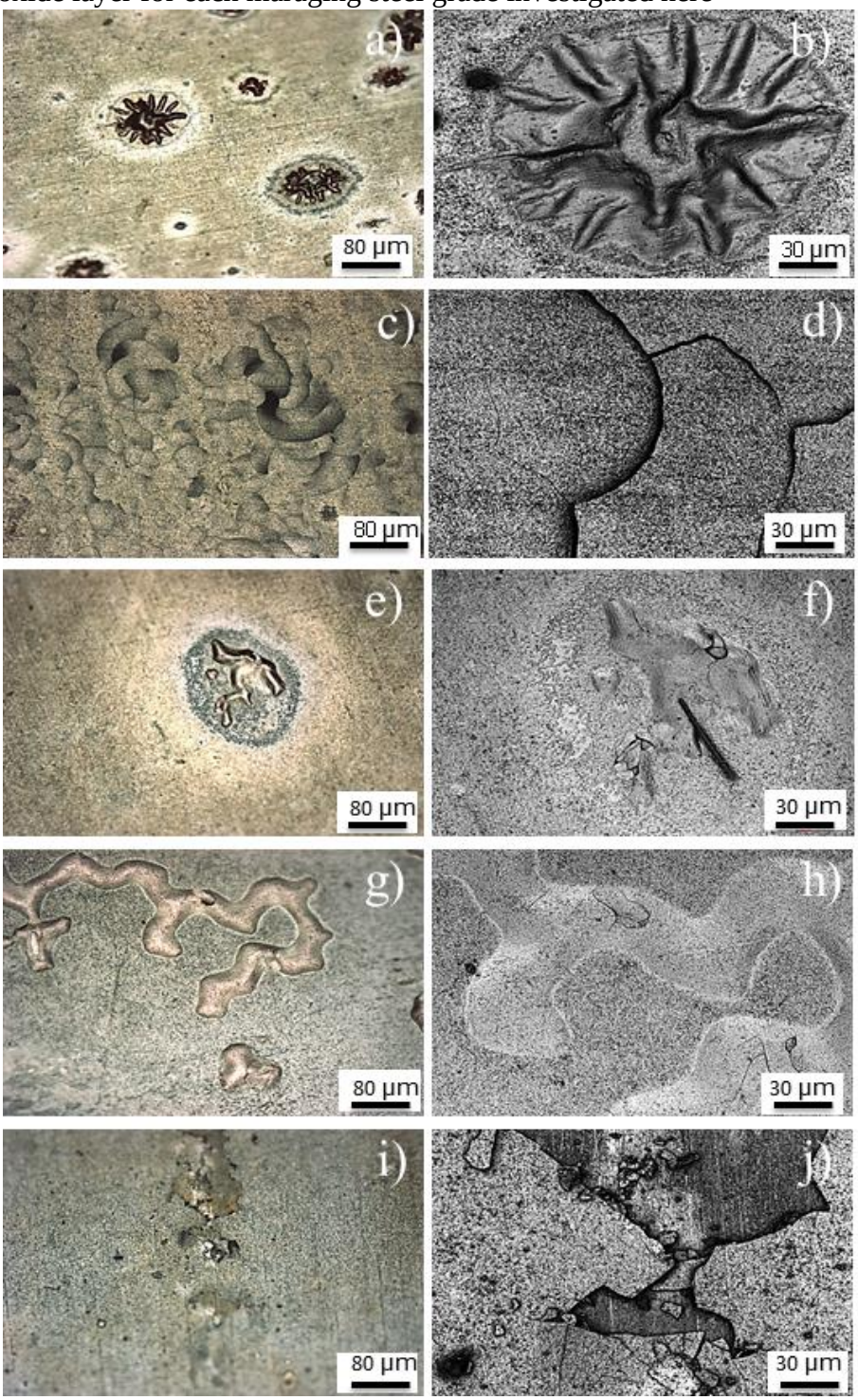

Source: Author (2021).

Figure 36 – Interferometry 3D topography of the oxide surface produced on (a) Mar300 and (b) Mar350 maraging steels

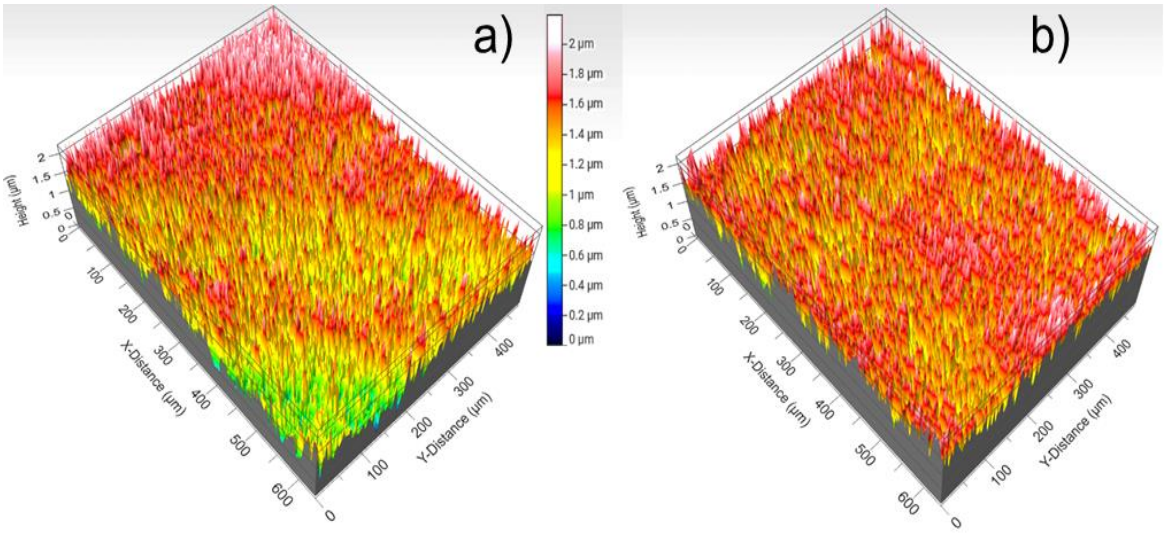

Source: Author (2021).

Table 18 – The main 3D roughness parameters according to ISO 25178

Roughness Parameter	Oxide of the Mar300 (µm)	Oxide of the Mar350 (µm)
Arithmetic mean height (Sa)	0.21	0.20
Maximum Height (Sz)	2.22	2.19
Maximum Peak Height (Sp)	0.90	0.85
Maximum Pit Height (Sv)	1.32	1.34
Root Mean Square Height (Sq)	0.31	0.25

Source: Author (2021).

The oxide layer morphology from each condition and maraging steel grade was observed by scanning electron microscopy (SEM) and is depicted in Figure 37. Figure 37a shows that it is possible to observe a completely covered surface without any superficial defect, and with several heterogeneities, including valleys and cracks (see white circles). On the other hand, in Figure 37b, nodular formations with different layers, sizes, and porosities are observed in more detail. The points highlighted with the letters A and B identify the positions where the chemical analysis by energy dispersive X-ray (EDS) was performed, and are summarized in Table 19, which highlights the chemical composition variation. From this observation, it is possible to observe that the metal base is richer in iron, nickel, titanium, and molybdenum, while the upper part of these nodules is mainly rich in cobalt.

Figure 37 – Scanning electron microscopy (SEM) micrographs of the oxide formed on Mar300 maraging steel, (a) different heterogeneities found on the surface of the oxide and (b) magnification of the nodular formation on the oxide

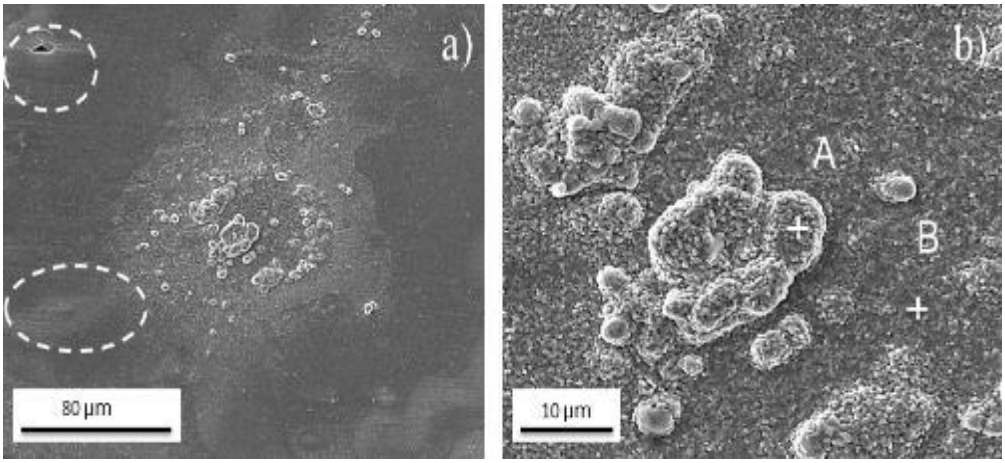

Source: Author (2021).

Table 19 – Energy dispersive X-ray (EDS) spot measurements taken at the different locations shown in the scanning electron microscopy (SEM) micrograph in Figure 37b

EDS Quantitative Analysis from A and B Points (Weight Conc.)			
Element Number	**Element Symbol**	**Point A**	**Point B**
26	Fe	52.57	60.25
8	O	32.46	27.70
27	Co	13.64	9.47
28	Ni	0.69	1.48
42	Mo	0.59	0.95
22	Ti	0.05	0.15

Source: Author (2021).

In Figure 38a, it is possible to observe different heterogeneities dispersed in the different oxide layers for both maraging steel grades, which are identified with white circles, including cracks, ridges, valleys showing the internal oxide, and areas with different straight edges presenting the limits of the chemical composition. On the other hand, Figure 38b shows a high-magnification SEM micrograph of the main defects. Furthermore, in this image, punctual EDS analysis was also carried out on each defect and the results are summarized in Table 20. As is depicted in this Table, there was a difference between points A (located at the homogeneous surface oxide layer) and B (surface valley). The main difference between each point may be associated with the generation of different phases along the oxide layer. On the other hand, point C, located in a nodule at the top of the ridges, presented a composition close to point A, which suggests that the latter is formed above the ridges. At point D, which corresponds to the internal part of the oxide layer, a higher concentration of the main steel elements can be

seen. This information confirms a difference in concentration for the different oxide layers. These differences from a chemical and morphological point of view may indicate the existence of different phases or compounds dispersed along the oxide layer thickness. Finally, the EDS spectra conducted inside a rectangular pore shape (point E) with straight edges presented a chemical composition rich in titanium and nitrogen, which may be related to the formation of titanium nitride (TiN) generated during the solidification process in concordance with results previously reported by Capurro and Cicutti (2018) and Silva *et al.* (2008).

A detailed inspection of the broken oxide fragments and internal oxide layer is shown in Figure 39a. Linear EDS analysis was performed on the white dash line drawn in Figure 39a to compare the internal and external zone of the oxide layer from a chemical point of view (Figure 39b). As is shown, different chemical elements were present in both areas, confirming that the outer part was richer in iron than the inner one.

Figure 38 – Scanning electron microscopy (SEM) micrographs of the oxide formed on Mar300 maraging steel, (a) different heterogeneities found on the surface of the oxide and (b) magnification of the defects found on the oxide

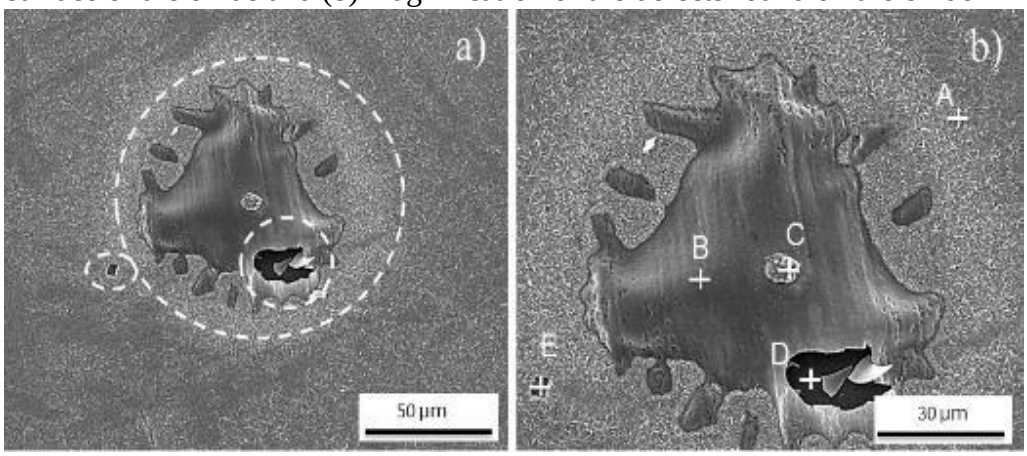

Source: Author (2021).

Table 20 – Energy dispersive X-ray (EDS) spot measurements taken at the different locations shown in the Scanning electron microscopy (SEM) micrograph in Figure 38b

EDS Quantitative Analysis at Points A and B (Weight Conc.)						
Element Number	**Element Symbol**	**Point A**	**Point B**	**Point C**	**Point D**	**Point E**
26	Fe	62.65	60.22	62.50	60.98	3.92
8	O	32.68	38.10	32.34	19.11	31.43
27	Co	3.21	0.64	3.39	9.14	0.63
28	Ni	0.35	0.53	0.90	4.90	-
42	Mo	0.94	0.29	0.71	4.66	-
22	Ti	0.17	0.22	0.16	1.21	44.54
7	N	-	-	-	-	19.48

Source: Author (2021).

Figure 39 – (a) Scanning electron microscopy (SEM) micrograph and (b) linear energy dispersive X-ray (EDS) spectrum made on the white dash line of the Figure 39a of the oxide surface formed on Mar300 maraging steel

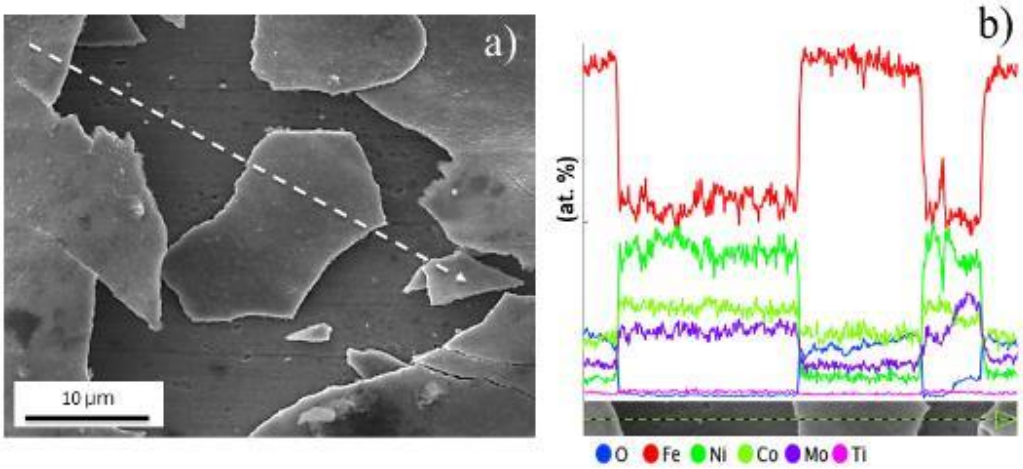

Source: Author (2021).

The heterogeneities observed for the Mar300 maraging steel also were found in the oxide layer in the Mar350 maraging steel. It is necessary to highlight that some imperfections reported previously for the Mar300 maraging steel (see Figure 38) did not exist in the oxides of Mar350 maraging steel, as depicted in Figure 40a, where, in the oxide region, several protuberances and broken areas are clearly visible. Figure 40b shows a magnification of the broken oxide area and the exposed internal oxide. EDS measurements were performed at the indicated points (A: protuberance on the oxide, B: internal part of the oxide, and C: more homogeneous part of the oxide) and the measurements are summarized in Table 21. These results show that the cobalt concentration was close between the internal region and that of the homogeneous oxide layer. Furthermore, the oxide layer presented an increase in the amount of molybdenum and nickel compared to the same area of the oxide formed in the Mar300 maraging steel (see values reported for the point A in Table 20). This difference between both grades may be related to the higher content of cobalt in the chemical composition of steel, which helps the formation of precipitate phases rich in molybdenum during the aging thermal treatment.

Figure 40 – Scanning electron microscopy (SEM) micrographs of the oxide formed on Mar350 maraging steel: (a) different heterogeneities found on the surface of the oxide and (b) magnification of a broken area of the oxide (A: protuberance on the oxide, B: internal part of the oxide, and C: more homogeneous part of the oxide)

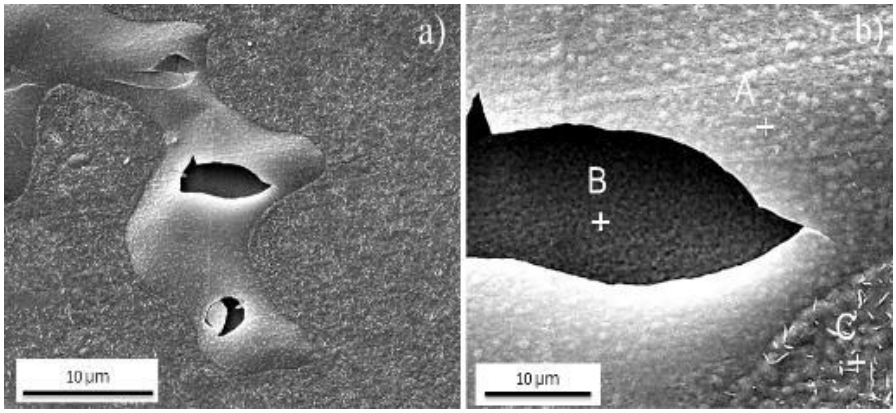

Source: Author (2021).

Table 21 – Energy dispersive X-ray (EDS) spot measurements taken at the different locations shown in the scanning electron microscopy (SEM) micrograph in Figure 40b

EDS Quantitative Analysis from Points A and B (Weight Conc.)				
Elem. Number	**Elem. Symbol**	**Point A**	**Point B**	**Point C**
26	Fe	62.61	55.23	59.43
8	O	34.84	27.97	34.01
27	Co	1.25	4.41	4.24
28	Ni	0.67	5.23	0.79
42	Mo	0.42	5.19	1.30
22	Ti	0.21	1.98	0.23

Source: Author (2021).

Other defects that were heterogeneously distributed along the oxide layer for both grades were the protuberances, as shown in Figure 41a,c. The images suggest that these protuberances were formed by different phases. A high magnification of these defects is shown in Figure 41b,d, and the interphase between this defect and the oxide layer is delimited by white dotted lines.

Figure 41 – Scanning electron microscopy (SEM) micrographs of the oxide formed on Mar350 maraging steel: (a,c) different heterogeneities found on the surface of the oxide and (b,d) magnification of the protuberances found on the oxide

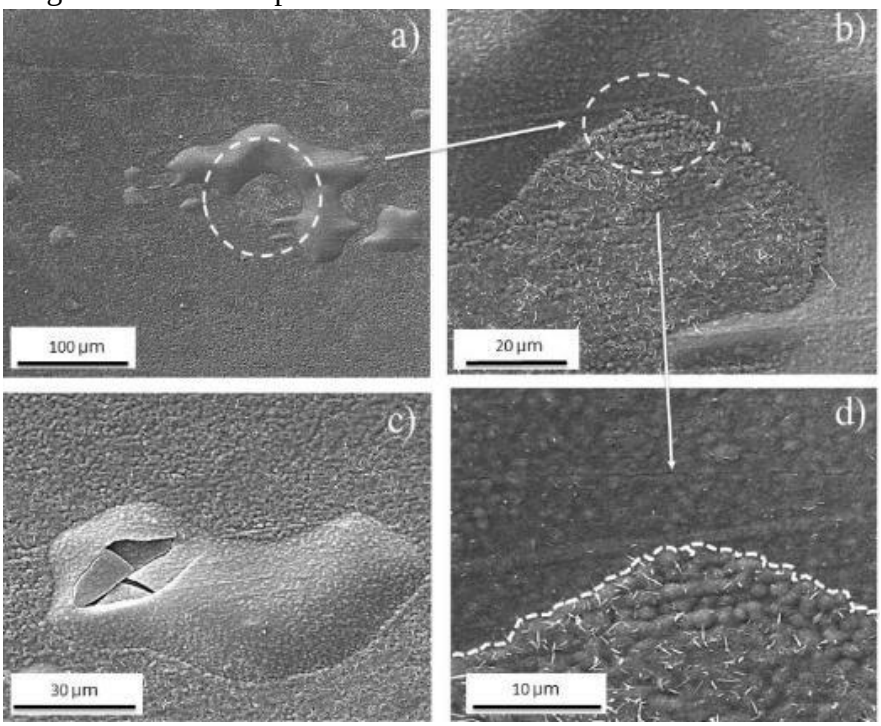

Source: Author (2021).

To observe the microstructure and to determine the oxide layer thickness, a cross-section using the focused ion beam (FIB) technique was used. Figure 42 presents the field emission scanning electron microscopy (FE-SEM) micrographs done on the oxide layer growth on Mar300 (Figure 42a,c) and Mar350 (Figure 42b,d) maraging steels. In both films, it is possible to observe the presence of little micro-holes, and mainly, a blister-like part of the film; this last defect present in the oxide layer (mentioned previously as protuberances) is related to differences in the expansion coefficient between the different constitutive phases, as well as being related to chemical heterogeneities along the oxide layer. From Figure 42c (oxide produced on Mar300) it was possible to observe that the oxide was not both homogeneous and continuous. In this sense, there is an air bubble that divides the oxide into two parts. The part of the oxide located above the bubble was the one with the thickest layer with a value ranging between 825 and 1310 nm; however, it was not homogeneous. From this SEM micrograph, it was also possible to distinguish two different kinds of oxide layers, one more obscure (external) and one clear (internal), which may be related to the presence of two different phases or compounds. The part of the oxide below the gas bubble was more homogeneous and its

thickness ranged between 601 to 790 nm. It was also possible to observe a small microstructure of fine grains with a different shade just below the oxide. From Figure 42e (oxide produced on Mar350) it is possible to observe a homogeneous oxide layer with a thickness of approximately 1700 nm; however, another part of the oxide was also appreciated with a gas bubble that divided the oxide in two different parts and which produced small cracks on their vertex. The part of the oxide located above it was small and relatively homogeneous, with a homogeneous thickness that ranged between 624 and 652 nm. Furthermore, differences in shades that may be attributed to the presence of two different phases and/or compounds were also observed. The part of the oxide below the gas bubble ranged between 865 and 1040 nm of thickness. In the same way as in Figure 42c, it is possible to observe the small fine-grained microstructure with a different shade just below the oxide. The lighter area on the outermost part of the oxide is due to the formation of more oxidized compounds, and the small metallic microstructure just below the metal–oxide interface with an austenitic-rich phase in Ni and Co formed because of the oxidation process (KLEIN; SHARON; YANIV, 1981; KLEIN; YANIV; SHARON, 1981; 1983; LUO; SHENZ, 2008; REZEK; KLEIN; YAHALOM, 1997).

Figure 42 – Field emission scanning electron microscopy (FE-SEM) cross-section micrograph and the magnification with the oxide layer thickness measurement on maraging 300 (a,c) and 350 (b,d) steels

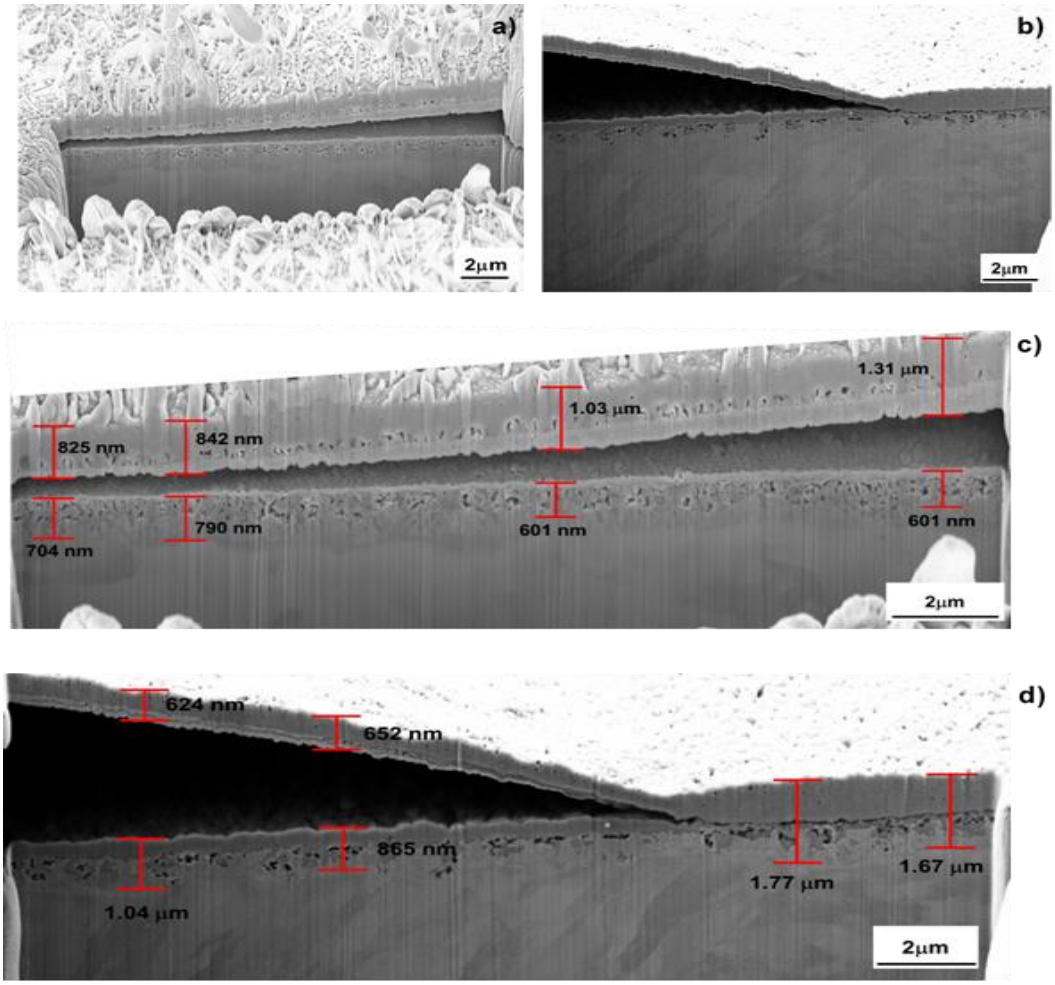

Source: Author (2021).

The results of the X-ray diffraction (XRD) analysis of the oxide layers for both steels are shown in Figure 43. In the two oxides, the same phases labeled as A, B, C, D, and E were identified, where the A peaks corresponded to a spinel ferrite, which may be iron, cobalt, nickel, or a mixture of them, according to ICDD (1975) and DĄBROWA *et al.* (2018). On the other hand, it was not possible to determine which types of spinel were formed because they have the same crystallographic structure and lattice parameters (KLEIN; SHARON; YANIV, 1981). The B peaks corresponded to hematite (Fe_2O_3) in agreement with ICDD (1975). The peaks labeled with C corresponded to TiO_2 (ICDD, 1975), while the D peaks corresponded to molybdenum oxide (MoO_3) (ICDD, 1975; ZHAO *et al.*, 2020). Finally, the E peak corresponded to the austenite phase (CONDE *et al.*, 2019). This phase was rich in Ni, Fe, and Co (KLEIN; SHARON; YANIV, 1981; KLEIN; YANIV; SHARON, 1981; 1983; REZEK; KLEIN; YAHALOM,

1997) and formed at the metal–oxide interface during the oxidation process when iron, cobalt, molybdenum, and titanium were oxidized and diffused through the oxide layer, leaving the steel surface with a high concentration of nickel; this phase is the microstructure of fine-grained metal with a darker color just below the oxide observed in Figure 42c,d.

Figure 43 – X-ray diffractograms of the oxide layer produced on the investigated maraging steels

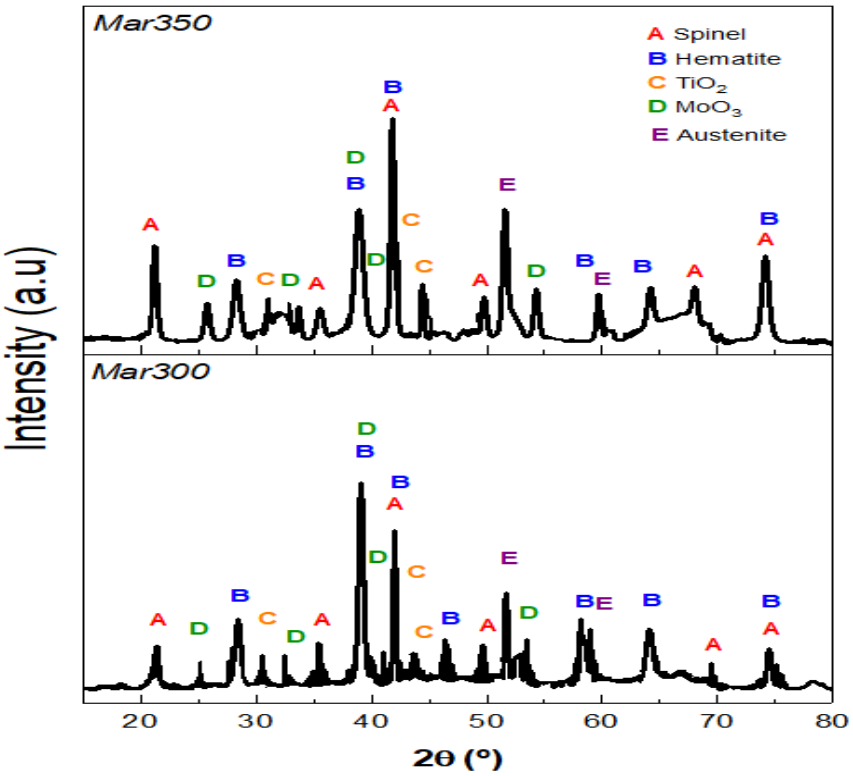

Source: Author (2021).

The semi-quantification of the phases presents in the oxides led to the determination of the phase formed in the oxide layer. The oxide layer created for the Mar300 maraging steel was mainly constituted by about 69.3% spinel, 23.8% hematite, 5.9% MoO_3, and 1% TiO_2. On the other hand, the other oxide layer was constituted by about 65% spinel, 23% hematite, 10% MoO_3, and 2% TiO_2. It is understandable that a higher amount of titanium oxide was found in Mar350 maraging steel due to the higher amount of this element in the chemical composition of this steel; however, the increase in the amount of molybdenum oxide cannot be associated with the amount of molybdenum in the chemical composition of this steel. The molybdenum content was almost identical in both steels, and this increase could thus be due to the greater amount

of cobalt that was used to decrease the solubility of molybdenum in steel, which produces a greater amount of intermetallic precipitates rich in molybdenum and titanium during the aging heat treatment (LIMA FILHO; BARROSA; GOMES DE ABREU, 2017; MAGNÉE *et al.*, 2020; SHA; CEREZO; SMITH, 1993; VASUDEVAN; KIM; WAYMAN, 1990); therefore, it is possible that on the surface of the maraging steel, this phenomenon provided a greater quantity of these elements that reacted and formed these oxides.

The Fourier transform infrared (FT-IR) spectra collected for the oxides of both steels are shown in Figure 44. The band located at 640 cm^{-1} corresponded to the of stretching vibration of Fe-O bonds in the structure of α-Fe_2O_3 (hematite), in agreement with Ding *et al.* (2020). On the other hand, the band located at 586 cm^{-1} corresponded to the stretching vibration of the Fe-O links in tetrahedral locations of the cobalt spinel structure—$CoFe_2O_4$— as reported previously (LI *et al.*, 2020; ROUTRAY; SAHA; BEHERA, 2020; WANG *et al.*, 2020; YANG *et al.*, 2020). Likewise, there were characteristic bands of MoO_3 at 993 cm^{-1} due to vibrations in the Mo=O bonds within the molecule, and at 859 cm^{-1} due to Mo-O-Mo bonds that connect the different molecules (RAMAR; BALASUBRAMANIAN, 2019; SHARMA; RAGUBANSHI; SHAH, 2020).

Figure 45 shows the Raman spectra for the oxide layer of each maraging steel grade investigated here. However, in both oxide layers, the same species were found. Hematite (α-Fe_2O_3) labeled as A (DE FARIA; LOPES, 2007; GUO *et al.*, 2020), spinel cobalt ferrite $CoFe_2O_4$ bands (B) (DE LA FIGUERA *et al.*, 2015; ROUTRAY; SAHA; BEHERA, 2020; WANG *et al.*, 2015), and Molybdenum oxide (MoO_3) were identified (C) (REED *et al.*, 2019; YANG *et al.*, 2019; ZHAO *et al.*, 2020). As was clearly evident in the FT-IR and RAMAN spectra, it was not possible to detect the titanium oxides, and this is an indication that this element was in the innermost layers.

Figure 44 – Fourier transform infrared (FT-IR) spectra of oxides produced on the maraging steels investigated here

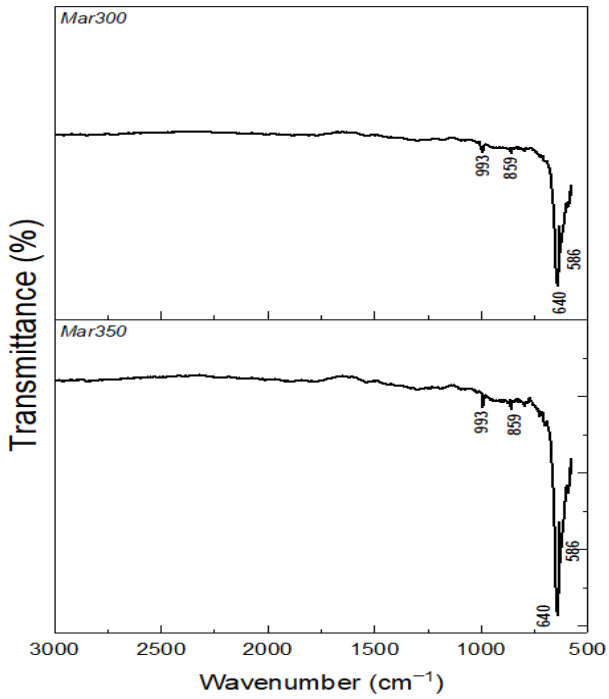

Source: Author (2021).

Figure 45 – Raman spectra of oxides produced for the maraging steels investigated here

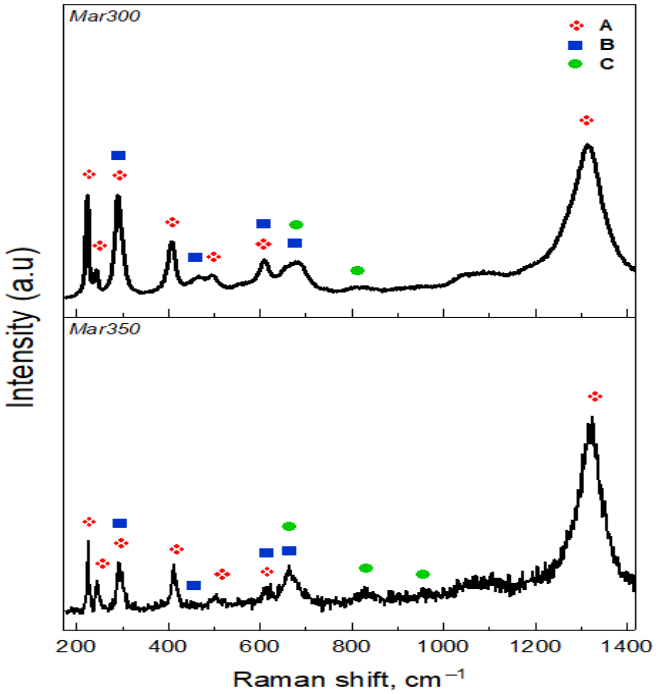

Source: Author (2021).

Figure 46a shows the survey X-ray photoelectron spectroscopy (XPS) spectrum of the oxide produced in Mar300 maraging steel, where the signals of the elements iron (Fe 2*p* and Fe 3*p*), carbon (C 1*s*), cobalt (Co 2*p*), and oxygen (O 1*s*) stand out. The chemical composition (in atomic concentration %) is also identified. Figure 46 also shows the high-resolution C 1*s* (b), O 1*s* (c), and Fe 2*p* (d) core-level spectra of the oxide produced on the maraging steel 300 grade before and after sputtering for 5 min with Ar^+ plasma. Tables 22 and 23 include the binding energy values (in eV) of the studied signals and the surface chemical composition, respectively. The C 1*s* core-level spectrum could be decomposed into four contributions (see Table 22). The main contribution at 284.8 eV was assigned to adventitious carbon, the other minor contributions at 285.6, 286.4, and 288.1 eV were derived from the presence of C-O, C=O, and O=C-O bonds, respectively (BARRECA *et al.*, 2001; KASPAR *et al.*, 2019). After etching for 5 min, there were only two contributions at 284.8 and 286.0 eV, and the surface concentration of C decreased from 47.94% to 18.4% (see Table 23), being indicative, as expected, of a adventitious contamination, which is very common on the surface of metals. The assignment of the oxygen species in the O 1*s* signal was not easy. The O 1*s* signal can be decomposed into three contributions at 529.3, 531.2, and 532.4 eV. The contribution at 529.3 eV, denoted as O, can be related to the presence of surface lattice oxygen (O_2^-), whereas the contribution at 531.2 eV, denoted as O, was assigned to the presence of defect oxide or to the surface low coordination oxygen ion. The third contribution at 532.4 eV mainly proceeded from the hydroxyl groups and C-O and C=O groups. After etching for 5 min, the relative intensity of the contribution due to lattice oxygens increased, and the relative intensity of the other two contributions decreased because of the removal of the surface contamination. In fact, the oxygen surface content slightly increased after etching, from 38.57% to 42.34% (see Table 23) (BARR, 1978; GALTAYRIES *et al.*, 1998).

The Fe 2*p* core-level spectra of the oxide produced on maraging steel 300 grade before and after etching for 5 min with Ar+ are shown in Figure 46, where the deconvolution of the Fe $2p_{3/2}$ signal is also included, and the corresponding values of the different contributions are shown in Table 22. It is well known that the position of the contributions of the Fe $2p_{3/2}$ signal, as well as its satellite peak, are very sensitive to the oxidation state of iron (GROSVENOR *et al.*, 2004; LIN; SESHADRI; KELBER, 1997; SANCHIS *et al.*, 1997). It is clear that the etching process modified the Fe 2*p* signal. Upon etching, the intensity of the signal increased and the surface iron content increased

from 10.13% to 31.12% in atomic concentration % (see Table 23). The deconvolution of the Fe 2$p_{3/2}$ main peak of the samples is also shown in Figure 46e. This peak was deconvoluted in three contributions at 708.9–709.2 eV assigned to Fe^{2+}, 710.6–710.8 eV assigned to Fe^{3+}, and 712.6–712.9 eV related to an interaction of Fe^{2+} and Fe^{3+} (LU *et al.*, 2007). It is interesting to know that the $Fe^{2+}/(Fe^{2+} + Fe^{3+})$ ratios on the surface of both samples were calculated from the XPS deconvolution (see Table 22), and as expected, the $Fe^{2+}/(Fe^{2+} + Fe^{3+})$ ratio increased after etching, indicating a higher proportion of the spinel phase $CoFe_2O_4$ and hematite (HONG *et al.*, 2019; HU *et al.*, 2007; KASPAR *et al.*, 2019; LIU *et al.*, 2019; YAN *et al.*, 2015; YAN *et al.*, 2016; YI *et al.*, 2020; ZHANG *et al.*, 2019). This was also supported by the higher cobalt content after etching (Table 23) from 3.24% to 8.14% in at. %. The shape of the Fe 2*p* spectra also indicated that magnetite (Fe_3O_4) was not formed.

The Co 2*p* core-level spectra (not shown) were very complex. The Co 2*p* spectrum before etching showed a maximum at 781.3 eV assigned to Co^{2+}, but this assignation was complex because the presence of Co^{3+} species cannot be ruled out. Upon etching, two maxima were observed at 780.7 and 782.0 eV. The new contribution at low-binding energy was assigned to reduced Co species (FANTAUZZI *et al.*, 2019; JI *et al.*, 2004; YAN *et al.*, 2015; YAN *et al.*, 2016; ZHAO *et al.*, 2019; ZHANG *et al.*, 2019). The Mo 3*d* signal was very noisy and hardly visible, and the Mo 3$d_{5/2}$ presented a maximum at 232.1 eV, assigned to Mo^{6+} from MoO_3 (SRINIVASAN; RAJAGOPAL *et al.*, 2011; RAVAPPAN, 2020; ZHAO *et al.*, 2020). Upon etching, the Mo 3*d* signal was not visible.

Figure 47 shows the survey spectra for the oxide produced on Mar350 maraging steel and the C 1*s*, O 1*s*, Fe 2*p*, and Mo 3d core-level spectra before and after etching for 5 min with Ar^+ plasma, and Tables 22 and 23 include the binding energy values (in eV) of the studied signals and the surface chemical compositions for the same samples. The C 1*s* high-resolution spectra (Figure 47b) were similar to those observed in the case of the maraging steel 300 grade sample, but the surface contents of C were lower, being 37.39% and 10.88% for the sample before and after etching. As aforementioned, some of the contributions of oxygen were due to the hydroxyl and hydrocarbon groups; the decrease of the carbon amount after etching was indicative of the fact that the surface of the oxide was less hydrophobic (BARR, 1978; BARRECA *et al.*, 2001; GALTAYRIES *et al.*, 1998; KASPAR *et al.*, 2019). The O 1*s* core-level spectra also

showed three contributions (Figure 47c and Table 22) at 529.7, 531.2, and 532. 4 eV, but in this case, the relative intensity of the surface lattice oxygen (O_2^-) was much higher, and the surface content of O 1*s* was also higher compared to that observed for sample maraging steel 300 grade. This also points out the higher observed hydrophilicity. After etching, the surface content of oxygen was barely modified. The Fe 2*p* core-level spectrum for maraging steel 350 was different (Figure 47d,e), with a much lower relative intensity of the contribution at 708.5 eV assigned to Fe^{2+}, and the calculated $Fe^{2+}/(Fe^{2+} + Fe^{3+})$ ratio was much lower (0.17). This fact points out that, before etching, this sample presented a high concentration of cobalt spinel. After etching, the $Fe^{2+}/(Fe^{2+} + Fe^{3+})$ ratio increased to 40, but interestingly, the Fe/Co atomic ratio was 36.64/18.14 = 2.01, very near to the theoretical value for the cobalt spinel $CoFe_2O_4$. However, this was not compatible with the relative high content of Fe^{2+}.

Figure 46 – X-ray photoelectron spectroscopy (XPS) spectra of samples with the oxide produced on maraging steel 300 (Mar300) before and after etching for 5 min with Ar^+ plasma (Mar300 5 min Ar^+). (a) Survey spectrum of sample Mar300: (b) C 1*s*, (c) O 1*s*, (d) Fe 2*p*, and (e) Fe $2p_{3/2}$ deconvoluted

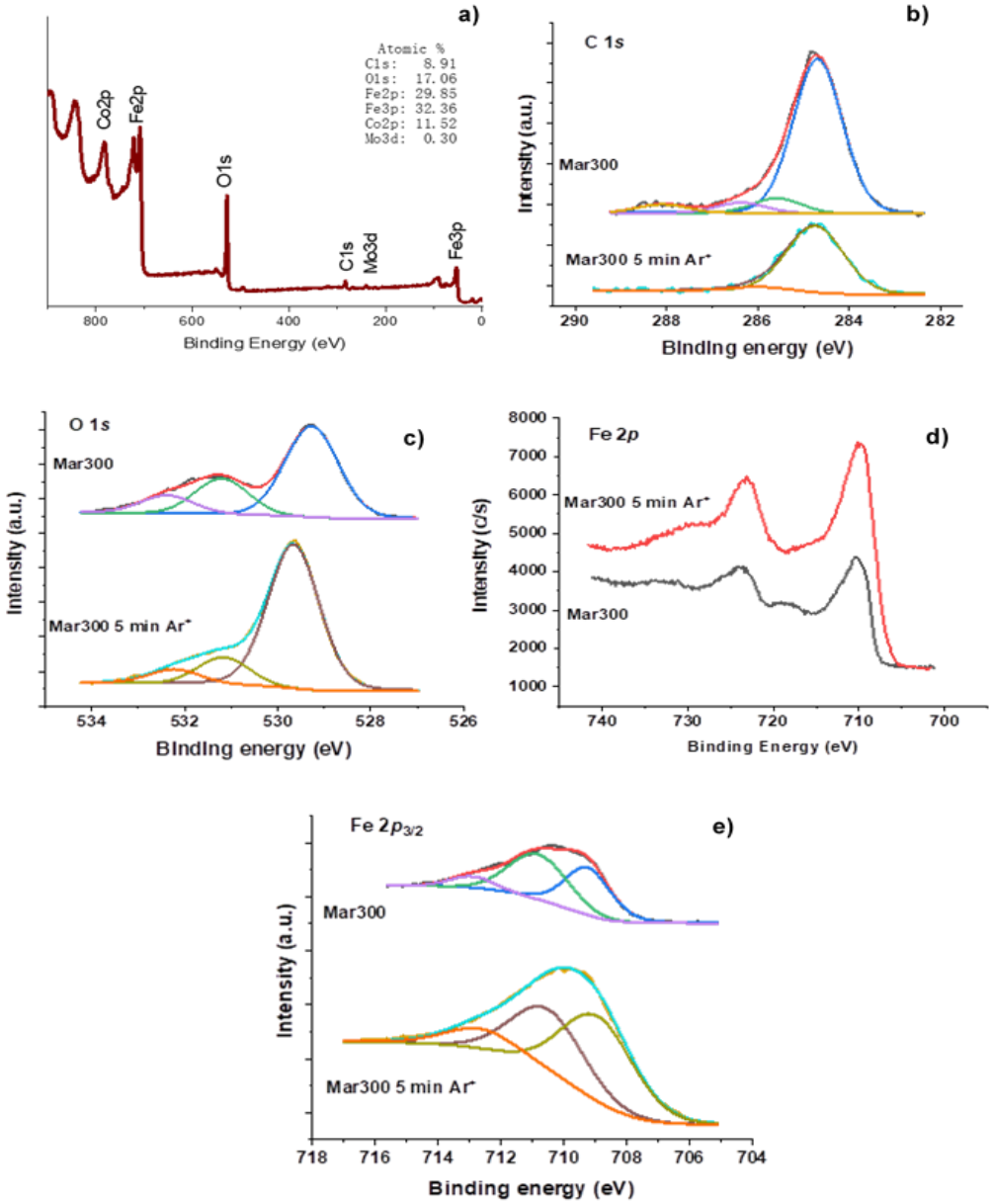

Source: Author (2021).

Table 22 – Binding energy values (in eV) of the studied elements, the percentages of the relative area in brackets, and the $Fe^{2+}/(Fe^{2+} + Fe^{3+})$ ratios for the studied oxide produced on maraging steels before and after etching for 5 min with Ar^+ plasma

Sample	**C 1*s***	**O 1*s***	**Fe 2$p_{3/2}$**	**Co 2$p_{3/2}$**	**Mo 3$d_{5/2}$**	**$Fe^{2+}/(Fe^{2+} + Fe^{3+})$**
Mar300	284.8 (82) 285.6 (8) 286.4 (5) 288.1 (5)	529.3 (63) 531.2 (24) 533.4 (13)	709.2 (43) 710.8 (48) 712.9 (9)	781.3	232.1	43
Mar300 5 min Ar^+	284.8 (95) 286.0 (5)	529.7 (78) 531.2 (14) 532.2 (8)	708.9 (50) 710.5 (37) 712.6 (13)	780.7 782.0		53
Mar350	284.8 (80) 286.0 (13) 288.0 (7)	529.7 (72) 531.2 (16) 532.4 (12)	708.5 (17) 710.2 (60) 712.4 (23)	780.7 782.7	232 (59) 232.7 (41)	17
Ma350 5 min Ar^+	284.8 (96) 287.4 (4)	529.8 (78) 531.1 (15) 532.4 (7)	708.4 (40) 710.0 (35) 712.4 (25)	782.3	232.1	40

Source: Author (2021).

Table 23 – Surface chemical composition (in at. %) for the studied oxide produced on maraging steels before and after etching for 5 min with Ar+ plasma

Sample	**C**	**O**	**Fe**	**Co**	**Mo**
Mar300	47.94	38.57	10.13	3.24	0.12
Mar300 5 min Ar^+	18.41	42.35	31.12	8.14	0.00
Mar350	37.49	42.58	14.83	4.90	0.20
Mar350 5 min Ar+	10.82	41.60	36.64	18.19	0.38

Source: Author (2021).

Figure 47 – X-ray photoelectron spectroscopy (XPS) spectra of samples with the oxide produced on grade 350 maraging steel before (Mar350) and after etching for 5 min with Ar^+ plasma (Mar350 5 min Ar^+). (a) Survey spectrum of sample, (b) C 1*s*, (c) O 1*s*, (d) Fe 2*p*, (e) Fe $2p_{3/2}$ deconvoluted, and (f) Mo 3*d*

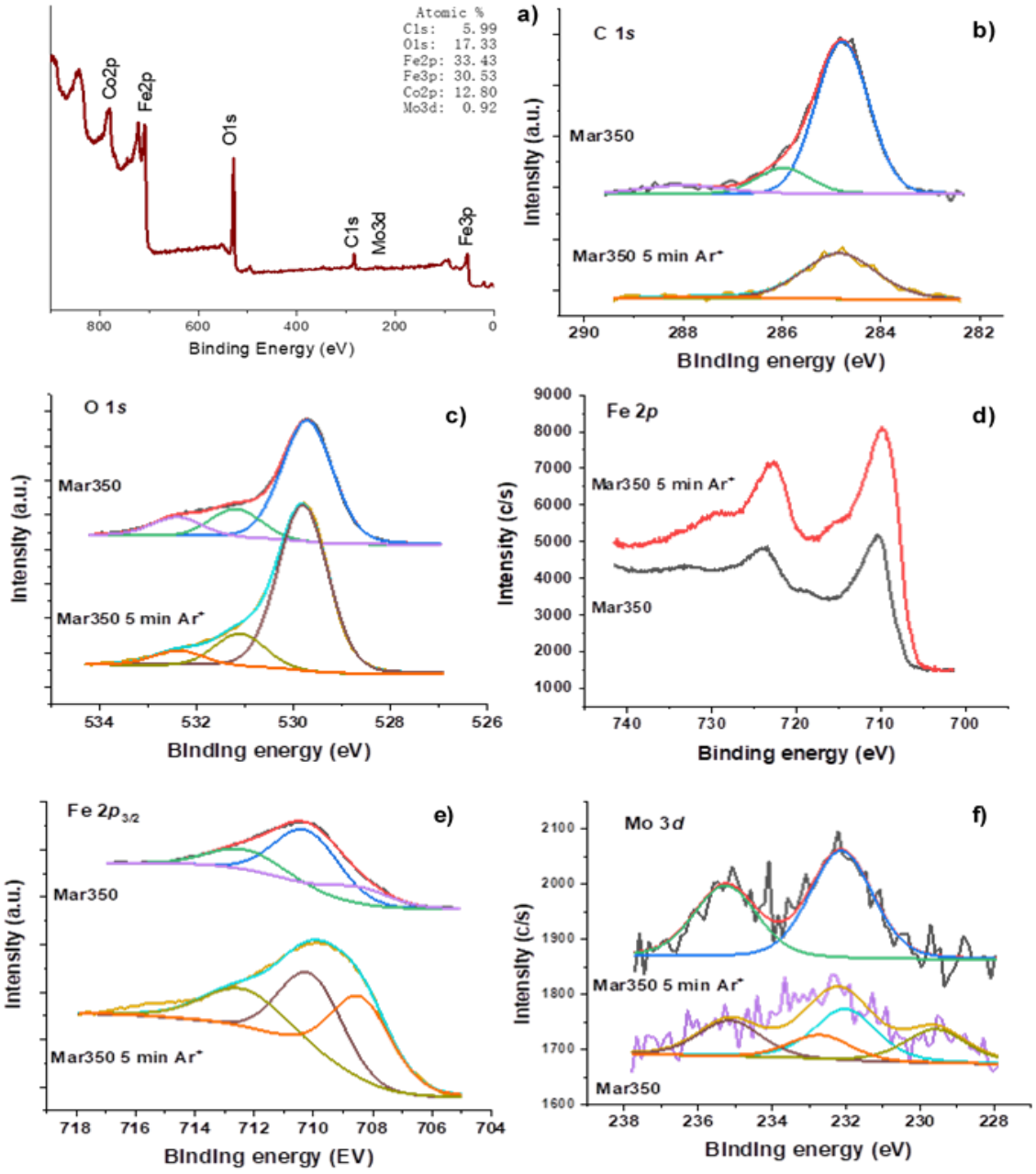

Source: Author (2021).

Scratch tests led us to determine the adhesive damage between the oxide layer and the metallic maraging alloy substrate, also denoted as Pc2 (ASTM, 2015c). Figure 48 (left hand side) exhibits the whole scratch track. The behavior was clearly discerned by comparing the micro-fracture events and damage features in regions close to the track edges. Figure 48 (right hand side) shows top-view field emission scanning electron

microscopy (FE-SEM) images of nanoscratch tracks, where some interesting features are clearly visible—mainly, chipping, also known as decohesion. Furthermore, the Pc2 directly determined from the FE-SEM micrographs are summarized in Table 23. From Figure 48 and the data summarized in Table 24, it is clearly visible that the oxide layers grown on the maraging 350 alloy required a higher force in order to detach the oxide layer growth under the CO_2 atmosphere from the metallic maraging substrate.

Figure 48 – (a) Field emission scanning electron microscopy (FE-SEM) image for the nanoscratch track and (b) magnification of the top-view FE-SEM images of nanoscratch tracks where the first adhesive damage appears

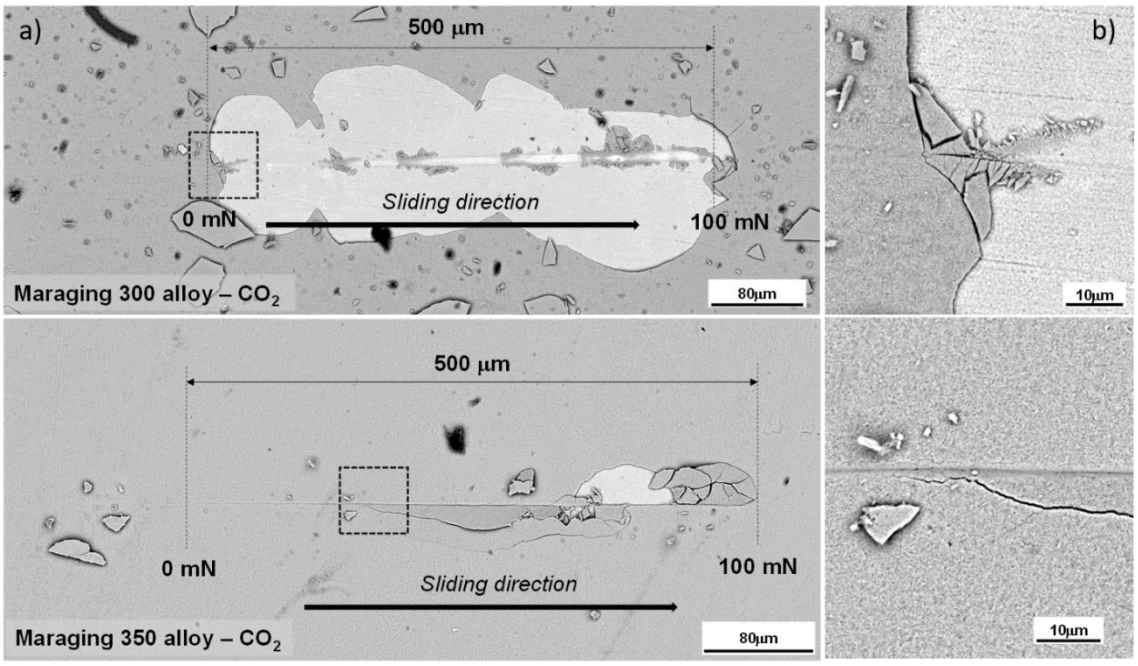

Source: Author (2021).

Table 24 – Pc2 directly determined from the field emission scanning electron microscopy (FE-SEM) micrographs for each oxide produced on each maraging steel

Maraging Steel	Pc2 (mN)
Mar300	2
Mar350	25

Source: Author (2021).

The results on both oxide layers showed that the film was not homogeneous and that several phases formed the layer. The processes of how they are formed and grown have been approached by several authors from different points of view, and divergent information has been found. On the basis of the results found in this work, several points can be highlighted; one of them is that TiO_2 is in the innermost layers of the oxide,

because it was not detected by X-ray photoelectron spectroscopy (XPS). Only the X-ray diffraction (XRD) that penetrated through different layers was able to detect it. This observation is in fair agreement with Luo and Shenz (2008), Surman (1973), Subbaraman, Deshmukh and Sankaranarayanan (2013), Klein, Sharon and Yaniv (1981) and Klein, Yaniv and Sharon (1981; 1983), based on thermodynamic information from experiments conducted under a steam atmosphere, which highlighted that, in the first stage of oxidation process, all elements were oxidized, and mainly titanium, which exhibited high reactivity with oxygen, but it ended up being covered by iron oxides because of the faster kinetics of the oxide formation reactions of this element. The same statement was made for MoO_3, but the results obtained from Raman and Fourier transform infrared (FT-IR) techniques detected this oxide in the outermost layers. These results were related to the chemical composition of steels, although the amount of molybdenum was similar between them, there was a difference in the amount of cobalt, which for this research was between 9.5 wt. % and 11.6 wt. %, which is slightly higher than the levels reported by Klein, Sharon and Yaniv (1981) and Klein, Yaniv and Sharon (1981; 1983), who reported a value of around 8 wt. %.

Klein, Sharon and Yaniv (1981), Klein, Yaniv and Sharon (1981; 1983) and Rezek, Klein and Yahalom (1997) reported that the oxide formed was magnetite (Fe_3O_4), but in this research, cobalt ferrite, $CoFe_2O_4$, and hematite (α-Fe_2O_3) were found. According to the literature (BLIEM *et al.*, 2015; DĄBROWA *et al.*, 2018; GENUZIO *et al.*, 2016; PARDAVI-HORVATH, 2000; RODRIGUES *et al.*, 2015; TSUKIMURA; SASAKI; KIMIZUKA, 1997), also it is possible to generate hematite, and the main reaction to generate it is a diffusion reaction, specifically by the diffusion of cobalt and nickel in the form of Co^{2+} and Ni^{2+} species from the metallic matrix to the outside. These ions end up occupying the octahedral sites of spinel, replacing Fe^{2+} iron, and displacing it to the outside of the film, where it is exposed to a higher concentration of oxygen, and they are oxidized to Fe^{3+}. The formation of nickel-rich austenite in the oxide–metal interface is due to the decomposition of the martensite at temperatures above 500 °C (SILVA *et al.*, 2019). However, remnants of iron and nickel may be subsequently present within the formed spinel (JEON *et al.*, 2013; LUO; SHEN, 2008; PARDAVI-HORVATH, 2020; PARKINSON, 2016; SUBBARAMAN; DESHMUKH; SANKARANARAYANAN, 2013). This statement was confirmed with the results of the

energy dispersive X-ray (EDS) measurements made on the surface of the oxide layer, where small amounts of nickel were detected.

The formation of hematite is related to the atmospheres used in the heat treatment in this research. Zhang *et al.* (2016) and Hong *et al.* (2019) described that iron-based materials oxidized at temperatures between 377 °C and 527 °C under steam, and mainly with CO_2 atmospheres, producing negative free energy for the formation of hematite; therefore, under these conditions, part of the magnetite exposed to higher concentrations of oxygen (outermost layers) is oxidized to hematite ($Fe_3O_4 \rightarrow \alpha\text{-}Fe_2O_3$) (GENUZIO *et al.*, 2016; SUBBARAMAN; DESHMUKH; SANKARANARAYANAN, 2013; ZHANG *et al.*, 2016). Genuzio *et al.* (2016) also mentioned that the kinetics of this transformation are very fast and that it depends on the chemical composition and the availability of defects in the crystalline network, which allow for the growth of the new phase through specific crystallographic plans. According to Genuzio *et al.* (2014), from 397 °C, $\alpha\text{-}Fe_2O_3$ is formed in the middle of the magnetite, which grows dendritically and with morphological differences that distinguish it from the matrix. Similar differences were mentioned by Genuzio *et al.* (2016), and these findings coincided with the protuberances found in the oxides of this research.

4.4.3 Conclusions

Both maraging steel grades studied in this research presented a non-homogeneous oxide layer, with several defects spread over the entire surface, such as holes that exposed more internal layers, cracks, porosity, and high roughness. The oxide formed was composed of four different phases, the majority being cobalt spinel ferrite ($CoFe_2O_4$), hematite ($\alpha\text{-}Fe_2O_3$), molybdenum oxide (MoO_3), and titanium oxide (TiO_2).

The conditions of time, temperature, and atmospheres used in the heat treatment allowed us to have a percentage of more than 65% of spinel for both steels.

It was found that the chemical composition of the oxide changed over depth; the inner parts were richer in alloy elements, and in general, the outer ones were richer in iron. An example of this is that the largest amount of titanium, nickel, and molybdenum was found in the inner parts of the oxide. These findings were confirmed when TiO_2 and nickel-rich austenite were only detected by low-angle X-ray diffraction (XRD), which highlighted that these elements were located on the metal–oxide layer interface. This fact

is related to a greater amount of cobalt in its chemical composition. This element acts so that molybdenum forms fine intermetallic precipitates during aging, which ends up making it available on the surface and creates conditions for its oxidation.

The formation of hematite depended strongly on the temperatures, partial pressure of oxygen, and the atmospheres used in the heat treatments. Under these conditions, part of the surface magnetite turned into α-Fe_2O_3 with a different morphology and with a chemical composition with few alloying elements. The low diffusion of nickel, a product of the formation of rich austenite, in this element together with an increase in the chemical composition of cobalt in these steels (with its ions with a high preference for occupying the octahedral sites in the network) influenced the transformation of the initially formed magnetite in $CoFe_2O_4$ cobalt ferrite. However, different nickel contents were detected in energy dispersive X-ray (EDS) measurements made on the different exposed oxide layers, which means that, together with iron, this element can replace cobalt inside the spinel.

The maraging 350 steel presented a good adherence between the oxide layer and the metallic substrate growth under the CO_2 atmosphere. This demonstrates its capability for being used under aggressive conditions.

4.5 Synthesis and characterization of a Fe/Co ferrites spinel oxide film produced by N_2/steam heat treatment on two maraging steels

4.5.1 Review

An experimental procedure has been developed to obtain an oxide layer formed mainly by spinel on maraging steels. It consists of different stages with specific conditions, such as atmospheres rich in nitrogen and water vapor, and different steps of temperatures and times. Tests have been performed on two maraging steel grades, i.e, 300 and 350. Oxide layer characterization has been done by using optical and electron microscopy, spectroscopy, X-Ray diffraction and using the nanoscratch tests in order to determine the adhesion force as well as to observe the main deformation mechanism induced under sliding tests. In both steels, oxide layers are formed by the spinel's Fe_3O_4 and $CoFe_2O_4$ in amounts close to ~ 85%, whereas TiO_2 and MoO_3 represent the other 15%. No hematite has been found. The low oxygen availability during the heat treatment

was fundamental for avoid hematite formation. A nickel-rich austenitic phase formed at the metal-oxide interface due the kinetics of the oxidation process of the cobalt, iron, and molybdenum. The particular conditions of the heat treatments induced the formation of a mixture of iron, nickel, and cobalt spinel ferrites, thereby contradicting previous studies which said that only magnetite would be formed. The sliding tests at the nanometric length scale highlight that the layer formed on maraging 300 grade presents a better adhesion than the other investigated material due to it requires more load in order to induce cracks located at the edge of the sliding track and subsequently the chipping of the formed layer.

The present investigation intends to produce an oxide with the largest amount of spinel. Moreover, the conditions of temperature, time and atmosphere were selected to avoid the formation of hematite. A standard experimental procedure has been established (with similarities to that presented in the publication by Cerra Florez *et al.* (2021) that can be reproduced under basic laboratory conditions. The main objective of this work is focused on verifying if the conditions of the heat treatment and the chemical composition of the steels used are sufficient or not for the formation and growth of a spinel type oxide on the surface of the steels. A horizontal tubular furnace, nitrogen gases and steam were used in the different stages of the thermal aging treatment of maraging steels grade 300 and 350.

4.5.2 Results and Discussion

The oxide layer of all samples was observed and analyzed using different techniques. With CLSM several heterogeneities were found distributed along the oxide layer, such as cracks, ridges, peeling and valleys. In Figure 49, it is possible to appreciate some peeling and cracks on the oxide surface. According to Cerra Florez *et al.* (2021), this kind of defects may be related to the volumetric differences between the different phases forming the oxide layer, as well as to the steam condensation on the surface.

Figure 49 – Optical (a,c) and laser scanning confocal microscopy (LSCM) (b,d) micrographs of the heterogeneities found on the oxide layer for grade 300 (a,b) and grade 350 (c,d) maraging steels

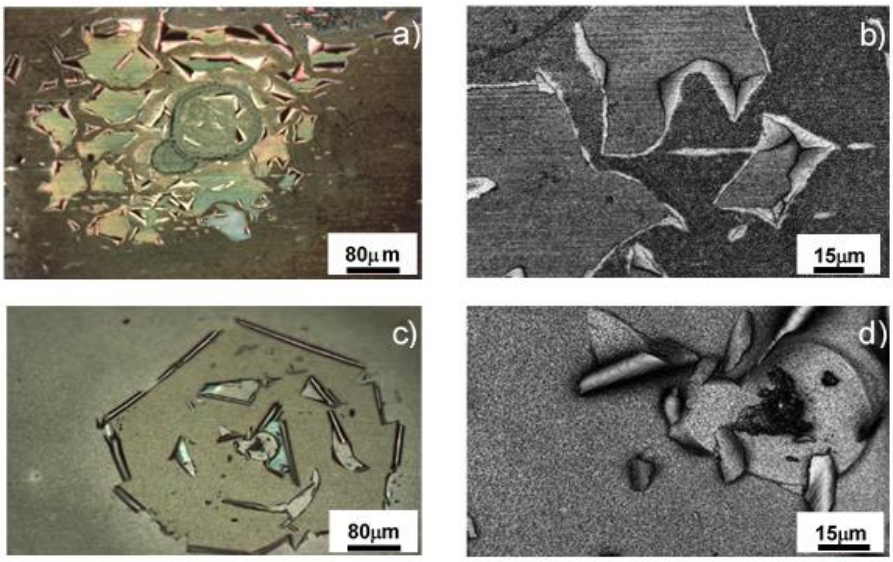

Source: Author (2021).

Figure 50 shows AFM topographic images in 3D-view (20 x 20 μm^2, 5 x 5 μm^2 and 1 x 1 μm^2) of the surface quality of the oxide produced on grade 300 (Figure 50a,b,c) and on grade 350 too (Figure 50d,e,f). From these images, it was possible to directly extract the main roughness parameters (i.e., maximum roughness, maximum and minimum roughness peaks; Rz, Rp and Ry, respectively), as summarized in Table 25. Several different microstructural features (i.e., porosity, picks, valleys, etc.) are clearly visible, heterogeneously distributed along the surface. With the observation of these images and the analysis of the values in Table 25, it is evident that the oxide layer growth on 300 maraging steel grade grows more heterogeneously, in a non-uniform way and with higher roughness than on grade 350.

Figure 50 – Topographic atomic force microscopy (AFM) image (3D view) of the oxide layer growth on grade 300 maraging steel (a, b, c) and grade 350 maraging steel (e, f, g)

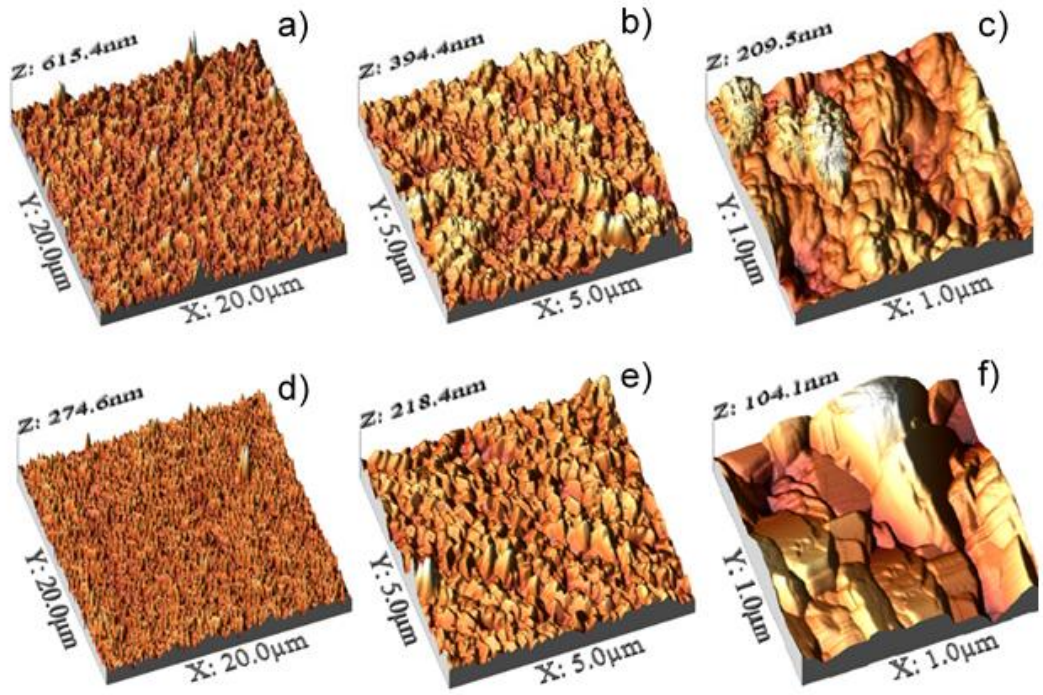

Source: Author (2021).

Table 25 – Surface roughness of the oxides produced on grade 300 and 350 maraging steels

Oxide Sample	Length (µm)	Roughness Ave. (Ra) (nm)	Roughness Max. (Rz) (nm)	Max Peak ht (Rp) (nm)	Maximum Depth (Rv) (nm)
Mar300	20 (Figure 3a)	43 ± 0.5	615	421	-194
	5 (Figure 3b)	36 ± 0.5	394	241	-153
	1 (Figure 3c)	24 ± 0.3	209	122	-87
Mar350	20 (Figure 3d)	15 ± 0.5	274	193	-82
	5 (Figure 3e)	14 ± 0.4	218	138	-80
	1 (Figure 3f)	15 ± 0.3	104	60	-43

Source: Author (2021).

X-ray diffractograms before oxidation and the oxide film produced in both steels are shown in Figure 51. Specifically, in Figure 51a diffractograms of the samples annealed at 840 ºC for 1 hour are given and it is possible to identify the peaks (110), (200) and (211), that correspond to the martensitic (α') phase, in fair agreement with works (CERRA FLOREZ *et al.*, 2021; CONDE *et al.*, 2019; VIANA *et al.*, 2013). Figure 51b resembles the diffractograms of the oxide layers for both steels. In the two oxides, the same phases, labeled as A, B, C and D were identified. Peaks correspond to a spinel ferrite which may be iron, cobalt, nickel, or a mixture of them, according to ICDD (1975),

Dabrowa *et al.* (2018) and Cerra Florez *et al.* (2021). On the other hand, it was not possible to determine which types of spinel are formed because they have the same crystallographic structure and lattice parameters (CERRA FLOREZ *et al.*, 2021; KLEIN; SHARON; YANIV, 1981). The peaks labeled with B correspond to TiO_2 (ICDD, 1975), while C peaks relate to molybdenum oxide (MoO_3) (ICDD, 1975; ZHAO *et al.*, 2020). Finally, E peaks match with the austenite phase γ- (CONDE *et al.*, 2019), rich in Ni, Fe and Co, and formed due the oxidation process at the metal/oxide interface (CERRA FLOREZ *et al.*, 2021; KLEIN; YANIV; SHARON, 1981; 1983; KLEIN; SHARON; YANIV, 1981; REZEK; KLEIN; YAHALOM, 1997).

Figure 51 – X-ray diffractograms of a) solution annealed state, b) oxide layers produced on both maraging steels

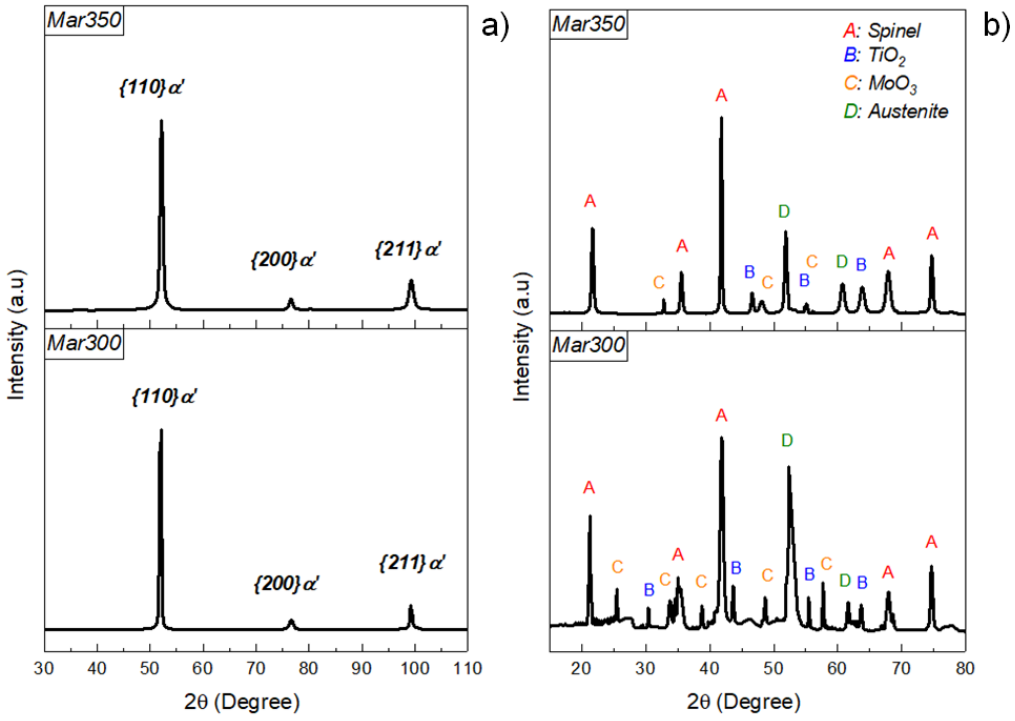

Source: Author (2021).

Therefore, the quantification of the phases in the oxides led to the following results: oxide formed on maraging 300 is constituted by around 86 % spinel, 8 % MoO_3 and 6 % TiO_2. In the case of the oxide produced on grade 350, the approximate composition was: 87 % spinel, 5 % MoO_3 and 8 % TiO_2. It is important to highlight that the spinel peaks present in the XRD diffractograms also fit with Fe_3O_4, $NiFe_2O_4$, and $CoFe_2O_4$, which have similar crystallographic parameters. However, this technique does not lead to isolating each contribution as reported Klein, Sharon and Yaniv (1981). The

high percentage of spinel, together with the absence of hematite peaks, shows the effectiveness of the conditions chosen in the procedure to form spinel oxide in these steels. The higher amount of TiO_2 found in the oxide of maraging 350 can be explained by the higher amount of this element in its chemical composition. According to the work of Klein, Yaniv and Sharon (1983), titanium has a greater reactivity than the other elements under these treatment conditions (steam atmosphere at 485 ºC), given the most negative values of free formation energy (ΔF) of Ti oxide (-204 kcal) compared to Fe (-142 kcal) and Mo oxide (-121 kcal). Moreover, this increase in titanium and its greater reactivity has the consequence that a lower amount of molybdenum oxide has been found, and this decrease cannot be associated with the amount of molybdenum because Mo content is almost identical in both steels.

The oxide layer morphology from both maraging steels, as observed by SEM, is illustrated in Figure 52. Several heterogeneities and defects are visible. Thus, in Figure 52a a surface completely covered with several heterogeneities, including holes and peeling, is shown. In Figure 52b, numerous porosities are observed over the entire oxide surface. Also, in Figure 52c porosities are observed in more detail and also an area not covered with external oxide. Then, points highlighted with letters A and B identify the positions where the chemical analysis by EDS were performed. The results summarized in Table 26 highlight a chemical composition difference: the inner part of the oxide is richer in nickel, titanium, and molybdenum, while the upper part is mainly rich in iron and cobalt. Figure 52d shows a covered oxide surface area without defects. Differently dispersed heterogeneities, such as cracks, holes, ridges, valleys, and peeling showing the internal oxide, are observed in Figure 52e. Punctual EDS analysis was also carried out on the external surface and the internal oxide exposed by the peeling, whose results are summarized in Table 27. As depicted in this Table, the differences between the chemical composition at points A and B show that the inner part of the oxide is richer in alloying elements than the oxide surface, confirming a different concentration in the different parts of the oxide layer. This fact can indicate the existence of different phases or compounds dispersed along with the oxide layer thickness. Finally, in Figure 52g a linear EDS analysis was performed following the yellow dash line, in order to compare from the chemical point of view the two holes with the internal area exposed (A and B) and the external zone of the oxide layer. As shown in Figure 52h, the EDS spectra conducted inside a rectangular hole shape (point A) with straight edges presents a chemical

composition rich in titanium and nitrogen, which may be related to the formation of titanium nitride (TiN) during the solidification process of steels with an appreciable content of titanium (DESCOTES *et al.*, 2015; 2020), in concordance with results previously reported by Capurro and Cicutti (2018) and Silva *et al.* (2018). The EDS spectrum of the irregular hole (point B) indicates that it is rich in molybdenum due to the intermetallic compounds (Ni_3Mo and Fe_3Mo) that precipitate during the aging treatment, as reported in Cerra Florez *et al.* (2021), Magnée *et al.* (2020), Moshka *et al.* (2015), Petty (1970), Rack and Kalish (1971) and Rodrigues, Bernardi and Otubo (2014). It is essential to indicate that oxygen was only taken into account for comparative purposes.

Figure 52 – Scanning electron microscope (SEM) micrographs of the oxide formed on grade 300 (a, b, c) and 350 (d, e, g, f) maraging steels, and g) linear Energy-dispersive X-ray spectroscopy (EDS) spectrum of the oxide formed on grade 300 maraging steel

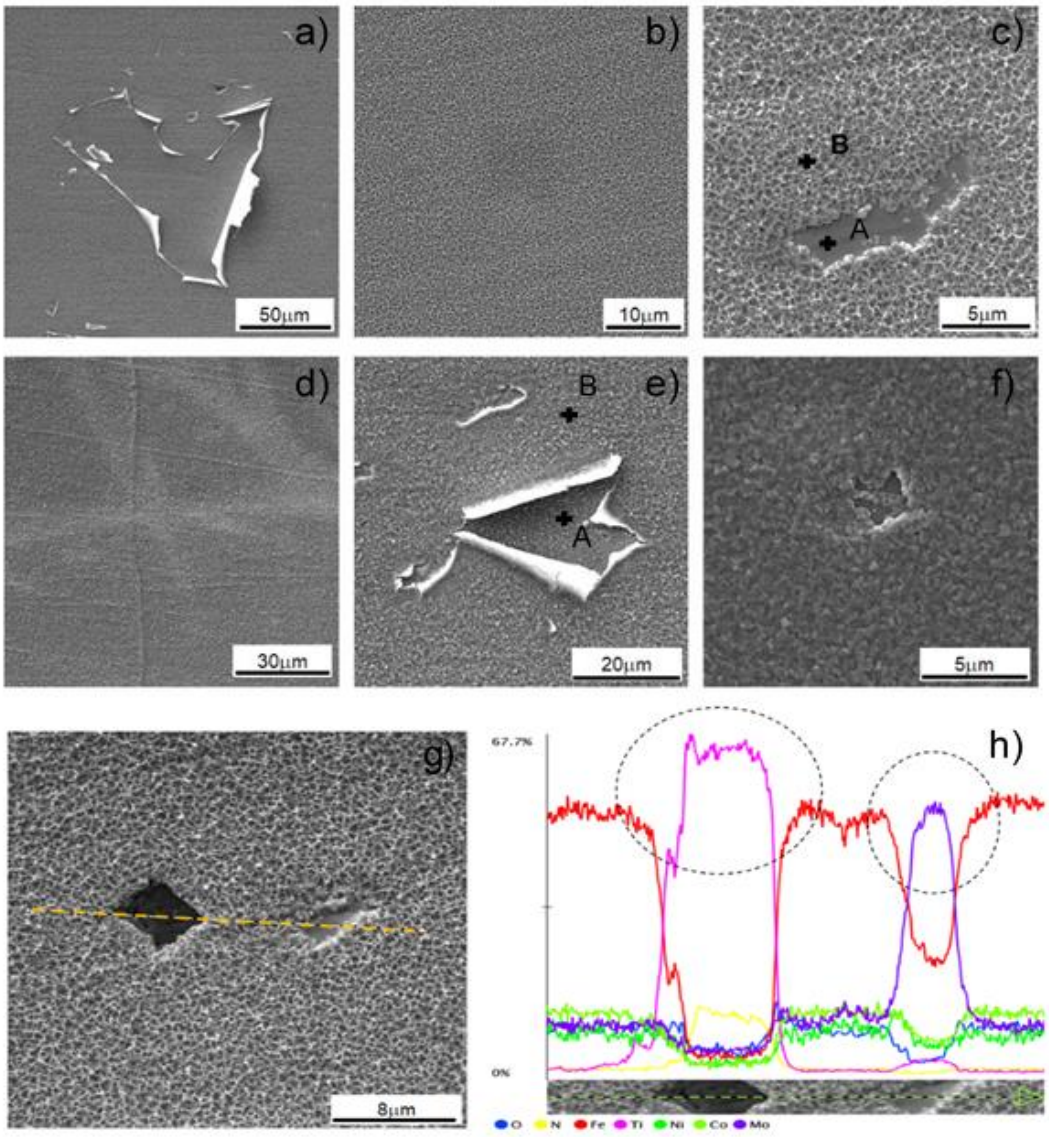

Source: Author (2021).

Table 26 – Energy-dispersive X-ray spectroscopy (EDS) spot measurements taken at the different locations shown in the Figure 52c

EDS quantitative analysis from A and B points			
Element Number	Element Symbol	**Point A**: (Weight Conc.)	**Point B** (Weight Conc.)
26	**Fe**	47.18	56.67
8	**O**	23.11	27.36
27	**Co**	4.84	6.12
28	**Ni**	7.42	5.55
42	**Mo**	14.68	3.80
22	**Ti**	2.77	0.50

Source: Author (2021).

Table 27 – Energy-dispersive X-ray spectroscopy (EDS) spot measurements taken at the different locations shown in the Figure 52e

EDS quantitative analysis from A and B points			
Element Number	Element Symbol	**Point A**: (Weight Conc.)	**Point B** (Weight Conc.)
26	**Fe**	52.06	59.53
8	**O**	26.01	34.37
27	**Co**	6.54	4.80
28	**Ni**	6.56	0.62
42	**Mo**	7.56	0.58
22	**Ti**	1.27	0.10

Source: Author (2021).

In order to observe and determine the thickness of the oxides produced on both maraging steels, cross-sections micrographs were done using focused ion beam (FIB). In Figure 53a is possible to observe the platinum plate (used for protection during the assay), the oxide layer and the steel matrix through the cross-section on the oxide produced on maraging steel grade 300. On the other hand, the micrograph in the Figure 53b shows a homogeneous oxide layer with a thickness ranged between 857 to 1319 nm, and medium thickness around 1007 ± 125 nm. The oxide film presents an irregular outer surface with a series of pore-like defects on the internal parts. A closer inspection (Figure 53c) shows the oxide layer with a uniform dark shade that suggest no variations of the phases, also a lighter shade with small grain size is observed on the steel side of the metal-oxide interphase, which could indicate the presence of a different phase from the rest of the metallic matrix of the steel. This assumption was confirmed by performing the linear EDS chemical analysis (Figure 53d) in the yellow line in Figure 53c. It is essential to indicate that oxygen was only taken into account for comparative purposes. These EDS analysis highlight that the oxidized layer presents a uniform distribution from a chemical point of view. In Figure 53d it is evident that Co and Ni present a higher concentration in the oxide layer near the metal base interface (specifically in the dash black circles in both Figures). This result shows the presence of an austenitic bonding layer rich in nickel, cobalt and iron at the oxide layer/metal base interface formed during the oxidation process (CERRA FLOREZ *et al.*, 2021; KLEIN; YANIV; SHARON, 1981; 1983; KLEIN; SHARON; YANIV, 1981; REZEK; KLEIN; YAHALOM, 1997) and found by XRD analysis made on the samples.

In Figure 54a is observed a cross-section of the oxide produced on maraging steel grade 350. The micrography in Figure 54b shows the similar defects (irregular outer

surface and with a series of pore-like defects on the internal parts) founds in Figure 53b and a homogeneous oxide layer with a thickness ranging between 716 to 1288 nm, and medium-thickness around 889 ± 160 nm. The closer inspection in Figure 54c shows a uniform dark shade on the oxide film and a lighter shade on the steel side of the metal-oxide interphase. The linear EDS chemical analysis (Figure 54d) performed in the yellow line in Figure 54c confirms a chemical uniform distribution on the oxide, and as found in the oxide produced on maraging steel grade 300, a higher concentration of Co and Ni at the metal-oxide interface (in the areas with dashed black circles in both Figures). This result confirms the formation of an austenite phase rich in Ni, Co and Fe in the metal-oxide interface during the oxidation process and found by XRD analysis. It is essential to indicate that oxygen was only taken into account for comparative purposes.

Figure 53 – Scanning electron microscope (SEM) micrographs of the oxide layer formed on maraging 300 steel, (a) focused ion beam (FIB) cross section micrograph of the oxide layer, (b) thickness of the oxide layer, (c) magnification of the oxide layer showing a yellow line where the chemical composition was determined, and d) energy-dispersive X-ray spectroscopy (EDS) chemical elements profiles conducted on the through the yellow line of the Figure 53c

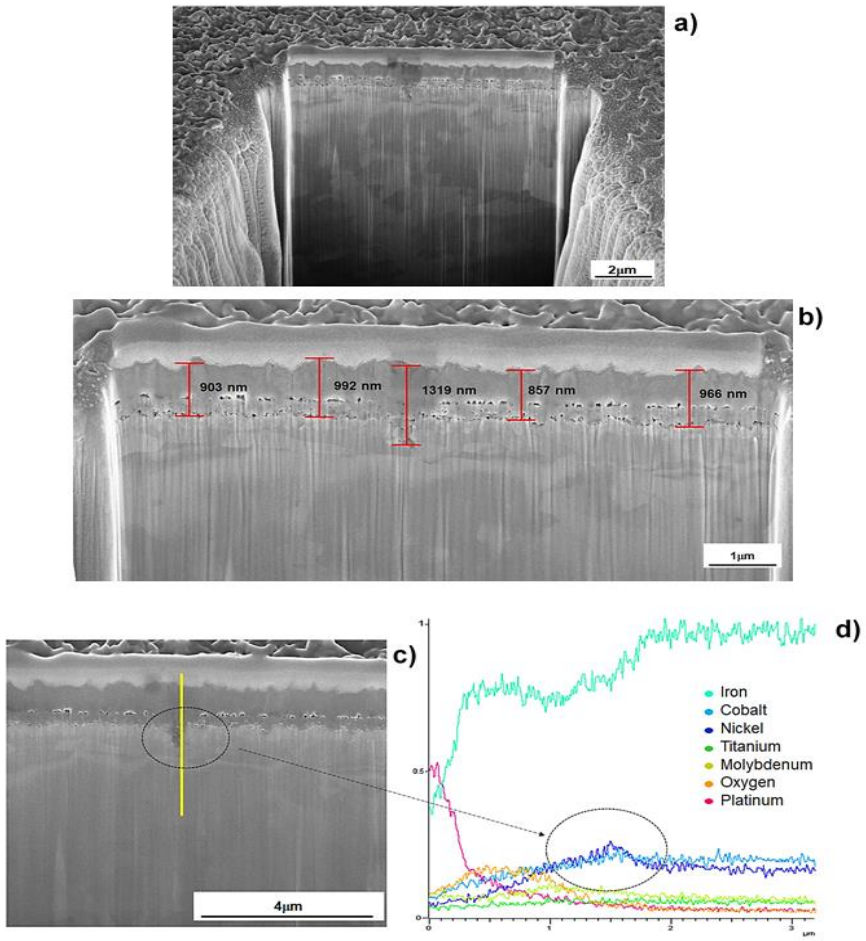

Source: Author (2021).

Figure 54 – Scanning electron microscope (SEM) micrographs of the oxide layer formed on maraging 350 steel, (a) focused ion beam (FIB) cross section micrograph of the oxide layer, (b) thickness of the oxide layer, (c) magnification of the oxide layer showing a yellow line where the chemical composition was determined, and d) energy-dispersive X-ray spectroscopy (EDS) chemical elements profiles conducted on the through the yellow line of the Figure 54c

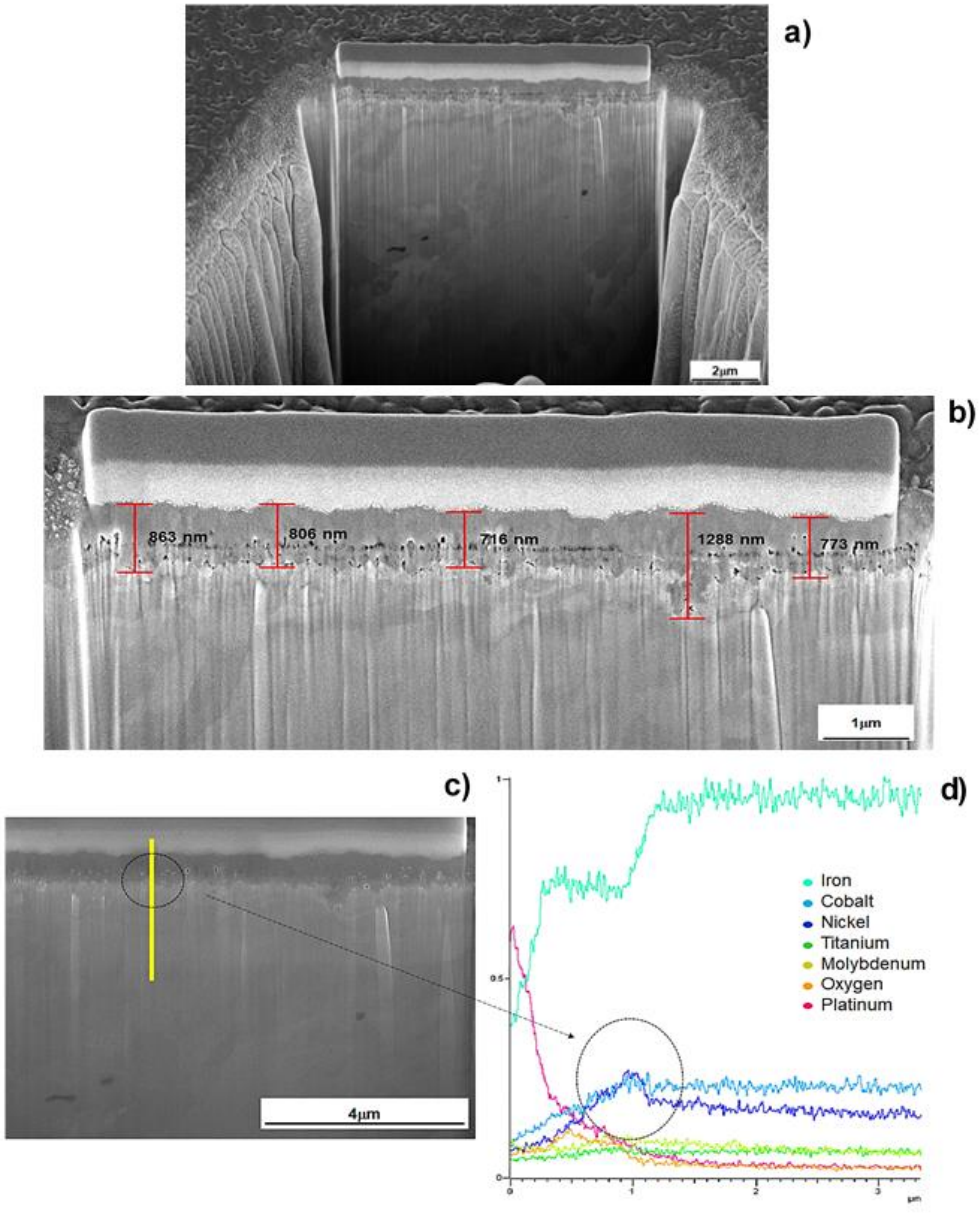

Source: Author (2021).

For the identification of spinel types formed in the oxides of both steels, Raman spectroscopy and X-ray photoelectron spectroscopy techniques were used. Figure 55a shows the Raman spectrum obtained from the oxide layers, in which it is possible to see two spinels: iron ferrite (Fe_3O_4) (CERRA FLOREZ *et al.*, 2021; KUMAR *et al.*, 2014; ROBINSON *et al.*, 2019) labeled as A, and cobalt ferrite ($CoFe_2O_4$) (CERRA FLOREZ

et al., 2021; DE LA FIGUERA *et al.*, 2015; ROUTRAY; SAHA; BEHERA, 2020; WANG *et al.*, 2015) labeled as B. Furthermore, by doing a magnification at a Raman shift ranged between 150 and 750 cm^{-1} (Figure 55b), spinel peaks are more clearly visible and the bands for each compound are more detailed. These results confirm the existence of all expected spinels, whereas no hematite bands are detected. These results are in agreement with the XRD finding. Raman did not find MoO_3 and TiO_2 because these compounds are in the innermost layers, as these techniques analyze the outermost layers of the oxide (CERRA FLOREZ *et al.*, 2021).

Figure 55 – Raman spectra of oxides produced on the maraging steels investigated here

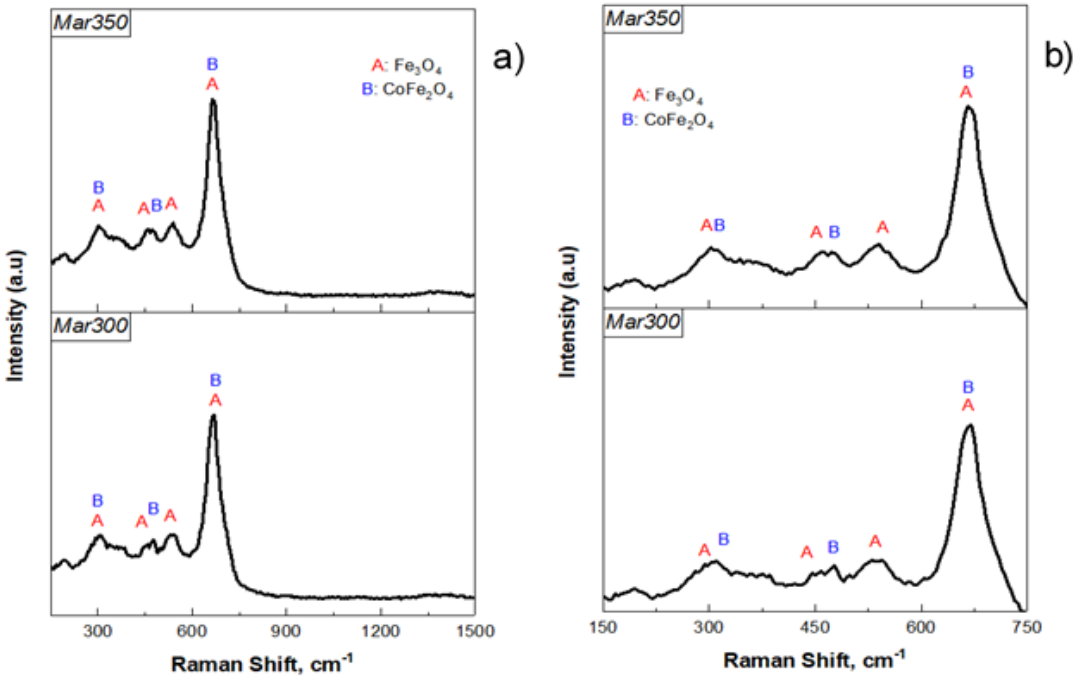

Source: Author (2021).

Figure 56 shows the survey and the high-resolution C 1*s* (b), O 1*s* (c), Fe 2*p* (d) core-level XPS spectra of the oxide produced on maraging steel 300 before and after sputtering for 5 min with Ar^+ plasma. In the survey XPS shown in Figure 56a, it is possible to see the signals of the elements iron (Fe 2*p*), carbon (C 1*s*), cobalt (Co 2*p*), and oxygen (O 1*s*). After etching, the intensity of the C 1*s* signal decreased and the intensities of the other elements signal increased. Tables 28 and 29 include the binding energy values (in eV) of the studied signals and the surface chemical composition (in atomic concentration %), respectively. The C 1*s* core-level spectrum can be decomposed into two contributions in Fig 56b (see Table 28). The main contribution at 284.8 eV is assigned

to adventitious carbon, while the other contribution at 285.7 eV is derived from the presence of C-O bonds (BARRECA *et al.*, 2001; CERRA FLOREZ *et al.*, 2021; KASPAR *et al.*, 2019). After etching 5 min, there are only two contributions at 284.8 and 285.9 eV, and the surface concentration of C decreased from 48.1 % to 1.6 % (see Table 29), being indicative, as expected, of adventitious contamination which is very common on the surface of metals. The assignment of the oxygen species in the O 1*s* signal is not easy. The O 1*s* signal in Fig 56c, can be decomposed into three contributions at 529.9, 531.2 and 532.2 eV. The first one, denoted as Oα, can be related to the presence of surface lattice oxygen (O^{2-}), whereas the contribution at 531.2 eV, denoted as Oβ, is assigned to the presence of defect oxide or to surface low coordination oxygen ion. The third contribution mainly proceeds from hydroxyl groups and C-O groups. After etching 5 min, the relative intensity of the contribution due to lattice oxygen increased. In fact, the oxygen surface content slightly increased after etching from 36.3 to 45.1 % (see Table 29) (BARR, 1978; CERRA FLOREZ *et al.*, 2021; GALTAYRIES *et al.*, 1998).

The Fe 2*p* core-level spectra of the oxide produced on maraging 300 before and after etching 5 min with Ar^+ are shown in Figure 56d, where the deconvolution of the Fe $2p_{3/2}$ signal is also included, and the corresponding values of the different contributions are shown in Table 28. It is well known that the position of the contributions of the Fe $2p_{3/2}$ signal, as well as its satellite peak, are very sensitive to the oxidation state of iron (CERRA FLOREZ *et al.*, 2021; GROSVENOR *et al.*, 2004; LIN; SESHADRI; KELBER, 1997; SANCHIS *et al.*, 2018). It is clear that, the etching process modifies the Fe 2*p* signal. Upon etching, the intensity of the signal increased and the surface iron content went from 10.4 to 35.4 % in atomic concentration (see Table 29). The deconvolution of the Fe $2p_{3/2}$ main peak is also shown in Figure 56e. This peak is deconvoluted in three contributions at 708.1-709.8 eV assigned to Fe^{2+}, 710.3-711.3 eV assigned to Fe^{3+} and 712.1-712.7 eV related to an interaction of Fe^{2+} and Fe^{3+} (LU *et al.*, 2007). The decrease in the $Fe^{2+}/(Fe^{2+} + Fe^{3+})$ ratio after etching can be associated with a greater amount of magnetite in the most external areas. Fe_3O_4 contains the iron ions Fe^{2+} and Fe^{3+}. While the increase in the Fe^{3+} ratio after etching (see Table 28) and the consequent decrease in the Fe^{2+} ratio, would indicate the formation of another type of spinel ferrites, as the cobalt ferrite ($CoFe_2O_4$), this valuation is consistent with the highest amount of cobalt after etching (see Table 29), remembering that in this compound iron and cobalt ions have the oxidation states Fe^{3+} and Co^{2+}, respectively. It is also important to mention that the Fe/Co

atomic ratio is 35.4/17.9 = 1.99, very close to the theoretical value for the cobalt spinel $CoFe_2O_4$ (FANTAUZZI *et al.*, 2019; JI *et al.*, 2004; YAN *et al.*, 2015; 2016; ZHAO *et al.*, 2019; ZHANG *et al.*, 2019). All these results agree with the literature (BLIEM *et al.*, 2015; CERRA FLORES *et al.*, 2021; DĄBROWA *et al.*, 2018; GENUZIO *et al.*, 2016; PARDAVI-HORVATH, 2000; RODRIGUES *et al.*, 2015; TSUKIMURA; SASAKI; KIMIZUKA, 1997), where the diffusion of Co and Ni ions, in the form of Co^{2+} and Ni^{2+} species, from the metallic matrix to the outside is explained.

The Co 2*p* core level spectra (not shown) are very complex. The Co 2*p* spectrum before etching shows a maximum at 784.0 eV assigned to Co^{2+}, but this assignation was difficult because the presence of Co^{3+} species cannot be ruled out. Upon etching, two maxima are observed at 780.7 and 786.0 eV. The new contribution at low binding energy is assigned to reduced Co species (FANTAUZZI *et al.*, 2019; JI *et al.*, 2004; YAN *et al.*, 2015; 2016; ZHAO *et al.*, 2019).

Figure 57 shows the survey spectra and the high-resolution C 1*s* (b), O 1*s* (c), Fe 2*p* (d) core level XPS spectra of the oxide produced on maraging steel 350, before and after sputtering for 5 min with Ar^+ plasma. In the survey shown in Figure 57a, the signals of iron (Fe 2*p*), carbon (C 1*s*), cobalt (Co 2*p*), and oxygen (O 1*s*) are discerned. After etching, the intensity of the adventitious carbon signal decreased and as expected, the relative intensities of the other studied elements increased. Tables 28 and 29 show the binding energy values (in eV) of the studied signals and the surface chemical composition, respectively. The C 1*s* high resolution spectra were similar to that observed in the case of the oxide produced on maraging 300. The C 1*s* core-level spectrum was decomposed into two contributions in Fig 57b. (see Table 28). The O 1*s* core level spectra also show three contributions (Figure 57c, Table 28) at 529.9, 531.1 and 532.0 eV, but in this case the surface content of O 1*s* core-level is higher compared to that observed for grade 300. The Fe 2*p* core-level spectra for the oxide produced on maraging 350 is shown in Fig 57d, where the difference between both core level intensities (before and after etched) is appreciable, being lower than for grade 300. However, iron content increased upon etching, from 11.5 to 31.6 % (see Table 29). The Fe 2p core-level spectra for the etched oxide produced on maraging steel 350 is different, with a much lower relative intensity of the contribution at 708.0 eV assigned to Fe^{2+}. This fact points out that before etching this sample presented a high concentration of the iron spinel Fe_3O_4, with higher concentration of Fe^{2+}. After etching the $Fe^{2+}/(Fe^{2+} + Fe^{3+})$ ratio decreased to 14 and,

taking in account the fact of the Fe/Co atomic ratio is 36.64/18.14 = 2.07, value very near to the theoretical for the cobalt spinel $CoFe_2O_4$ (formed by the metal ions Fe^{3+} and Co^{2+}), and that in the innermost areas of the oxide there is a greater concentration of cobalt (see Table 29), it is feasible to have a greater quantity of the cobalt spinel $CoFe_2O_4$.

The Co 2*p* core spectrum after etching shows two maxima at 780.7 and 782.7 eV, with a difficult assignation, but indicate the presence of Co^{2+} and Co^{3+}. The possible formation of a cobalt spinel Co_3O_4 cannot be discarded, together to the presence of the spinel $CoFe_2O_4$.

Figure 56 – XPS spectra of the oxide formed on maraging steel 300 before (As received) and after etching 5 min with Ar^+ plasma (Etched 5 min Ar^+). a) survey spectrum, b) C 1*s*, c) O 1*s*, d) Fe 2*p* and e) Fe $2p_{3/2}$ deconvoluted

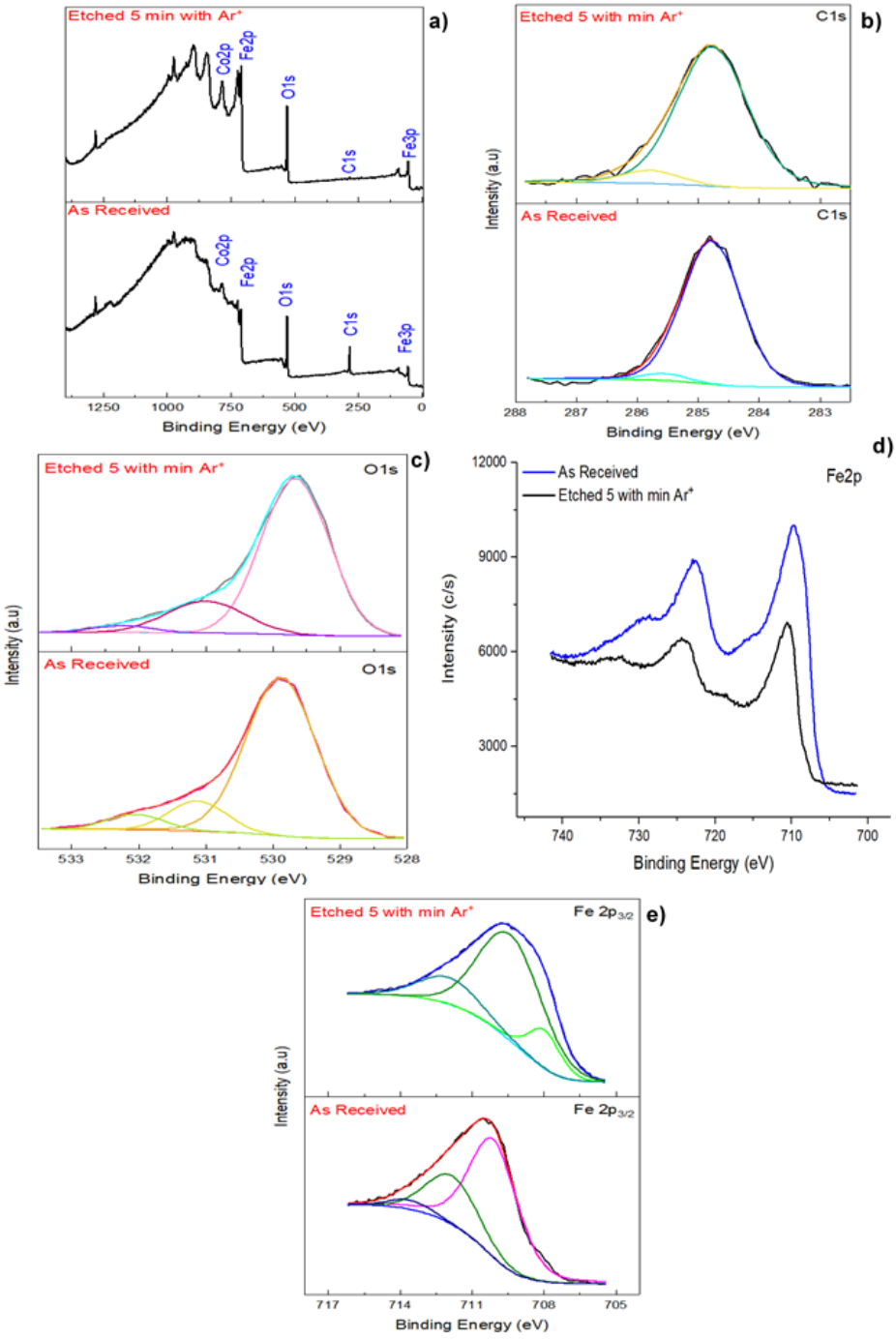

Source: Author (2021).

Figure 57 – XPS spectra of the oxide formed on maraging steel 350 before (As received) and after etching 5 min with Ar^+ plasma (Etched 5 min Ar^+). a) survey spectrum, b) C 1*s*, c) O 1*s*, d) Fe 2*p* and e) Fe 2$p_{3/2}$ deconvoluted

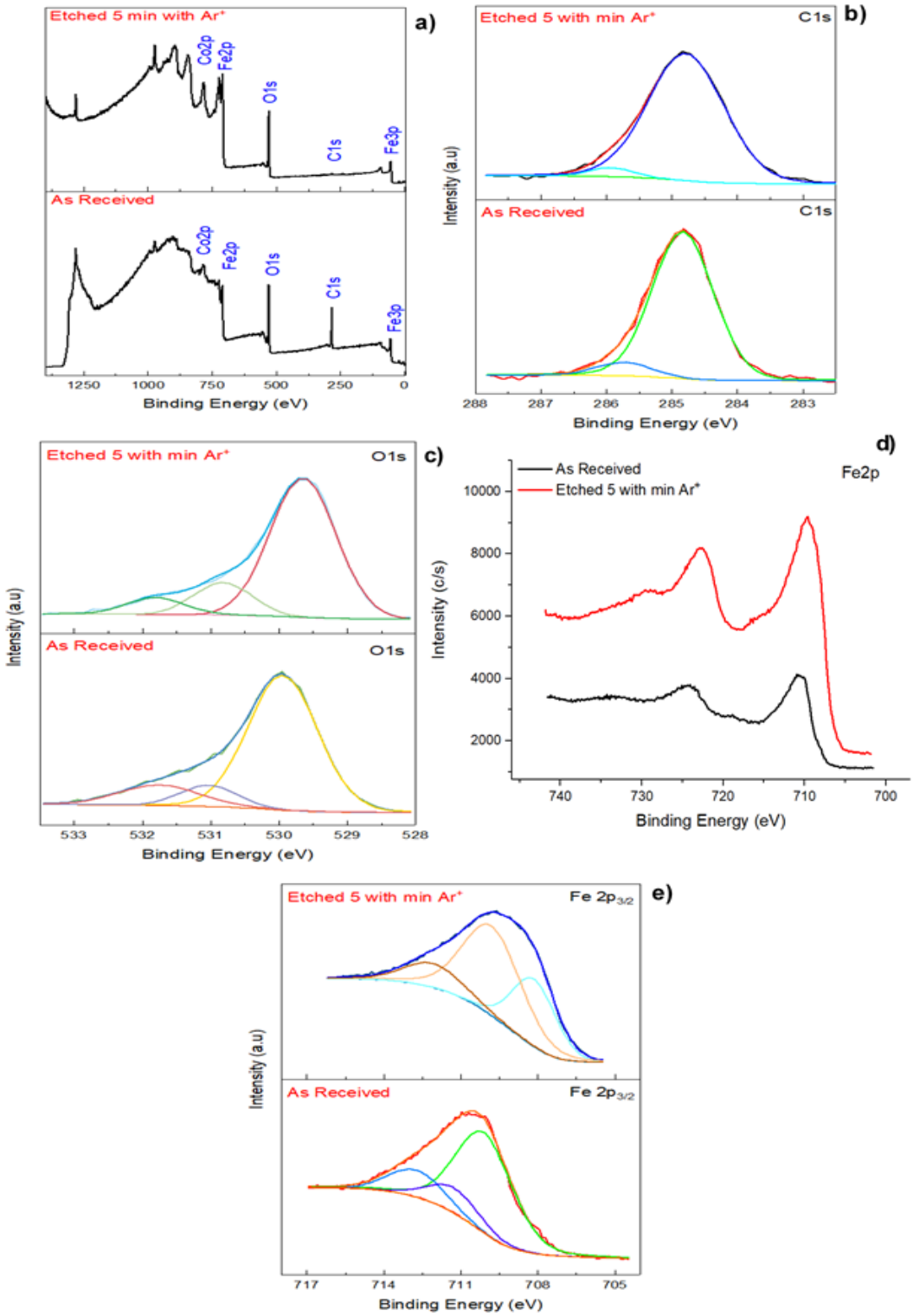

Source: Author (2021).

Table 28 – Binding energy values (in eV) of the studied elements and percentages of relative area in brackets and $Fe^{2+}/(Fe^{2+}+Fe^{3+})$ ratios for the studied oxide produced on maraging steels before and after etching 5 min with Ar^+ plasma

Sample	C 1*s*	O 1*s*	Fe 2$p_{3/2}$	Co 2$p_{3/2}$	$Fe^{2+}/(Fe^{2+}+Fe^{3+})$
Mar300	284.8 (92) 285.7 (8)	529.9 (76) 531.0 (10) 531.8 (14)	709.8 (68) 711.3 (15) 712.7 (17)	784.0	68
Mar300 after 5 min Ar^+	284.8 (96) 285.9 (4)	529.6 (76) 530.8 (15) 531.8 (9)	708.1 (29) 710.3 (56) 712.1 (15)	780.7 786.0	29
Mar350	284.8 (96) 285.6 (4)	529.9 (80) 531.1 (12) 532.0 (8)	710.1 (68) 711.8 (28) 713.6 (4)	784.2	68
Ma350 after 5 min Ar^+	284.8 (93) 285.8 (7)	529.7 (78) 531.0 (18) 532.2 (3)	708.0 (14) 709.4 (68) 712.4 (25)	782.6 788.4	14

Source: Author (2021).

Table 29 – Surface chemical composition (in at. %) for the studied oxide produced on grade 300 and 350 maraging steels before and after etching 5 min with Ar^+ plasma

Sample	C	O	Fe	Co
Mar300	48.1	36.3	10.4	5.3
Mar300 after 5 min Ar^+	1.6	45.1	35.4	17.8
Mar350	42.6	38.6	11.5	7.6
Mar350 after 5 min Ar+	3.9	49.3	31.6	15.2

Source: Author (2021).

In order to determine the adhesive damage between the former oxide layer and the different metallic maraging alloy substrates, also denoted as Pc_2 (ASTM, 2015c; CERRA FLOREZ *et al.*, 2021; GHASEMI PARIZI *et al.*, 2020), the scratch tests were conducted at the submicrometric length scale in order to confine the deformation stress field at the coating/substrate interface. Figure 58 (left hand side) shows the whole scratch track for both investigated systems in order to qualitative observe the induced damage along the sliding track. Figure 58 (right hand side) shows top-view SEM micrograph of nanoscratch tracks, where some interesting features are clearly visible – mainly, cracks at the edge of the sliding track and subsequently chipping of the former oxide layer. The Pc2 directly determined from the SEM micrographs are summarized in Table 30. From Figure 58 and the Pc2 summarized in Table 30, it is clearly visible that the oxide layer grown on the maraging 300 alloy required a higher sliding force in order to detach the oxide layer growth under N_2 atmosphere from the metallic maraging substrate. However, both oxide films present good adherence, and the results shows the capability for being

used for tribological applications under sliding contact tests (CERRA FLOREZ *et al.*, 2021; GHASEMI PARIZI *et al.*, 2020).

Figure 58 – (a) Scanning electron microscope (SEM) micrograph for the nanoscratch track and (b) magnification of the top-view SEM micrographs of nanoscratch tracks where the first adhesive damage appears

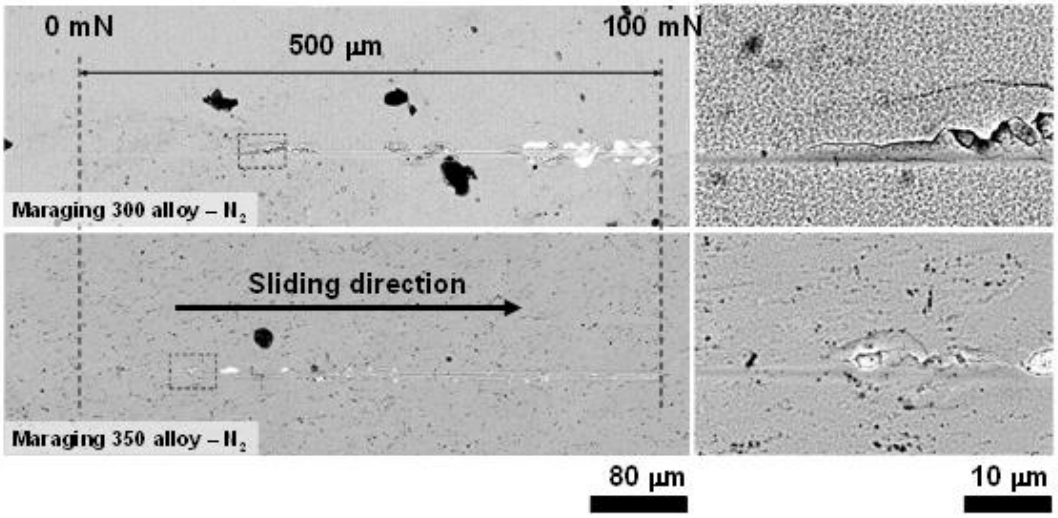

Source: Author (2021).

Table 30 – Pc2 was directly determined from the scanning electron microscope (SEM) micrographs for each oxide produced on each maraging steel

Steel where the oxide was formed	Pc2 (mN)
Mar300	32
Mar350	16

Source: Author (2021).

The above results show several similarities between the oxides produced in both steels. They have the same superficial defects, although the oxide on grade 300 is slightly rougher than that of the 350 maraging steel. These differences may not be associated to the chemical composition of the oxide (similar for both), not to the previous sample roughness (the same for both).

Molybdenum (MoO_3) and titanium (TiO_2) oxides were found in the internal layers of the oxide, with higher quantities in the innermost part of the film. For this reason, they were not detected by RAMAN spectroscopy and XPS. These results are according to the works (CERRA FLOREZ *et al.*, 2021; KLEIN; YANIV; SHARON, 1983; SUBBARAMAN; DESHMUKH; SANKARANARAYANAN, 2013; SURMAN, 1973) that explain how this type of compounds are formed in the initial stages of the oxidation

process and are only found in the inner parts of the oxide because iron oxides, who have greater growth kinetics, cover molybdenum and titanium oxides.

Thermodynamic and kinetic stability conditions allow the iron oxide Fe_3O_4 to be formed during the growth process of the oxide layer, as commented in Klein, Sharon and Yaniv (1981), Klein, Yaniv and Sharon (1981; 1983), Greyling, Kotzi and Viljoen (1990), Rezek, Klein and Yahalom (1997), Luo and Shenz (2008), Surman (1973), Subbaraman, Deshmukh and Sankaranarayanan (2013) and Jeon *et al.* (2013). However, from these same conditions, elements such as cobalt and nickel can also diffuse within the oxide. Klein, Yaniv and Sharon (1981) and Klein, Sharon and Yaniv (1981; 1983) mentioned that it is possible to find these elements within the iron spinel in a substitutionary way but not as another compound. In this work, as well as in Cerra Florez *et al.* (2021), it has been observed that these elements form a mixture of spinels: $CoFe_2O_4$, $NiFe_2O_4$ and Fe_3O_4. The formation of this spinel mixture is possible by the diffusion reaction of Co^{2+} and Ni^{2+} from the metallic matrix to the outside of the oxide. Then, the diffusion of these ions replaces Fe^{2+} ions in the octahedral sites of spinel and to the external part of the film, where they form Fe_3O_4. In the present case, the high cobalt content of maraging steels, and also the formation of nickel-rich austenite in the oxide layer/metal interface (due to the decomposition of martensite at temperatures near 500 ºC) influence the preferential formation of the cobalt ferrite spinel (BLIEM *et al.*, 2015; CERRA FLOREZ *et al.*, 2021; DĄBROWA *et al.*, 2018; GENUZIO *et al.*, 2016; PARDAVI-HORVATH, 2000; RODRIGUES *et al.*, 2015; SILVA *et al.*, 2019; TSUKIMURA; SASAKI; KIMIZUKA, 1997).

It is possible that in the innermost layers, where there is more nickel, spinel $NiFe_2O_4$ was formed, but it was not detected in the upper layers. Also the gradient of composition of cobalt observed in the results of EDS and XPS, where a greater quantity is observed in the innermost layers, confirms that the spinel $CoFe_2O_4$ has a bigger amount in the internal regions of the oxide.

The conditions of time and temperature in the present procedure, as well as the steps using nitrogen (without available oxygen) and focusing on the oxidation process taking place only with steam, allowed the formation of a spinel-like oxide film. Hematite was not found due to oxygen deficit, as indispensable factor for the transformation of $Fe_3O_4 \rightarrow \alpha\text{-}Fe_2O_3$ to occur under the temperature conditions used in this heat treatment (GENUZIO *et al.*, 2014; 2016; GREYLING; KOTZI; VILJOEN, 1990; HONG *et al.*,

2019; JEON *et al.*, 2013; SUBBARAMAN; DESHMUKH; SANKARANARAYANAN, 2013; ZHANG *et al.*, 2016).

4.5.3 Conclusions

The oxides produced in both maraging steel present the same superficial defects and similar roughness. A chemical composition gradient from the innermost towards to the external surface of the oxide was observed, whit a higher quantity of alloying elements such Ni, Ti, Mo, and Co in the oxide layer/metal interface. Then, due to the nickel gradient composition in the metal/oxide interphase, the formation of nickel-rich austenite was possible in the steel, and the formation in a great quantity of the nickel spinel ferrite $NiFe_2O_4$ next to this region cannot be discarded.

Another implication of the chemical composition gradient is the formation of Molybdenum (MoO_3) and Titanium (TiO_2) oxides in the internal layers of the oxide. These compounds are formed in the initial stages of the oxidation process and are only found in the inner parts of the oxide because iron oxides, which have greater growth kinetics, cover molybdenum and titanium oxides.

The thermodynamic and kinetic conditions of the heat treatment here investigated allowed the formation of the iron ferrite spinel Fe_3O_4, and the consequent formation of the spinel mix $NiFe_2O_4$, $CoFe_2O_4$ and Fe_3O_4, by the diffusion reaction of cobalt and nickel ions (Co^{2+} and Ni^{2+}) from the metallic matrix to the outside of the oxide, replacing of Fe^{2+} ions in the octahedral sites of spinel and displacing part of this iron ions to the external part of the film, where they form Fe_3O_4.

Moreover, the conditions of the heat treatment, specifically the nitrogen atmosphere at the first stage (without available oxygen), allowed the formation of a spinel-like oxide film and avoid the formation of hematite oxide.

In both steels, the oxide produced had a relatively similar thickness, with the same defects, such as porosity, metal-oxide interface and irregular outer surface. It was also possible to observe in both steels the austenitic phase rich in nickel and cobalt detected by XRD and that was formed during the oxidation process at the base of the steels.

The maraging 300 steel presents a good adherence between the formed oxide layer and the metallic substrate growth under the N_2 atmosphere. However, both oxide

films demonstrate good adherence, and its capability for being used under aggressive conditions mainly for tribological applications under sliding contact tests.

5 CONCLUDING REMARKS

In this work, the influence of chemical composition and heat treatments on microstructure, mechanical behavior and corrosion were performed for two maraging steels. It has been confirmed that the combination of the martensitic microstructure (more ductile) with the nanometric intermetallic compounds, formed during the aging heat treatment, dispersed in the metal matrix produces an exponential increase of the maraging steels mechanical properties.

The electrochemical behavior showed the low corrosion resistance of maraging steels in HF solution; even the studied solution annealed condition had no formation of passive films. The formation of the intermetallic compounds on the aged conditions produced phase boundaries more reactive to corrosion and a chemical composition differential between the metal matrix and the nanometric compounds (and austenitic phase in the case of the formation) that generated galvanic effect, decreasing their corrosion resistance.

The oxidation treatment using nitrogen atmosphere to heat up to 500°C for 60 min, allowed to understand the oxidation behavior of grade 300 maraging steel. It was produced an oxide film with different heterogeneities, especially on the surface. This study showed the influence of the steel chemical composition on the formation and composition of the oxide film and revealed the dominion of the iron ions kinetic in the production of a chemical composition profile with more amounts of alloy elements in the inner part of the film. An austenitic nickel-rich phase was detected, observed for the first time in their site on the metal-oxide interphase, and, at last, it was known the oxidation influence on their formation and localization. The composition of the oxide film was also influenced by the kinetic and thermodynamic conditions during the heat treatment, since the oxygen availability allowed the overoxidation and the consequent transformation of a spinel part into hematite; and the diffusion of cobalt/nickel ions through magnetite replacing the iron located in the octahedral sites of the spinel's structure and transforming part of the magnetite into $CoFe_2O_4$ and $NiFe_2O_4$. Finally, the adherence between the formed oxide layer and the metallic substrate was evaluated and demonstrated its capability for being used under aggressive conditions, mainly for tribological applications under sliding contact tests.

The heat treatment procedure used with the four variations in the atmospheres (Air or N_2 or O_2 or CO_2, with steam and N_2) and applied to the grade 300 and 350 maraging steels produced heterogeneous oxide layers, with the presence of several defects spread on all their surfaces, such as holes, cracks, and porosity.

The differences in terms of roughness and thickness of all the samples do not indicate any relationship with the steel's chemical composition of the different investigated alloys. Therefore, it depends on the oxygen availability in the atmosphere used. As observed, less roughness and lower thickness were found on the samples treated with the N_2/steam/N_2 oxidation process (with less oxygen available).

In all the samples, the same production of a chemical composition profile was observed (more amounts of alloy elements in the innermost part of the oxide), and also the austenitic nickel-rich phase was detected and observed on the metal-oxide interphase localization.

Variations in the phases (and their amounts) that form the oxides were found depending on the gases used in the thermal treatments. Thus, the atmospheres with a higher amount of oxygen (synthetic air, O_2, and CO_2) had the transformation of part of the spinel into hematite in the oxide surface, and its quantity decreased in the case of the CO_2 treatment (with less available oxygen), until it was not found in the nitrogen oxidation treatment.

In all the samples were found molybdenum (MoO_3) and titanium (TiO_2) oxides in the internal layers of the oxide. These compounds are formed in the initial stages of the oxidation process and are covered by the iron/cobalt/nickel oxides, and the higher quantity of these oxides was found on the grade 350 maraging steels due to their chemical composition (with more Mo and Ti) and the more intermetallic precipitates (rich in Mo and Ti).

The thermodynamic and kinetic conditions of the heat treatments with synthetic air, O_2 and N_2 allowed the formation of the iron ferrite spinel Fe_3O_4 and the consequent formation of the spinel mix $NiFe_2O_4$, $CoFe_2O_4$ and Fe_3O_4 by the diffusion reaction of cobalt and nickel ions (Co^{2+} and Ni^{2+}) from the metallic matrix to the outside of the oxide, replacing Fe^{2+} ions in the octahedral sites of spinel and displacing part of these iron ions to the external part of the film, where they form Fe_3O_4. The particularity (kinetic and thermodynamic) of the CO_2 treatment only left the formation of the $CoFe_2O_4$. About the spinel quantity, the higher amount was found in the samples treated with N_2,

followed by the treated with CO_2. Coincidently, these results are associated with less oxygen availability.

Finally, the adherence between the oxide layer and the metallic substrate of the oxides films produced using air and N_2 (in both maraging steels) and CO_2 atmospheres (in the grade 350 maraging steel) presents excellent results and demonstrates their capability for being used under aggressive conditions, mainly for tribological applications under sliding contact tests. No relationship was found between the chemical composition, the thickness, the number of phases, and the adhesion of the oxide film that would explain the low Pc2 of the samples treated with O_2 (both steels) and CO_2 (maraging 300). This phenomenon is probably due to the combination of a greater amount of surface defects (roughness) and sub-surface defects (cracks and bubbles) that can affect the measurement, but bring a decrease in film cohesion and, consequently, the low adhesion of these oxides.

6 SUGGESTIONS FOR FUTURE WORKS

An innovative study involving X-ray photoelectron spectroscopy (XPS) is suggested as future work, specifically the performance of the maraging steel oxidation process with the procedure developed in the present work, using the near-ambient pressure X-ray photoelectron spectroscopy (NAP-XPS) technique, that provides direct measurements of the gaseous environment influence on the surface of materials in different temperatures, in order to identify the chemical state, the surface restructuring of materials that critically undergo changes during the oxidation process, and the formation of the oxide films. NAP-XPS systems do not require ultra-high vacuum conditions in the analysis area, and the equipment localized at the Barcelona Research Center in Multiscale Science and Engineering (Universitat Politècnica de Catalunya) can analyze samples heating up to 700 ºC (BARCELONA RESEARCH CENTER IN MULTISCALE SCIENCE AND ENGINEERING, 2021).

It is important to note that the electrochemical tests (open potential circuit, linear polarization, and electrochemical impedance spectroscopy) to assess the corrosion resistance in hydrofluoric acid (HF) solution of the oxides produced under the conditions described in this work (steels and atmospheres) were not mentioned as suggested works since, at the moment, the essays are being carried out in the master's research of a Materials Science and Engineering postgraduate program student at the Universidade Federal do Ceará. The results of this work will be compared with the outcomes shown in subchapter 4.1.

REFERENCES

ABDULLAH, S. A.; SAHDAN, M. Z.; NAYAN, N.; EMBONG, Z.; CHE HAK, C. R.; ADRIYANTO, F. Neutron beam interaction with rutile TiO_2 single crystal (1 1 1): Raman and XPS study on Ti^{3+}-oxygen vacancy formation. **Materials Letters**, v. 263, p. 127143, Mar. 2020.

ALMODÓVAR, P. LÓPEZ, M. L. RAMÍREZ-CASTELLANOS, J. NAPPINI, S. MAGNANO, E. GONZÁLEZ-CALBET, J. M. DÍAZ-GUERRA, C. Synthesis, characterization and electrochemical assessment of hexagonal molybdenum trioxide (h-MoO_3) micro-composites with graphite, graphene and graphene oxide for lithium-ion batteries. **Electrochimica Acta**, v. 365, p. 137355, Jan. 2021.

ASTM. American Society for Testing and Materials. **Annual Book of ASTM Standards**: ASTM E112-96 e2 – Standard Test Methods for Determining Average Grain Size. West Conshohocken, PA: ASTM International, 2015a.

ASTM. American Society for Testing and Materials. **Annual Book of ASTM Standards**: ASTM E18-03 – Standard Test Methods for Rockwell Hardness and Rockwell Superficial Hardness of Metallic Materials. West Conshohocken, PA: ASTM International, 2015b.

ASTM. American Society for Testing and Materials. **Annual Book of ASTM Standards**: ASTM C1624 – Standard Test Method for Adhesion Strength and Mechanical Failure Modes of Ceramic Coatings by Quantitative Single Point Scratch Testing. West Conshohocken, PA: ASTM International, 2015c.

AVELINO, A. F.; ARAÚJO, W. S.; DIAS, D. F.; DOS SANTOS, L. P.; CORREIA, A. N.; LIMA-NETO, P. Corrosion investigation of the 18Ni 300 grade maraging steel in aqueous chloride medium containing H_2S and CO_2. **Electrochimica Acta**, 286, 339-349, 2018.

BARCELONA RESEARCH CENTER IN MULTISCALE SCIENCE AND ENGINEERING. Near-ambient pressure X-ray photoelectron spectroscopy. Universitat Politècnica de Catalunya. Barcelona, 2021. Available at: https://multiscale.upc.edu/en/infrastructure/nap-xps. Access on: 16 March 2021.

BARRECA, D.; BATTISTON, G.A.; BERTO, D.; GERBASI, R.; TONDELLO, E. Chemical vapor deposited Fe_2O_3 thin films analyzed by XPS. **Surface Science Spectra**, v. 8, p. 240, 2001.

BARR, T. L. An ESCA study of the termination of the passivation of elemental metals. **The Journal of Physical Chemistry A**, v. 82, i. 16, p. 1801-1810, 1 Aug. 1978.

BARZASHKA, I.; OELRICH, I. Engineering Considerations for Gas Centrifuges. **Federation of American Scientists**, [*s.d.*].

BELLANGER, G.; ROMEAU, J. J. Effect of slightly acid pH with or without chloride in radioactive water on the corrosion of maraging steel. **Journal of Nuclear Materials**, v. 28, i. 1, p. 24-37, Feb. 1996.

BLIEM, R.; PAVELEC, J.; GAMBA, O.; MCDERMOTT, E.; WANG, Z.; GERHOLD, S.; BLAHA, P. Adsorption and incorporation of transition metals at the magnetite Fe_3O_4 (001). **Physical Review B**, v. 92, p. 75440, 26 Aug. 2015.

BRADHURST, D. B.; HEUER, P. M. Environmental Cracking of High Strength Maraging Steels: Part 2 – Gaseous Fluoride Atmospheres. **Corrosion**, v. 37, i. 2, p. 63-70, 1981.

CAPURRO, C. CICUTTI, C. Analysis of titanium nitrides precipitated during medium carbon steels solidification.
Journal of Materials Research and Technology, v. 7, i. 3, p. 342-349, 2018.

CARLOS, A. O enriquecimento de urânio e seu uso. **Energia nuclear**, 18 Mar. 2011. Available at: http://enbrasilbr.blogspot.com/2011/03/o-enriquecimento-de-uranio.html. Access on: 23 March 2020.

CERRA FLOREZ, M. A.; FARGAS RIBAS, G.; ROVIRA, J. J. R.; VILARRASA-GARCÍA, E.; RODRÍGUEZ-CASTELLÓN, E.; SOUSA, A. B. F.; CARDOSO, J. L.; GOMES DA SILVA, M. J. Characterization Study of an Oxide Film Layer Produced under CO_2/Steam Atmospheres on Two Different Maraging Steel Grades. **Metals**, v. 11, i. 5, p. 746, 1 May 2021.

CERRA FLOREZ, M. A.; PEREIRA, U. C.; CARDOSO, J. L.; OLIVEIRA, F. J. S.; ARAÚJO, W. S.; RIBAS, G. F.; DE ABREU, H. F. G.; DA SILVA, M. J. G. Microstructural characterization of grade 300 and grade 350 maraging steels and electrochemical study in hydrofluoric solution. **Journal of Fluorine Chemistry**, v. 243, p. 109738, 2021.

CERRA FLOREZ, M. A.; RIBAS, G. F.; CARDOSO, J. L.; MATEO GARCÍA, A. M.; ROA ROVIRA, J. J.; BASTOS-NETO, M.; DE ABREU, H. F. G.; GOMES DA SILVA, M. J. Oxidation Behavior of Maraging 300 Alloy Exposed to Nitrogen/Water Vapor Atmosphere at 500 °C. **Metals**, v. 11, i. 7, p. 1021, 28 May 2021.

CONDE, F. F.; ESCOBAR, J. D.; OLIVEIRA, J. P.; BÉREŠ, M.; JARDINI, A. L.; BOSE, W. W.; AVILA, J. A. Effect of thermal cycling and aging stages on the microstructure and bending strength of a selective laser melted 300-grade maraging steel. **Materials Science & Engineering A**, v. 758, p. 192-201, 2019.

CHINN, S. R.; ZEIGER, H. J. Electronic Raman scattering in FeF_2. *In*: AMERICAN INSTITUTE OF PHYSICS CONFERENCE, 5., Chicago, USA, 1971. **Proceedings** […]. Chicago, USA: AIF, 1971. Available at: https://doi.org/10.1063/1.3699453. Access on: 22 May 2019.

CHUNG, F. Quantitative Interpretation of X-ray Diffraction Patterns of Mixtures: I – Matrix-Flushing Method for Quantitative Multicomponent Analysis. **Journal of Applied Crystallography**, v. 7, p. 519-525, 1974.

CRUM, J. R.; SMITH, G. D.; MCNALLAN, M. J.; HIRNYJ, S. Characterization of Corrosion Resistant Materials in Low and High Temperature HF Environments. *In*: CORROSION '99, NACE INTERNATIONAL CONFERENCE, 382., 25 Apr. 1999, San Antonio, USA. **Proceedings** […]. San Antonio: OnePetro, 1999. Available at: https://onepetro.org/NACECORR/proceedings-abstract/CORR99/All-CORR99/NACE-99382/128402. Access on: 19 May 2019.

DĄBROWA, J.; STYGAR, M.; MIKUŁA, A.; KNAPIK, A.; MROCZKA, K.; TEJCHMAN, W.; MARTIN, M. Synthesis and microstructure of the $(Co,Cr,Fe,Mn,Ni)_3O_4$ high entropy oxide characterized by spinel structure. **Materials Letters**, v. 216, p. 32-36, 2018.

DAI, H.; SHI, S.; GUO, C.; CHEN, X. Pits formation and stress corrosion cracking behavior of Q345R in hydrofluoric acid. **Corrosion Science**, v. 166, p. 108443, 15 Apr. 2020.

DA SILVA, F. **Síntese e caracterização de óxidos ternários de Ni-Co-Mn com estrutura espinélio**. 2016. Master thesis (Mestrado em Engenharia e Ciência de Materiais) – Universidade Federal do Ceará, 2016. Available at: http://www.repositorio.ufc.br/handle/riufc/18904. Access on: 2 May 2019.

DECKER, R. F. **Source book on maraging steels**: a comprehensive collection of outstanding articles from the periodical and reference literature. Decker. Metals Park, Ohio: American Society for Metals, 1979. Available at: https://catalog.hathitrust.org/Record/000301554?type%5B%5D=all&lookfor%5B%5D=Decker%2C%20Raymond%20Frank.&ft=. Access on: 18 March 2020.

DE FARIA, D. L. A.; LOPES, F. N. Heated goethite and natural hematite: Can Raman spectroscopy be used to differentiate them? **Vibrational Spectroscopy**, v. 45, i. 2, p. 117-121, Nov. 2007.

DE LA FIGUERA, J.; QUESADA, A.; MARTÍN-GARCÍA, L.; SANZ, M.; OUJJA, M.; REBOLLAR, E.; CASTILLEJO, M.; PRIETO, P.; MUÑOZ-MARTÍN, A.; ABALLE, L.; MARCO, J. F. Self-organized single crystal mixed magnetite/cobalt ferrite films grown by infrared pulsed-laser deposition. **Applied Surface Science**, v. 359, p. 480-485, 30 Dec. 2015.

DESCOTES, V.; MIGOT, S.; ROBAUT, F.; BELLOT, J.P.; PERRIN-GUÉRIN, V.; WITZKE, S.; JARDY, A. TEM Characterization of a Titanium Nitride (TiN) Inclusion in a Fe-Ni-Co Maraging Steel. **Metallurgical and Materials Transactions A**, v. 46A, p. 2793, 2015.

DESCOTES, V.; QUATRAVAUX, T.; BELLOT, J.P; WITZKE, S.; JARDY, A. Titanium Nitride (TiN) Germination and Growth during Vacuum Arc Remelting of a Maraging Steel. **Metals**, v. 10, i. 4, p. 541, 22 Apr. 2020.

DING, M.; CHEN, W.; XU, H.; SHEN, Z.; LIN, T.; HU, K.; HUI LU, C.; XIE, Z. Novel α-Fe_2O_3/MXene nanocomposite as heterogeneous activator of peroxymonosulfate for the degradation of salicylic acid. **Journal of Hazardous Materials**, v. 382, p. 121064, 15 Jan. 2020.

DINIZ, V.; DANTAS, B.; FIGUEIREDO, A.; CORNEJO, D.; COSTA, A. Avaliação microestrutural e magnética de Fe_3O_4 sintetizada pelo método de reação de combustão. **Cerâmica**, v. 61, p. 298-302, 2015.

DONG, W. P.; SULLIVAN, P. J.; STOUT, K. J. Comprehensive study of parameters for characterizing three-dimensional surface topography: III – Parameters for characterizing amplitude and some functional properties. **Wear**, v. 178, i. 1-2, p. 29-43, 1994a.

DONG, W. P.; SULLIVAN, P. J.; STOUT, K. J. Comprehensive study of parameters for characterizing three-dimensional surface topography: IV – Parameters for characterizing spatial and hybrid properties. **Wear**, v. 178, i. 1-2, p. 45-60, 1994b.

DUDZIAK, T.; BORON, L.; DEODESHMUKH, V.; SOBCZAK, J.; SOBCZAK, N.; WITKOWSKA, M.; RATUSZEK, W.; CHRUSCIEL, K. Steam Oxidation Behavior of Advanced Steels and Ni-Based Alloys at 800ºC. **Journal of Materials Engineering and Performance**, v. 26, p. 1044-1056, 2017.

EL-MAHDY, G. A.; HEGAZY, M. M.; F-EL-TAIB H.; MAHMOUD, H. E.; FATHY, A. M.; SAYED, F. M. Electrochemical Behavior of Maraging Steel in Chloride Containing Environment. **International Journal of Electrochemical Science**, v. 8, p. 2816-2825, 2013.

ENTENDA como funciona a energia nuclear. **Agência Câmara**, Brasília, DF, 3 Mar. 2005. Available at: https://www2.camara.leg.br/agencia/noticias/62053.html. Access on: 22 March 2020.

FANTAUZZI, M.; SECCI, F.; ANGOTZI, M. S.; PASSIU, C.; CANNAS, C.; ROSSI, A. Nanostructured spinel cobalt ferrites: Fe and Co chemical state, cation distribution and size effects by X-ray photoelectron spectroscopy. **RSC Advances**, v. 9, i. 33, p. 19171-19179, 2019.

FARZI-KAHKESH, S.; FATTAH, A.; BAGHER RAHMANI, M. Synthesis and optimum temperature determination of highly sensitive MoO_3-based heterojunction Schottky sensor for hydrogen detection. **Microelectronic Engineering**, v. 235, p. 111453, 15 Jan. 2021.

FLAMANT, Q.; GARCÍA, F. M.; ROA, J. J.; ANGLADA, M. Hydrofluoric acid etching of dental zirconia: Part 1 – etching mechanism and surface characterization. **Journal of the European Ceramic Society**, v. 36, i. 1, p. 121-134, 2016.

FLOREEN, S. The physical metallurgy of maraging steels. **Metallurgical Reviews**, v. 13, p. 115-128, 1968.

GADELMAWLA, E. S.; KOURA, M. M.; MAKSOUD, T. M. A.; ELEWA, I. M.; SOLIMAN, H. H. Roughness parameters. Journal of Materials Processing Technology, v. 123, i. 1, p. 133-145, 2002.

GALTAYRIES, A.; SPORKEN, R.; RIGA, J.; BLANCHARD, G.; CAUDANO, R. XPS comparative study of ceria/zirconia mixed oxides: Powders and thin film characterization. **Journal of Electron Spectroscopy and Related Phenomena**, v. 88-91, p. 951-956, 1998.

GAO, X.; BI, J.; WANG, W.; LIU, H.; CHEN, Y.; HAO, X.; SUN, X.; LIU, R. Morphology-controllable synthesis of $NiFe_2O_4$ growing on graphene nanosheets as advanced electrode material for high performance supercapacitors. **Journal of Alloys and Compounds**, v. 826, p. 154088, 15 Jun. 2020.

GENTIL, V. **Corrosão**. 6. ed. Rio de Janeiro: LTC, 2012.

GENUZIO, F.; SALA, A.; SCHMIDT, T. H.; MENZEL, D.; FREUND, H. J. Interconversion of α-Fe_2O_3 and Fe_3O_4 Thin Films: Mechanisms, Morphology, and Evidence for Unexpected Substrate Participation. **The Journal of Physical Chemistry C**, v. 118, i. 50, p. 29068-29076, 2014.

GENUZIO, F.; SALA, A.; SCHMIDT, T.; MENZEL, D.; FREUND, H. J. Phase transformations in thin iron oxide films: Spectromicroscopic study of velocity and shape of the reaction fronts. **Surface Science**, v. 648, p. 177-187, Jun. 2016.

GLASER, A. Characteristics of the Gas Centrifuge for Uranium Enrichment and Their Relevance for Nuclear Weapon Proliferation. **Science and Global Security**, v. 16, i. 1-2, p. 1-25, 2008.

GHASEMI PARIZI, M. J.; SHAHVERDI, H.; ROA, J. J.; PIPELZADEH, E.; MARTINEZ, M.; CABOT, A.; GUARDIA, P. Improving Mechanical Properties of Glass Fiber Reinforced Polymers through Silica-Based Surface Nanoengineering. **ACS Applied Polymer Materials**, v. 2, i.7, p. 2667-2675, 2020.

GREYLING, C.; KOTZI, A.; VILJOEN, P. The Kinetics of Oxide Film Growth on Maraging Steel as Described by Space-charge Effects. **Surface and Interface Analysis**, v. 16, i. 1-12, p. 293-298, 1990.

GROSVENOR, A. P.; KOBE, B. A.; BIESINGER, M. C.; MCINTYRE, N. S. Investigation of multiplet splitting of Fe 2*p* XPS spectra and bonding in iron compounds. **Surface and Interface Analysis**, v. 36, i. 12, p. 1564-1574, Dec. 2004.

GUO, R.; DANG, L.; LIU, Z.; LEI, Z. Incorporation of electroactive $NiCo_2S_4$ and Fe_2O_3 into graphene aerogel for high-energy asymmetric supercapacitor. **Colloids and Surfaces A**, v. 602, p. 125110, 5 Oct. 2020.

HOFF, J.T.; GRUNGERG, P.A.; KONINGSTEIN, J.A. Light Scattering from High-Lying Electronic Excitations in CoF_2. **Applied Physics Letters**, v. 20, i. 9, p. 358, 18 Jan. 1972.

HONG, H.; MEMON, N. K.; DONG, Z.; KEAR, B. H.; TSE, D. S. Flame synthesis of gamma-iron-oxide (γ-Fe_2O_3) nanocrystal films and carbon nanotubes on stainless-steel substrates. **Proceedings of the Combustion Institute**, v. 37, i. 1, p. 1249-1256, 2019.

HORCAS, I.; FERNÁNDEZ, R. WSXM: A software for scanning probe microscopy and a tool for nanotechnology. **Review of Scientific Instruments**, v. 78, p. 013705, 2007.

HU, X.; YU, J.C.; GONG, J.; LI, Q.; LI, G. α-Fe_2O_3 Nanorings Prepared by a Microwave-Assisted Hydrothermal Process and Their Sensing Properties. **Advanced Materials**, v. 19, i. 17, p. 2324-2329, Sept. 2007.

ICDD. International Center for Diffraction Data. **JCPDS**: X-ray Diffraction Data Cards of the Joint Committee on Powder Diffraction Standards. Swarthmore, PA, USA: ICDD, 1975.

JI, G. B.; TANG, S. L.; REN, S. K.; ZHANG, F. M.; GU, B. X.; DU, Y. W. Simplified synthesis of single-crystalline magnetic $CoFe_2O_4$ nanorods by a surfactant-assisted hydrothermal process. **Journal of Crystal Growth**, v. 270, i. 1-2, p. 156-161, 15 Sept. 2004.

JEON, B.; VAN OVERMEERE, Q.; VAN DUIN, A. C.; RAMANATHAN, S. Nanoscale oxidation and complex oxide growth on single crystal iron surfaces and external electric field effects. **Physical Chemistry Chemical Physics**, v. 15, i. 6, p. 1821-1830, 2013.

JONES, D. A. **Principles and Prevention of Corrosion**. 2. ed. Prentice Hall, NJ, EUA: Pearson Education, 1996.

KASPAR, P.; SOBOLA, D.; DALLAEV, R.; RAMAZANOV, S.; NEBOJSA, A.; REZAEE, S.; GRMELA, L. Characterization of Fe2O3 thin film on highly oriented pyrolytic graphite by AFM, Ellipsometry and XPS. **Applied Surface Science**, v. 493, p. 673-678, 1 Nov. 2019.

KLEIN, I.; SHARON, J.; YANIV, A. A mechanism of oxidation of ferrous alloys by super-heat steam. **Scripta Metallurgica**, v. 15, p. 141-144, 1981.

KLEIN, I.; YANIV, A.; SHARON, J. The Oxidation Mechanism of Fe-Ni-Co Alloys. **Oxidation of Metals**, v. 16, p. 1-2, 1981.

KLEIN, I.; YANIV, A.; SHARON, J. The Mechanism of Oxidation of Fe-Ni-Co Alloys: The Role of Ti and Mo. **Applications of Surface Science**, v. 14, i. 3-4, p. 351-358, 1983.

KUMAR, P. R.; JUNG, Y. H.; BHARATHI, K. K.; LIM, C. H.; KIM, D. K. High capacity and low cost spinel Fe_3O_4 for the Na-ion battery negative electrode materials. **Electrochimica Acta**, v. 146, p. 503-510, 10 Nov. 2014.

KUMAR, P.; SHETTY, A. N. Corrosion Behaviour of 18%Ni M250 Grade Maraging Steel under Welded Condition in Hydrochloric Acid Medium. Portugaliae Electrochimica Acta, v. 31, i. 1, p. 21-32, 2013.

LI, Y.; WANG, Y.; LU, H.; LI, X. Preparation of $CoFe_2O_4$eP4VP@Ag NPs as effective and recyclable catalysts for the degradation of organic pollutants with NaBH4 in water. **International Journal of Hydrogen Energy**, v. 45, i. 32, p. 16080-16093, 11 Jun. 2020.

LIMA FILHO, V.; BARROSA, I.; GOMES DE ABREU, H. Influence of Solution Annealing on Microstructure and Mechanical Properties of Maraging 300 Steel. **Materials Research**, v. 20, i. 1, p. 10-14, 2017.

LIN, T. C.; SESHADRI, G.; KELBER, J. A. A consistent method for quantitative XPS peak analysis of thin oxide films on clean polycrystalline iron surfaces. **Applied Surface Science**, v. 119, i. 1-2, p. 83-92, p. 1997.

LIU, W.; CHENG, B.; MIAO, T.; XIE, J.; LIU, L.; SI, J.; ZHOU, G.; QIN, H.; HU, J. Room temperature electric field control of magnetic properties for the α-Fe_2O_3/Fe_3O_4 composite structure. **Journal of Magnetism and Magnetic Materials**, v. 491, p. 165500, Dec. 2019.

LU, L.; AI, Z.; LI, J.; ZHENG, Z.; LI, Q.; ZHANG, L. Synthesis and characterization of Fe–Fe_2O_3 core–shell nanowires and nanoneckaces. **Crystal Growth & Design**, v. 7, i. 2, p. 459-464, 6 Jan. 2007.

LUO, D. W.; SHEN, Z. S. Oxidation behavior of Kovar alloy in controlled atmosphere. **Acta Metallurgica Sinica**, v. 21, i. 6, p. 409-418, 2008.

MADHUSUDHAN REDDY, G.; SRINIVASA RAO, K. Microstructure and corrosion behavior of gas tungsten arc welds of maraging steel. **Defense Technology**, 11, i. 1, p. 48-55, 2015.

MAGNÉE, A.; DRAPIER, J. M.; COUTSOURADIS, D.; HABRAKEN, L.; DUMONT J. **Cobalt monograph series**: Cobalt-containing high-strength steels. Brussels, Belgium: Centre d'Information du Cobalt, 1974. Available at: https://inis.iaea.org/search/search.aspx?orig_q=RN:6217555. Access on: 18 March 2020.

MASOUMI, M.; ABREU, H.F.G.; HERCULANO, L.F.G.; PARDAL, J.M.; TAVARES, S.S.M.; SILVA, M.J.G. EBSD study of early fractured phenomena in a 350 grade Maraging steel elbows exposed to hydrofluoric acid. **Engineering Failure Analysis**, v. 104, p. 379-387, 2019.

MAXIMO, H. W. P. **Avaliação de propriedades mecânicas e microestruturais de juntas de aço maraging soldadas por meio de processos laser e feixe de elétrons**. 201. Master thesis (Mestrado em Ciências da Área de Tecnologia Nuclear) – Instituto de Pesquisas Energéticas e Nucleares, Universidade de São Paulo, São Paulo, 2014. Available at: https://teses.usp.br/teses/disponiveis/85/85134/tde-27052015-090049/publico/2014MaximoAvaliacao.pdf. Access on: 22 March 2020.

MAZZA, T.; BARBORINI, E.; PISERI, P.; MILANI, P.; CATTANEO, D.; LI BASSI, A.; BOTTANI, C.E.; DUCATI, C. Raman spectroscopy characterization of TiO_2 rutile nanocrystals. **Physical Review B**, v. 75, p. 045416, 11 Jan. 2007.

MIRONOVA-ULMANE, N.; KUZMIN, A.; STEINS, I.; GRABIS, J.; SILDOS, I.; PÄRS, M. Raman scattering in nanosized nickel oxide NiO. *In*: JOURNAL OF PHYSICS CONFERENCE SERIES '93, Riga, Latvia, 2007. **Proceedings** […]. Letônia: Journal of Physics, 2007.

MOSHKA, O.; PINKAS, M.; BROSH, E.; EZERSKY, V.; MESHI, L. Addressing the issue of precipitates in maraging steels – Unambiguous answer. **Materials Science and Engineering**: A, v. 638, p. 232-239, 25 Jun. 2015.

NICKEL DEVELOPMENT INSTITUTE. **18 per cent nickel maraging steels**: Engineering properties. Nickel development institute, 1976. Available at: https://www.nickelinstitute.org/media/1598/18_nickelmaragingsteel_engineeringproperties_4419_.pdf. Access on: 22 March 2020.

NWAOGU, U. C.; TIEDJE, N. S.; HANSEN, H. N. A non-contact 3D method to characterize the surface roughness of castings. Journal of Materials Processing Technology, v. 213, i. 1, p. 59-68, 2013.

PARDAL, J. M.; TAVARES, S. S. M.; CINDRA FONSECA, M. P.; ABREU, H. F. G.; SILVA, J. J. M. Study of the austenite quantification by X-ray diffraction in the 18Ni-Co-Mo-Ti maraging 300 steel. **Journal of Materials Science**, v. 41, p. 2301-2307, 2006.

PARDAVI-HORVATH, M. Microwave applications of soft ferrites. **Journal of Magnetism and Magnetic Materials**, v. 215-216, 171-183, 2 Jun. 2000.

PARKINSON, G. Iron oxide surfaces**. Surface Science Reports**, v. 71, i. 1, p. 272-365, 2016.

PAWEL, S. J. Corrosion of High-Alloy Materials in Aqueous Hydrofluoric Acid Environments. **Corrosion**, v. 50, i. 12, p. 963-971, 1994.

PETTY, E. R. Martensite, Fundamentals and Technology: Edited by ER Petty. **Journal of Applied Crystallography**, v. 4, p. 402-403, 1970.

POORMINA, T.; NAYAK, J.; SHETTY, A. N. Corrosion of Aged and Annealed 18 Ni 250 Grade Maraging Steel in Phosphoric Acid Medium. **International Journal of Electrochemical Science**, v. 5, p. 56-71, 2010.

POORMINA, T.; NAYAK, J.; SHETTY, A. N. Effect of 4-(N,N-diethylamino) benzaldehyde thiosemicarbazone on the corrosion of aged 18 Ni 250 grade maraging steel in phosphoric acid solution. **Corrosion Science**, v. 53, i. 11, p. 3688-3696, Nov. 2011.

RACK, H.; KALISH, D. The strength and fracture toughness of 18 Ni (350) maraging steel. **Metallurgical and Materials Transactions B**, v. 2, p. 3011-3020, 1971.

RAJAGOPAL, S.; NATARAJ, D.; KHYZHUM, O. Y.; DJAOUED, Y.; ROBICHAUD, J.; SENTHIL, K.; MANGALARAJ, D. Systematic synthesis and analysis of change in morphology, electronic structure and photoluminescence properties of pyrazine intercalated MoO_3 hybrid nanostructures. **CrystEngComm**, v. 13, i. 7, p. 2358-2368, 2011.

RAMAR, V.; BALASUBRAMANIAN, K. Optical and highly enhanced solar light-driven photocatalytic activity of reduced graphene oxide wrapped α-MoO_3 nanoplates. **Solar Energy**, v. 194, p. 1-10, Dec. 2019.

REED, B. W.; WILLIAMS, D. R.; MOSER, B. P.; KOSKI, K. J. Chemically tuning quantized acoustic phonons in 2D layered MoO_3 nanoribbons. **Nano Letters**, v. 19, p. 4406–4412, 2019.

REZEK, J.; KLEIN, I.; YAHALOM, J. Structure and corrosion resistance of oxides grown on maraging steel in steam at elevated temperatures. **Applied Surface Science**, v. 108, i. 1, p. 159-165, 1997.

ROBINSON, M. R.; ABDELMOULA, M.; MALLET, M.; COUSTEL, R. Starch functionalized magnetite nanoparticles: New insight into the structural and magnetic properties. **Journal of Solid State Chemistry**, v. 277, p. 587-593, Sept. 2019.

RODRIGUES, A. C; BERNARDI, H. H; OTUBO, J. Microstructural Analysis of Co-Free Maraging Steel Aged. **Journal of Aerospace Technology and Management**, v. 6, n. 4, p. 389-394, 2014.

RODRIGUES, A. P. G.; GOMES, D. K. S.; ARAÚJO, J. H.; MELO, D. M. A.; OLIVEIRA, N. A. S.; BRAGA, R. M. Nanoferrites of nickel doped with cobalt: Influence of Co^{2+} on the structural and magnetic properties. **Journal of Magnetism and Magnetic Materials**, v. 374, p. 748-754, 2015.

ROUTRAY, K. L.; SAHA, S.; BEHERA, D. Nanosized $CoFe_2O_4$-graphene nanoplatelets with massive dielectric enhancement for high frequency device application. **Materials Science & Engineering B**, v. 257, p. 114548, Jul. 2020.

SANATKUMAR, B. S.; NAYAK, J.; SHETTY, A. N. Corrosion behavior of 18% Ni M250 grade maraging steel under weld-aged condition in sulfuric acid medium. Chemical Engineering Communications, v. 199, i. 12, p. 1610-1625, 2012.

SANCHIS, R.; ALONSO-DOMÍNGUEZ, D.; DEJOZ, A.; PICOM, M. P.; ÁLVAREZ-SERRANO, I.; GARCÍA, T.; LÓPEZ, M. L.; SOLSONA, B. Eco-friendly cavity-containing iron oxides prepared by mild routes as very efficient catalysts for the total oxidation of VOCs. **Materials**, v. 11, i. 8, p. 1387, 2018.

SANTOS, L. P. M.; BÊRES, M.; BASTOS, I. N.; TAVARES, S. S. M.; ABREU, H. F. G.; SILVA, M. J. G. Hydrogen embrittlement of ultra-high strength 300 grade maraging steel. Corrosion Science, v. 101, p. 12-18, 2015.

SANTOS, L. P. M.; BERES, M.; DE CASTRO, M. O.; SARVEZUK, P. W. C.; WU, L.; HERCULANO, L. F. G.; PAESANO JR, A.; SILVA, C. C.; MASOUMI, M.; DE ABREU, H. F. G. Kinetics of Reverted Austenite in 18 wt.% Ni Grade 300 Maraging Steel: An In-Situ Synchrotron X-Ray Diffraction and Texture Study. **JOM**, v. 72, p. 3502-3512, 2020.

SCHMIDT, M.; ROHRBACH, K. Heat treating in maraging steels. Metals Handbook. **ASM**, v. 4, p. 219-228, 1991.

SHA, W.; CEREZO, A.; SMITH, G. D. W. Phase chemistry and precipitation reactions in maraging steels: Part 4. Discussion and conclusion. **Metallurgical Transactions A**, v. 24, p. 1251-1256, 1993.

SHARMA, P. K.; RAGHUBANSHI, A. S.; SHAH, K. Examining dye degradation and antibacterial properties of organically induced α-MoO_3 nanoparticles, their uptake and phytotoxicity in rice seedlings. **Environmental Nanotechnology, Monitoring & Management**, v. 14, p. 100315, Dec. 2020.

SILVA, C. C.; FARIAS, J. P.; MIRANDA, H. C.; GUIMARÃES, R. F.; MENEZES, J. W. A.; NETO, A. M. Microstructural characterization of the HAZ in AISI 444 ferritic stainless steel welds. **Materials Characterization**, v. 59, i. 5, p. 528-533, May 2008.

SILVA M. J. G.; CARDOSO, J. L.; CARVALHO. D. S.; SANTOS, L. P. M.; HERCULANO, L. F. G.; ABREU, H. F. G.; PARDAL, J. M. The effect of prior austenite grain size on hydrogen embrittlement of Co-containing 18Ni 300 maraging steel. **International Journal of Hydrogen Energy**, v. 44, i. 33, p. 18606-18615, 2019.

SRINIVASAN, P.; RAVAPPAN, J. B. B. Growth of α-MoO_3 Golf Ball Architectures with Interlocking Loops for Selective Probing of Trimethylamine at Room Temperature. **Materials Research Bulletin**, v. 130, p. 110944, Oct. 2020.

STEHLE, R. C.; BOBEK, M. M.; HOOPER, R.; HAHN, D. W. Oxidation reaction kinetics for the steam-iron process in support of hydrogen production. **International Journal of Hydrogen Energy**, v. 36, i. 23, p. 15125-15135, 2011.

SUBBARAMAN, R.; DESHMUKH, S. A.; SANKARANARAYANAN, S. K. Atomistic insights into early stage oxidation and nanoscale oxide growth on Fe (100), Fe (111) and Fe (110) surfaces. **The Journal of Physical Chemistry C**, v. 117, p. 5195-5207, 2013.

SURMAN, P. L. The oxidation of iron at controlled oxygen partial pressures: I. Hydrogen/water vapour. **Corrosion Science**, v. 13, i. 2, p. 113-124, 1973.

TSUKIMURA, K.; SASAKI, S.; KIMIZUKA, N. Cation Distributions in Nickel Ferrites. **Japanese Journal of Applied Physics**, v. 36, p. 3609, 1997.

VASUDEVAN, V.; KIM, S.; WAYMAN, C. Precipitation reactions and strengthening behavior in 18 Wt Pct nickel maraging steels. **Metallurgical Transactions A**, v. 21, p. 2655-2668, 1990.

VIANA, N. F.; DOS SANTOS, N. C.; DE ABREU, H. F. G. The variant selection in the transformation from austenite to martensite in samples of maraging-350 steel. **Journal of Materials Research and Technology**, v. 2, i. 4, p. 298-302, Oct./Dec. 2013.

VISWANATHAN, U. K.; DEY, G. K.; ASUDI, M. K. Precipitation Hardening in 350 grade maraging steel. **Metallurgical Transactions A**, v. 24A, p. 2429-2442, 1993.

VISWANATHAN, U. K.; DEY, G. K.; SETHUMADHAVAN, V. Effects of austenite reversion during overageing on the mechanical properties of 18 Ni (350) maraging steel. **Materials Science and Engineering A**, v. 398, p. 367-372, 2005.

VITOR, P.; TOPOLSKI, D.; LIMA, A.; BRAGANÇA, S.; BERGMANN, C. Preparação e caracterização de espinélio $MgAl_2O_4$ nanoestruturado através de síntese por combustão em solução. **Cerâmica**, v. 62, i. 363, p. 230-236, 2006.

WANG, W.; DING, Z.; ZHAO, X.; WU, S.; LI, F.; YUE, M.; LIU, J. P. Microstructure and magnetic properties of MFe_2O_4 (M = Co, Ni, and Mn) ferrite nanocrystals prepared using colloid mill and hydrothermal method. **Journal of Applied Physics**, v. 117, i. 17A, p. 328, 2015.

WANG, Y.; ZHANG, A.; ZHANG, D.; YANG, J.; LI, H.; MENG, F.; SUN, Z.; CHEN, G. Ultra-low loading of Ag_2CrO_4 on $BiOI/CoFe_2O_4$ microsphere with p-n heterojunction: Highly improved photocatalytic performance for Hg0 removal and mechanism insight. **Journal of Photochemistry and Photobiology A**: Chemistry, v. 396, p. 112543, 1 Jun. 2020.

YAN, W.; BIAN, W.; JIN, C.; TIAN, J. H.; YANG, R. An Efficient Bi-functional electrocatalyst based on strongly coupled CoFe2O4/Carbon nanotubes hybrid for Oxygen reduction and Oxygen evolution. **Electrochimica Acta**, v. 177, p. 65-72, 20 Sept. 2015.

YAN, W.; CAO, X.; TIAN, J.; JIN, C.; KE, K.; YANG, R. Nitrogen/sulfur dual-doped 3D reduced graphene oxide networks-supported CoFe2O4 with enhanced electrocatalytic activities for oxygen reduction and evolution reactions. **Carbon**, v. 99, p. 195-202, Apr. 2016.

YANG, J.; XIAO, X.; CHEN, P.; ZHU, K.; CHENG, K.; YE, K.; WANG, G.; CAO, D.; YAN, J. Creating oxygen-vacancies in MoO_3-x nanobelts toward high volumetric

energy-density asymmetric supercapacitors with long lifespan. **Nano Energy**, v. 58, p. 455-465, 2019.

YANG, Z.; LI, Y.; XHANG, X.; CUI, X.; HE, S.; LIANG, H.; DING, A. Sludge activated carbon-based $CoFe_2O_4$-SAC nanocomposites used as heterogeneous catalysts for degrading antibiotic norfloxacin through activating peroxymonosulfate. **Chemical Engineering Journal**, v. 384, p. 123319, 15 Mar. 2020.

YU, L.; JIANG, Y.; HE, Y.; LIU, C. T. The corrosion behavior of sintering micro-porous Ni–Cu alloy in hydrofluoric acid solution. **Journal of Alloys and Compounds**, v. 638, p. 7-13, 25 Jul. 2015.

YI, Y.; WU, Q.; WANG, W.; CUI, C. In situ depositing an ultrathin CoOxHy layer on hematite in alkaline media for photoelectrochemical water oxidation. **Applied Catalysis B**: Environmental, v. 263, p. 118334, Apr. 2020.

ZHAO, N.; FAN, H.; ZHANG, M.; MA, J.; DU, Z.; YAN, B.; LI, H.; JIANG, X. Simple electrodeposition of MoO_3 film on carbon cloth for high-performance aqueous symmetric supercapacitors. **Chemical Engineering Journal**, v. 390, p. 124477, 15 Jun. 2020.

ZHAO, Y.; NIE, G.; MA, X.; XU, P.; ZHAO, X. Peroxymonosulfate catalyzed by rGO assisted $CoFe_2O_4$ catalyst for removing Hg0 from flue gas in heterogeneous system. **Environmental Pollution**, v. 249, p. 868-877, Jun. 2019.

ZHANG, Y.; CUI, K.; GAO, Q.; HUSSAIN, S.; LV, Y. Investigation of morphology and texture properties of WSi_2 coatings on W substrate based on contact-mode AFM and EBSD. **Surface & Coatings Technology**, v. 396, p. 125966, 2020.

ZHANG, C.; LI, Y.; HOU, Y.; TANG, N.; OHMURA, K.; KOIZUMI, Y.; CHIBA, A. Corrosion resistance of Cu- and Fe-modified Ni–30Co–16Cr–15Mo alloy in aqueous hydrofluoric acid. **Corrosion Science**, v. 89, p. 81-92, Dec. 2014.

ZHANG, T.; LI, Z.; WANG, L.; ZHANG, Z.; WANG, S. Spinel $CoFe_2O_4$ supported by three dimensional graphene as high-performance bi-functional electrocatalysts for oxygen reduction and evolution reaction. **International Journal of Hydrogen Energy**, v. 44, i. 3, p. 1610-1619, 2019.

ZHANG, X.; YANG, S.; YANG, Z.; XU, X. Kinetics and intermediate phases in epitaxial growth of Fe_3O_4 films from deposition and thermal reduction. **Journal of Applied Physics**, v. 120, i. 8, p. 085313, 30 Aug. 2016.

ZHOU, X.; LIU, D.; BU, H.; DENG, L.; LIU, H.; YUAN, P.; DU, P.; SONG, H. XRD-based quantitative analysis of clay minerals using reference intensity ratios, mineral intensity factors, Rietveld, and full pattern summation methods: A critical review. **Solid Earth Sciences**, v. 3, i. 1, p. 16-29, 2018.